

**SEARCH FOR COMPACT OBJECT
COALESCENCES AND UNDERSTANDING
THEIR SIGNIFICANCE USING DATA FROM
ADVANCED LIGO**

by

Debnandini Mukherjee

A DISSERTATION SUBMITTED IN
PARTIAL FULFILLMENT OF THE
REQUIREMENTS FOR THE DEGREE OF

DOCTOR OF PHILOSOPHY
IN PHYSICS

at

The University of Wisconsin–Milwaukee
May 2018

ABSTRACT

SEARCH FOR COMPACT OBJECT COALESCENCES AND UNDERSTANDING THEIR SIGNIFICANCE USING DATA FROM ADVANCED LIGO

by

Debnandini Mukherjee

The University of Wisconsin–Milwaukee, 2018
Under the Supervision of Professor Patrick Brady

Gravitational waves were observed for the first time on September 14, 2015. A 36 and a 29 M_{\odot} black holes were seen to inspiral around each other and merge about ~ 410 Mpc away. This gave momentum to the areas of gravitational wave astrophysics and astronomy. While the universe could be perceived in the electromagnetic spectrum so far, enabling us to “see” it with telescopes, it could now be “listened to” using gravitational waves. Also, black holes being optically dark, could be observed directly for the very first time after this discovery. The 100 year old theory of General Relativity saw direct evidence through this discovery for the first time. Ever since the first observation, 5 black hole binaries and a binary neutron star have been seen to merge, through gravitational waves. In case of the binary neutron star merger, its electromagnetic counter part, a gamma ray burst was also observed by astronomers, thereby corroborating it.

Hence, I have been writing my dissertation in an era of pioneering discoveries. I will try to summarize my contributions to the field at this stage. The major aspects of my work that my dissertation explores, are as follows:

- 1) contributions to the search for Intermediate mass binary black holes (total masses $100 - 10^5 M_{\odot}$) for the first observing run of LIGO that extended between September 12, 2015 and January 14th 2016;
- 2) preparations for the second observing run of LIGO including helping integrate the search for stellar mass and the intermediate mass binary black holes, so as to have an optimally sensitive combined search;
- 3) analysis and interpretation of science data during the second observing run which lasted

between 30th November 2016 and 26th August 2017. This included work on improving and optimizing the search sensitivity;

4) continued effort on the calculation of astrophysical rates of different populations of compact objects and with the preparation for the next observing run.

TABLE OF CONTENTS

1 From General Relativity to Gravitational Waves and Their Detections using Advanced LIGO	1
1.1 Introduction: Newtonian gravity to General Relativity:	1
1.2 Theory of General Relativity and Gravitational Waves	3
1.2.1 Linearized gravity	4
1.2.2 Gravitational waves	4
1.2.3 Production of gravitational waves	6
1.2.4 Energy and angular momentum in gravitational waves	7
1.2.5 Orbiting binary system	8
1.3 LIGO detectors	10
1.4 Organization of this dissertation	13
2 Towards a combined stellar mass and intermediate mass search and its effect on the spacetime volume sensitivity of the search	14
2.1 Introduction	14
2.2 Background	15
2.2.1 Combined search	16
2.2.2 Comparison of ranking between the searches	17
2.3 Study of the sensitivity of different template banks to various simulations	18
2.3.1 Using Monte Carlo Integration	19
2.3.2 Using the efficiency parameter method used by the pipeline	22
2.4 Investigations and conclusions Using IMBH run with IMBH injection set	23
2.4.1 Using the original full injection set and the pruned set	23
2.4.2 Diagnostic plots to understand difference between pruned and full IMBH injection sets	24
2.4.3 Regenerating the pipeline plot using the full injection set	25
2.4.4 Comparison of all three methods for IMBH run using IMBH injections	25
2.4.5 Folding in a trials factor for IMBH run with IMBH injection results	25

2.4.6	Comparison between IMBH and combined search sensitivities for IMBH injections	26
2.4.7	Comparison of pipeline and efficiency methods for IMBH run using IMBH pruned injections and the mystery of earlier disagreement	28
2.5	Looking Forward	29
3	Does a Supernova Mass Gap Really Exist? using source-dependent template-weighting and FGMC formalism to investigate the SN mass gap	44
3.1	Background	44
3.1.1	Astrophysical motivation for inspecting the mass gap	44
3.2	Methods and techniques used	46
3.2.1	Two component Rates computation for CBC	47
3.2.2	Multi component Rates computation using FGMC formalism	47
3.3	Steps undertaken to obtain a posterior for mass gap populations	48
3.3.1	Injections and data used	49
3.3.2	Distribution of recovery of injections across groups of template banks	50
3.3.3	Obtaining count posteriors for 5 categories of populations and comparison with the earlier 4 categories	50
3.4	Effect of adding an event at the center of the gap	51
3.5	Number of events needed for a detection in the mass gaps for different mass distributions	51
3.6	Effect of events at the edge of the gap	52
3.7	Results, conclusions and looking forward	52
4	Contributions to the template bank used by the offline Gstlal pipeline for the 2nd observing run	59
4.1	Introduction	59
4.2	Background	60
4.3	Design and construction of the O2 bank	61
4.3.1	Astrophysical sources targeted:	61

4.3.2	Construction of the O2 bank	62
4.3.3	SVD binning and bank splitting	68
4.4	Investigations of changes in template placement and binning styles	69
4.4.1	\mathcal{M} - χ binning Vs template duration based binning	70
4.4.2	\mathcal{M} - χ binning vs duration based binning with unequal number of templates (hierarchical) in each bin	71
4.4.3	1000 template grid addition Vs 5000 template grid addition to the bank	71
4.4.4	Uniform duration based binning Vs duration based binning with unequal number of templates (hierarchical) in each bin	71
4.4.5	No grid Vs addition of 1000 template grid to the bank in case of \mathcal{M} - χ binning	72
4.4.6	No grid Vs addition of 1000 template grid to the bank in case of duration based binning	72
4.5	Effectiveness of the O2 bank	72
4.6	Results and conclusions	75
5	Contributions to the IMBH search and its improvement	90
5.1	The IMBH search region and astrophysical populations targeted in O1	90
5.2	The search in 1st observing run vs 2nd observing run	92
5.2.1	Comparison of the search sensitivity in 1st and 2nd observing runs of advanced LIGO	93
5.3	Inclusion of higher order modes of waveforms	95
5.3.1	Importance of higher order modes in the search	97
5.3.2	The contribution of higher order modes to the search sensitivity	98
5.4	looking forward: Plans for 3rd observing run	100
6	Contributions to the Analysis of Advanced LIGO data using Matched Filter Based Offline Runs	103
6.1	Introduction	103
6.2	Contributions to latest and 2nd observation run (O2)	103

6.2.1	Contributions to GstLAL-based inspiral pipeline search	103
6.2.2	Conducting analysis runs and related investigations	104
6.2.3	Contribution to BNS rates calculation	107
6.3	Contributions to papers	109
6.4	Contribution to 1st Observation run (O1):	111
6.4.1	SNR based trimming of IMBH injection files:	111
6.4.2	Investigations of missed injections:	111
7	Conclusion	112
	Curriculum Vitae	122

LIST OF FIGURES

1	Gravitational-wave polarizations	6
2	[1] A binary system orbiting on the $x^1 - x^2$ plane.	8
3	[3] A simplified diagram of the Advanced LIGO detector. <i>Inset.</i> (a) Location and orientation of the detector at Hanford, WA (H1) and Livingston, LA (L1). (b) The instrument noise for each detector.	11
4	A visual representation of the different searches in the log of the component mass space.	15
5	Visual representation of a combined bank made by adding IMBBH and the stellar mass bank, in the component mass space.	16
6	A visual representation of the binary populations for which simulated waveforms were used, in the component mass space, in solar masses.	18
7	Volume sensitivity vs CFAR for stellar mass search with all injections	19
8	Volume sensitivity vs CFAR for IMBH search with all injections	20
9	Volume sensitivity plot using a pruned IMBH injection set with an IMBH bank using Monte Carlo Integration	30
10	Volume sensitivity plot using a full IMBH injection set with an IMBH bank using Monte Carlo Integration	31
11	Volume sensitivity plot using a pruned IMBH injections set with an IMBH bank (from GstLAL-based inspiral pipeline).	32
12	Volume sensitivity vs CFAR for IMBH search with IMBH injections using efficiency method	33
13	Efficiency vs distance for IMBH search with IMBH injections, comparing between pruned and full sets	34
14	ϵ vs injection distance using pruned set as found (green) using number of found injections as numerator (red).	35
15	gstlal pipeline plot regenerated using full IMBH injection set.	36

16	Volume sensitivity vs CFAR for IMBH run using full IMBH injections (using Monte Carlo Integration)	37
17	Volume sensitivity vs CFAR for IMBH run using full IMBH injections (using independent code)	37
18	Overlay of Volume Vs CFAR plot made using all three methods, using full IMBH injection set, for IMBH run	38
19	Shift in the Volume vs CFAR plot using full IMBH injection set, for IMBH analysis, on multiplying CFARs by a trials factor of 2, accounting for the two independent searches, in order to compare with combined search. . .	39
20	Overlay of volume sensitivity vs CFAR for IMBH run and combined search using full IMBH injections, without a trials factor.	40
21	Overlay of volume sensitivity vs CFAR for IMBH search and combined search using full IMBH injections, with a trials factor.	40
22	Relative volume sensitivity vs CFAR for IMBH search and the combined search using full IMBH injections, without a trials factor.	41
23	Relative volume sensitivity vs CFAR for IMBH search and combined search using full IMBH injections, with a trials factor.	41
24	Relative volume sensitivity vs CFAR for IMBH search and combined search using full IMBH injections, with and without a trials factor for comparison.	42
25	Volume sensitivity vs CFAR for IMBH run using IMBH pruned injections (gstlal pipeline)	43
26	Volume sensitivity vs CFAR for IMBH run using IMBH pruned injections (efficiency method, using appropriate segments and live time.	43
27	Predicted galactic neutron star/black hole mass distribution. From Rapid ($<\sim 100 - 200\text{ ms}$) and Delayed ($>\sim 500 - 1000\text{ ms}$) models of supernova explosion and from Star Track population synthesis code.	46
28	90 % credible intervals for recovered m_2 as a function of the true mass. .	47
29	Representation of the categories of different populations of compact binaries in their component mass space.	49
30	Activation counts vs SVD bin no. plots	54

31	Count posteriors for 4 component FGMC	55
32	Count posteriors for 5 component FGMC	56
33	Effect of adding a high and a low significance event.	57
34	Dependence of number of events needed for detection in the gap, on mass distribution	57
35	Effect of events at the edge of the gap	58
36	A visual representation of the power spectral density used to model detec- tor noise.	62
37	A visual representation of the original O2 search bank in the component mass space	64
38	The extra 14667 templates that were added to the original O2 bank, with a higher minimum match above a total mass of $80 M_{\odot}$ in the component mass space.	65
39	The uniform grid bank with a 1000 templates spanning $100\text{-}400 M_{\odot}$ in total mass	66
40	A visual representation of the template bank used by the gstlal offline search in the second observing run in the component mass space.	67
41	A visual representation of the template bank used in the low-latency mode of the GstLAL-based inspiral pipeline, in the second observing run in the component mass space.	67
42	The initial $\mathcal{M} - \chi_{\text{eff}}$ split banks where each color denotes a different svd bank	69
43	A visual representation of the improved $\mathcal{M} - \chi_{\text{eff}}$ split banks where each color denotes a different svd bank.	70
44	$\mathcal{M}\text{-}\chi$ vs duration binning	77
45	$\mathcal{M}\text{-}\chi$ vs hierarchical duration binning	78
46	1000 vs 5000 grid addition	79
47	Uniform vs hierarchical duration binning	80
48	No grid vs 1000 grid for $\mathcal{M}\text{-}\chi$	81
49	No grid Vs 1000 grid for $\mathcal{M}\text{-}\chi$	82

50	Fitting factor plots for BNS SpinTaylorT4 type waveforms	83
51	Fitting factor plots for BNS TaylorF2 type waveforms	84
52	Fitting factor plots for NSBH SEOBNRv4_ROM waveforms	85
53	Fitting factor plots for NSBH IMRPhenomPv2 waveforms	86
54	Fitting factor plots for BBH SEOBNRv4_ROM waveforms	87
55	Fitting factor plots for IMBH SEOBNRv4_ROM waveforms	88
56	Fitting factor plots for IMBH EOBNRv2HML_ROM waveforms	89
57	A visual representation of the original IMBH only dedicated search bank used in the first observing run of Advanced LIGO (O1), in the component mass space.	91
58	A visual representation of the template bank used in the 2nd observing run of Advanced LIGO and Virgo (O2), in the component mass space. The search region corresponding to the O1 IMBH search region is shown.	92
59	Simulated signals or injections used to compare between the sensitivity of the GstLAL- inspiral based search in O1 Vs in O2.	94
60	Space time volume sensitivity Vs combined false alarm rate (CFAR) plots	95
61	Space time volume sensitivity ratio Vs combined false alarm rate (CFAR) plots	96
62	Spacetime volume sensitivity ratio vs combined false alarm rate (CFAR) plots	101
63	Spacetime volume sensitivity ratio vs combined false alarm rate (CFAR) plots	102
64	Template banks before and after change	105
65	Change in event count Vs IFAR plots	105
66	Missed injection plots for chunk 8	106
67	VT sensitivity vs CFAR plots for chunk 8	106
68	Example of an omega scan followup of a missed injection, showing multiple glitches in H1 instrument, causing the injection to be missed.	107
69	Change in event count Vs IFAR plots in openbox	108

70	Omega scan followup of the loudest coincident trigger in chunk 8, which turned out to be a glitch in L1 detector.	108
71	The BNS posterior obtained in Eq. 6.2.6.	110

LIST OF TABLES

1	Mass range and number of templates of the stellar and IMBBH search bank used for O1 and the combination of these.	15
2	Differences between the three searches. SVD grouping of templates is explained in chapter 4. The parameters for the search using the combined bank, were kept mostly the same as for the IMBH only search.	16
3	The False Alarm Rate (FAR), False Alarm Probability (FAP), log likelihood ($\ln \Lambda$), Signal to noise ratio (SNR) and component masses, compared between three searches for GW150914 event.	17
4	The False Alarm Rate (FAR), False Alarm Probability (FAP), log likelihood ($\ln \Lambda$), Signal to noise ratio (SNR) and component masses, compared between three searches for LVT151012 candidate. It is clear that the combined search seems to assign it a lower FAR (hence higher significance) than the stellar mass search and a slightly higher FAR than the IMBH search.	17
5	Comparison of Volume sensitivity obtained from different methods at CFAR of 10^{-7} for the middle mass bin, for IMBH run with IMBH injections. We see that for the full injection set, the results from the three different methods agree. For the pruned set, they agree between the Monte Carlo and the efficiency method, but not with the pipeline results.	24
6	Description of different categories of astrophysical populations in terms of the component masses of the systems. The simulations used to obtain posteriors for each category, satisfy these requirements.	50
7	Description of different categories of astrophysical populations, in terms of their mass and spin parameters, that were used as the simulations, injected to test the sensitivity of the bank towards them.	74

ACKNOWLEDGMENTS

I would like to thank all sources of funding (all awards, scholarships, research assistant and teaching assistant appointments, as indicated in the Curriculum Vitae section at the end). I would like to thank my advisor Dr. Patrick Brady for being an indispensable part of this journey. I would like to thank Dr. Jolien Creighton for having been another indispensable part of this journey and for always being there for discussions.

I would like to thank all my present and past collaborators, primarily, Laleh Sadeghian, Sarah Caudill, Shasvath Kapadia, Duncan Meacher, Chad Hanna, Les Wade, Ryan Lang, Francesco Salemi, Surabhi Sachdev, Heather Fong, Cody Messik, Kipp Cannon, Chris Pankow, Stephen Privitera and others. I would like to thank all other members of CGCA at UWM and other members of the Physics department, for teaching me and helping me over the last six years. I would like to thank my committee for all your help and support in shaping me.

I would like to thank Heidi Matera, Gracie Leibenstein and Kate Valerius for all your help with travel and paperwork. I would like to express my gratitude to Alina Istrate for all her talks and advice and teas, Shaon Ghosh for all your advice, Sarah Vigeland, Sinead Walsh, Shasvath Kapadia and fellow graduate student Kristina Oslo For helping me proof read. Thank you for all your comments. I especially thank Kristina, Alina and Sarah, for being there in difficult times.

I would like to thank other members of the LVC that I have developed friendships with over the years, especially Min-A-Cho and Michael Coughlin. Even though we never directly collaborated, your support and interactions are valued.

Most importantly, I would like to thank my parents and my sister, for all their help and support over the years. I would not be here without you. I would also like to thank all my teachers, from school, college and the two universities I have attended so far. Thank you God for helping me though every step.

Chapter 1

From General Relativity to Gravitational Waves and Their Detections using Advanced LIGO

1.1 Introduction: Newtonian gravity to General Relativity:

Most people first come to know about gravity at some point in school, where one is taught the Newtonian concept of how gravity is the force with which a massive body attracts another and its magnitude is inversely proportional to the square of the distance between them. Then follows the story of how Newton saw the apple fall. This is at best a partial explanation of gravity, because the theory has major limitations. The most important limitation being, it expects the effect to be instantaneous. This is in the face of the Special Theory of Relativity established by Einstein in 1905, which establishes the path taken by light to be the causal connection between two events, or in other words, the speed of light is the speed of causality.

Einstein's intention to understand gravity in the light of Special Theory of Relativity, gave rise to the General Theory of Relativity, published by Einstein in 1915. Gravity was explained by his theory, as the curvature of space-time, which were considered at par, and objects "falling" under gravity is simply following a geodesic or the straightest possible path. So Newton's apple didn't "fall", it just followed the straightest trajectory

in a curved space time. Now thats a more interesting story!

Over almost a hundred years, the world has seen several indirect evidence of General Relativity. The precession of Mercury by 43 arc seconds every century while orbiting the sun, could not be fully explained by any other theory. The observation of the bending of light of stars around the sun, during a solar eclipse in 1918, when the foreground was blocked out, agreed with general relativistic predictions. In the experiment by Pound and Rebka in 1958, a photon emitted by an atom was seen to red shift or lose energy as it moved away from earth, in a way that was consistent with general relativity. When humans got out to space, more effects could be observed. The dragging of spacetime while earth rotates was a general relativistic prediction, tested by Gravity Probe B in the year 2004 and the slower passage of time on the ground as compared to low earth orbits which is routinely used for GPS navigation, have been furthur evidence of general relativity.

But Newtonian gravity has to be recovered at a certain limit, one where $GM/c^2 \ll 1$ and $v/c \ll 1$ where v is the characteristic speed of bodies in the system and M and R are the characteristic mass and size of the system, c being speed of light and G is the gravitational constant. Since a changing tidal field can do work on distant bodies in Newtonian gravity, to conserve energy, the same must be true in general relativity. Hence, to produce a changing tidal field, energy must be radiated out to the rest of the universe by the gravitating system, as the bodies on which work is done, cannot have a reactive force on the gravitating system instantaneously, as that would violate Special Theory of Relativity. This radiation is called gravitational radiation [1]. Hence gravitational waves are the oscillations in space time that carry information about the changes in the gravitating source. This prediction of general relativity was famously used to explain the decay of the orbit of the Hulse and Taylor binary [2] where observation of the light curves matched the general relativistic predictions precisely.

It was however not until 14th September 2015 that gravitational waves could be experimentally detected for the first time [3]. This was made possible by instruments called LIGO, which stands for Laser Interferometer Gravitational Wave Observatory. These detectors use the principle of Michelson's Interferometers. Interfering beams of laser are

maintained at a configuration such that a small relative shift in the phase of the lasers due to a passing gravitational wave would cause light to be detected by photodetector circuits which generate an electrical signal. But more on that later.

1.2 Theory of General Relativity and Gravitational Waves ¹

Conservation of stress-energy implies that field equations need to be constructed so that the spacetime geometry is related to stress energy. In the words of John Wheeler, in general relativity, matter curves space time, while space time informs matter how to move. This relation is ensured by the The Einstein field equations which has the form:

$$G_{\alpha\beta} = \frac{8\pi G}{c^4} T_{\alpha\beta}, \quad (1.2.1)$$

where, $G_{\alpha\beta}$ is the Einstein tensor:

$$G_{\alpha\beta} = R_{\alpha\beta} - \frac{1}{2} g_{\alpha\beta} R, \quad (1.2.2)$$

where the Ricci tensor $R_{\alpha\beta} = g^{\mu\nu} R_{\alpha\mu\beta\nu} = R_{\alpha\mu\beta}{}^{\mu}$, the Ricci scalar $R = g^{\mu\nu} R_{\mu\nu} = R_{\mu}{}^{\mu}$, and $R_{\alpha\beta\gamma\delta}$ is the Riemann curvature tensor.

The metric defines the distance s between two points in spacetime as:

$$ds^2 = g_{\mu\nu} dx^{\mu} dx^{\nu}. \quad (1.2.3)$$

which defines the geometry of the spacetime. For flat spacetime in rectilinear coordinates, the metric is given by:

$$g_{\alpha\beta} = \eta_{\alpha\beta} = \text{diag}(-c^2, 1, 1, 1) = \text{diag}(-1, 1, 1, 1) (\text{assuming, } c = 1) \quad (1.2.4)$$

The matter stress energy tensor $T_{\alpha\beta}$ has the following components:

$$T^{00} = \rho \quad (1.2.5)$$

$$T^{0i} = T^{i0} = J^i \quad (1.2.6)$$

$$T^{ij} = S^{ij}, \quad (1.2.7)$$

¹This section closely follows [1] and has been helped with ideas from [4]

where ρ is the mass density, J^i are the components of the momentum density, and S^{ij} are the components of the stress tensor.

1.2.1 Linearized gravity

The Einstein Field Equations can be written in the weak field approximation, which is called the linearized gravity approximation. In this regime, the spacetime metric is assumed to be flat as shown in Eq. 1.2.4, with a small perturbation $h_{\alpha\beta}$ as:

$$g_{\alpha\beta} = \eta_{\alpha\beta} + h_{\alpha\beta}. \quad (1.2.8)$$

Retaining only terms that are linear in h in Einstein Tensor, the Einstein field equations becomes:

$$-\square \bar{h}_{\alpha\beta} - \eta_{\alpha\beta} \frac{\partial^2 \bar{h}^{\mu\nu}}{\partial x^\mu \partial x^\nu} + \frac{\partial^2 \bar{h}_\beta^\mu}{\partial x^\alpha \partial x^\mu} + \frac{\partial^2 \bar{h}_\alpha^\mu}{\partial x^\mu \partial x^\beta} \approx \frac{16\pi G}{c^4} T_{\alpha\beta}, \quad (1.2.9)$$

where $\square = \eta^{\mu\nu} \partial^2 / (\partial x^\mu \partial x^\nu)$ is the d'Alembertian operator also known as the flat-spacetime wave operator and $\bar{h}_{\alpha\beta} = h_{\alpha\beta} - \frac{1}{2} \eta_{\alpha\beta} h$ is the trace-reversed metric perturbation, where $h = \eta^{\mu\nu} h_{\mu\nu} = h_\mu{}^\mu$.

In order to obtain a simplified version of the wave equation, we select a gauge similar to the Lorenz gauge in electrodynamics, such that the divergence terms of the trace reversed metric perturbation can be discarded. Hence, $(\partial \bar{h}^{\mu\alpha} / \partial x^\mu = 0)$.

Under this gauge choice, the Einstein field equations become:

$$-\square \bar{h}_{\alpha\beta} \approx \frac{16\pi G}{c^4} T_{\alpha\beta}. \quad (1.2.10)$$

1.2.2 Gravitational waves

The linearized Einstein field equations in vacuum, in the Lorenz gauge looks like:

$$\square \bar{h}_{\alpha\beta} \approx 0. \quad (1.2.11)$$

An important solution to Eq. (1.2.11) is the plane wave solution which propagates in the z -direction, since the Lorenz condition $\partial\bar{h}^{\mu\alpha}/\partial x^\mu = 0$ ensures that the plane wave is transverse, that is, it oscillates in a plane perpendicular to its propagation. Using the gauge freedom left within the Lorenz gauge we get the following three conditions for the trace-reversed metric perturbation:

It is traceless ($\delta^{ij}h_{ij} = 0$) and completely spatial ($h_{\alpha 0} = 0$), and this is called the transverse traceless (TT) gauge.

In the TT gauge, $\bar{h}_{\alpha\beta} = h_{\alpha\beta} \equiv h_{\alpha\beta}^{\text{TT}}$ since the perturbation is traceless. Also, propagation along the z -axis would mean, from Eq. (1.2.11) the components of the perturbation are functions of the retarded time $t - z/c$. Hence the waves are also transverse:

$$\delta^{ij}\frac{\partial h_{ij}^{\text{TT}}}{\partial x^k} = 0 .$$

Therefore, in the TT gauge, the solution of the vacuum Einstein field equations for the metric perturbation are transverse plane waves traveling at the speed of light, called gravitational waves.

In the TT gauge, After the removal of all the gauge freedom, the Reimann Tensor in the Einstein Field Equation is left with only two degrees of freedom, or rather, only two independent functions of $(t - z/c)$. For a gravitational wave traveling in the z -direction, the Lorenz condition (now $\partial\bar{h}^{ij}/\partial x^i = 0$ since the perturbation is purely spatial) implies that $\partial\bar{h}^{3i}/\partial x^3 = 0$, hence $\bar{h}_{3i}(t - z/c) = h_{3i}(t - z/c) = h_{3i}^{\text{TT}}(t - z/c) = \text{constant}$. We can take this constant to be zero. The non-zero components then are h_{11}^{TT} , h_{12}^{TT} , h_{21}^{TT} , and h_{22}^{TT} . Since the perturbation is symmetric,

$$h_{12}^{\text{TT}} = h_{21}^{\text{TT}} \equiv h_{\times}(t - z/c), \quad (1.2.12)$$

and since the perturbation is traceless and $h_{33}^{\text{TT}} = 0$,

$$h_{11}^{\text{TT}} = -h_{22}^{\text{TT}} \equiv h_{+}(t - z/c). \quad (1.2.13)$$

We refer to these two polarizations as “plus” and “cross” because of how they affect masses, which can be seen in Fig. 1.

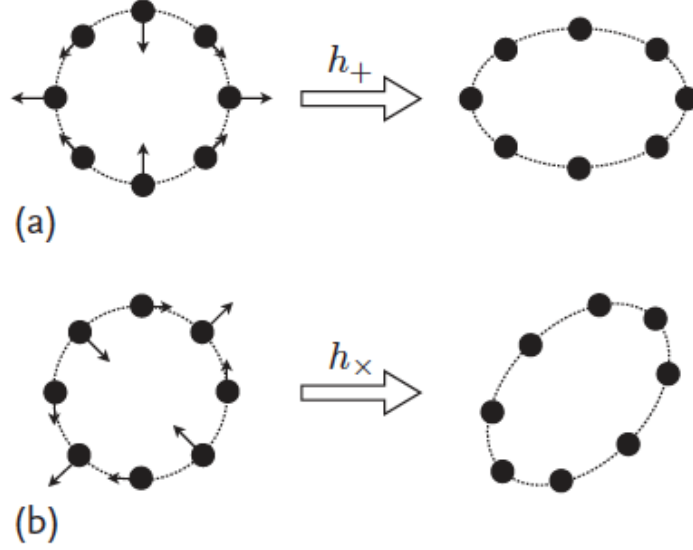


Figure 1 : [1] The figure shows the distortion of a hoop of particles when a gravitation wave passes transverse to its plane.(a) Shows the effect of a purely plus polarized wave (b) Shows the effect of a purely cross polarized wave.

1.2.3 Production of gravitational waves

The linearized Einstein Field Equation 1.2.10 can be written so as to include the higher order contributions from the metric perturbation

$$\square \bar{h}^{\alpha\beta} = -\frac{16\pi G}{c^4} T^{\alpha\beta} + O(h^2), \quad (1.2.14)$$

By representing the stress-energy tensor that includes $O(h^2)$ as $\tau_{\alpha\beta}$ the above can be rewritten as:

$$\square \bar{h}^{\alpha\beta} = -\frac{16\pi G}{c^4} \tau^{\alpha\beta}. \quad (1.2.15)$$

The solution to $\bar{h}^{\alpha\beta}$ for the exact field equations can be found using a Green's function, and the solution is:

$$\bar{h}^{\alpha\beta}(t, \vec{x}) = \frac{4G}{c^4} \int \frac{\tau_{\alpha\beta}(t - |\vec{x} - \vec{x}'|/c, \vec{x}')}{|\vec{x} - \vec{x}'|} d^3 \vec{x}'. \quad (1.2.16)$$

To this integral, we apply the “far zone” approximation, which is where gravitational wave detectors are located relative to astrophysical sources. The assumptions of the far zone are that the size of the source R is much less than the wavelength λ , which is much

less than the distance to the source r . In the far zone and exploiting an identity of the effective stress energy tensor, equation (1.2.16) becomes

$$\bar{h}^{ij}(t, \vec{x}) \approx \frac{2G}{c^4 r} \ddot{I}^{ij}(t - r/c), \quad (1.2.17)$$

where the quadrupole tensor is defined

$$I^{ij}(t) = \int x^i x^j \tau^{00}(t - r/c, \vec{x}) d^3 \vec{x}. \quad (1.2.18)$$

After projecting to the TT gauge using the transverse projection operator, the far-zone solution for the metric perturbation is

$$h_{ij}^{\text{TT}}(t) \approx \frac{2G}{c^4 r} \ddot{I}_{ij}^{\text{TT}}(t - r/c). \quad (1.2.19)$$

where, the transverse-traceless quadrupole tensor is

$$I_{ij}^{\text{TT}}(t) = P_{ik} I^{kl} P_{lj} - \frac{1}{2} P_{ij} P_{kl} I^{kl}, \quad (1.2.20)$$

and the transverse projection operator is

$$P_{ij} = \delta_{ij} - \hat{n}_i \hat{n}_j, \quad (1.2.21)$$

and the unit vector in the direction of propagation is $\hat{n}_i = x_i/r$.

1.2.4 Energy and angular momentum in gravitational waves

It can be shown that the gravitational wave stress-energy tensor can be written as:

$$T_{\alpha\beta}^{\text{GW}} = \frac{c^4}{32\pi G} \left\langle \frac{\partial h_{\text{TT}}^{ij}}{\partial x^\alpha} \frac{\partial h_{ij}^{\text{TT}}}{\partial x^\beta} \right\rangle. \quad (1.2.22)$$

The gravitational wave luminosity can be calculated from this as:

$$L = -\frac{dE}{dt} = \frac{1}{5} \frac{G}{c^5} \left\langle \ddot{\mathcal{I}}_{ij} \ddot{\mathcal{I}}^{ij} \right\rangle, \quad (1.2.23)$$

where

$$\mathcal{I}_{ij} = \int \left(x_i x_j - \frac{1}{3} r^2 \delta_{ij} \right) \tau^{00}(\vec{x}) d^3 \vec{x}. \quad (1.2.24)$$

In the TT gauge, $\mathcal{I}_{ij}^{\text{TT}} = I_{ij}^{\text{TT}}$ since \mathcal{I}_{ij} is traceless.

From this it can be shown, the amount of angular momentum radiated is

$$\frac{dJ_i}{dt} = -\frac{2}{5} \frac{G}{c^5} \epsilon_{ijk} \left\langle \ddot{\mathcal{I}}^{jl} \ddot{\mathcal{I}}_l^k \right\rangle, \quad (1.2.25)$$

where ϵ_{ijk} is the usual cyclic Levi-Civita function.

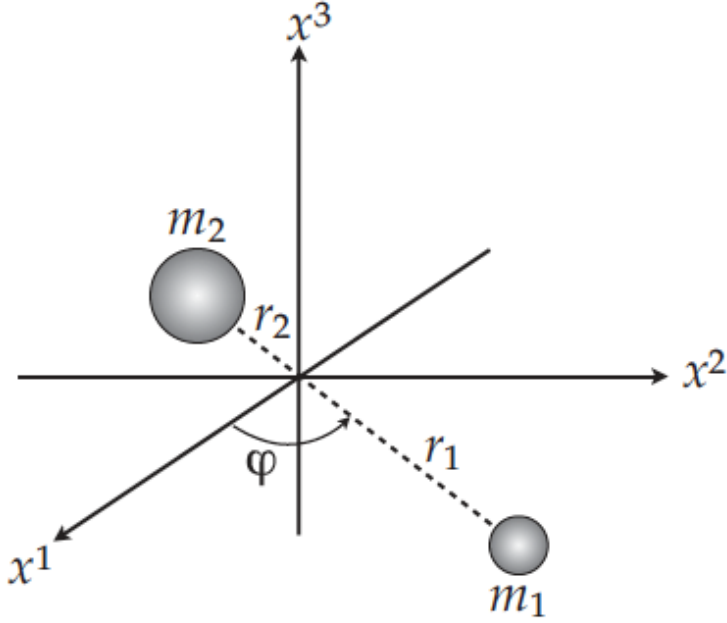


Figure 2 : [1] A binary system orbiting on the $x^1 - x^2$ plane.

1.2.5 Orbiting binary system

We consider a binary system comprising two orbiting point particles with masses m_1 and m_2 . We can use this set up to model a coalescing compact binary system, in a circular orbit on the $x^1 - x^2$ plane so that the orbital angular momentum vector points along x^3 . Let r_1 and r_2 be the separations of these bodies from the origin. Defining orbital separation $a = r_1 + r_2$ and $M = m_1 + m_2$, the reduced mass of the system $\mu = m_1 m_2 / M$, the non vanishing components of the quadrupole tensor I_{ij} are:

$$I_{11} = \mu a^2 \cos^2 \phi$$

$$I_{22} = \mu a^2 \sin^2 \phi$$

$$I_{12} = \mu a^2 \cos \phi \sin \phi$$

Using $v = (\pi M G f_{\text{gw}})^{1/3}$ from Kepler's 3rd Law, f_{gw} is the gravitational wave frequency, and the orbital phase $\phi = \omega t = \pi f_{\text{gw}} t = v^3 t / (GM)$, for an observer on the orbital axis but at an inclination ι from the axis, the second time derivative of the transverse-traceless quadrupole tensor for a CBC system is

$$\ddot{I}_{ij}^{\text{TT}} = -2\mu v^2 \begin{bmatrix} \left(\frac{1+\cos^2\iota}{2}\right) \cos 2\phi & \cos \iota \sin 2\phi & 0 \\ \cos \iota \sin 2\phi & -\left(\frac{1+\cos^2\iota}{2}\right) \cos 2\phi & 0 \\ 0 & 0 & 0 \end{bmatrix},$$

The far-zone solution to the linearized Einstein Field Equations which are already in the TT gauge for an observer at a distance r on the x^3 is:

$$h_{ij}^{\text{TT}}(t) = \frac{2G}{c^4 r} \ddot{I}_{ij}^{\text{TT}}(t - r/c). \quad (1.2.26)$$

which takes the form

$$h_{ij}^{\text{TT}} = -\frac{4G\mu}{c^2 r} \left(\frac{v}{c}\right)^2 \begin{bmatrix} \left(\frac{1+\cos^2\iota}{2}\right) \cos(2\phi(v)) & \cos \iota \sin(2\phi(v)) & 0 \\ \cos \iota \sin(2\phi(v)) & -\left(\frac{1+\cos^2\iota}{2}\right) \cos(2\phi(v)) & 0 \\ 0 & 0 & 0 \end{bmatrix}, \quad (1.2.27)$$

and the functional form for the system's energy and luminosity can be used to solve for $\phi(v)$ and v in term of t .

Newtonian chirp

In the Newtonian case, the energy and luminosity of a CBC system are

$$E(v) = -\frac{1}{2}c^2 M \eta \left(\frac{v}{c}\right)^2 \quad (1.2.28)$$

$$L(v) = \frac{32}{5} \frac{c^5}{G} \eta^2 \left(\frac{v}{c}\right)^{10}, \quad (1.2.29)$$

where $\eta = \mu/M$. Since the luminosity is given by $L = -dE/dt$. Therefore, using this relationship and the chain rule,

$$\frac{dt}{dv} = \frac{dt}{dE} \frac{dE}{dv} = -\frac{E'}{L}, \quad (1.2.30)$$

where the prime indicates a derivative with respect to v . Also, since $\phi = \omega t = v^3 t / (GM)$,

$$\frac{d\phi}{dv} = \frac{d\phi}{dt} \frac{dt}{dv} = -\frac{v^3}{GM} \frac{E'}{L}. \quad (1.2.31)$$

Integrating Eqs. (1.2.30) and (1.2.31) to the point of coalescence v_c , gives

$$t = t_c + \int_v^{v_c} \frac{E'(u)}{L(u)} du, \quad (1.2.32)$$

$$\phi = \phi_c + \int_v^{v_c} \frac{u^3}{GM} \frac{E'(u)}{L(u)} du. \quad (1.2.33)$$

The binary loses energy to gravitational waves as the orbit decays and the orbital velocity continually increases until the bodies eventually coalesce. Using Eqs. (1.2.28) and (1.2.29) in Eqs. (1.2.32) and (1.2.33) and solving for $t(v)$ and $\phi(v)$

$$t(v) = t_c - \frac{5}{256} \frac{GM}{\eta c^3} \left(\frac{v}{c}\right)^{-8}, \quad (1.2.34)$$

$$\phi(v) = \phi_c - \frac{1}{32\eta} \left(\frac{v}{c}\right)^{-5}. \quad (1.2.35)$$

Inverting Eq. (1.2.34) to find $v(t)$, substituting this into Eq. (1.2.35) to find $\phi(t) = \phi(v(t))$, and putting $v(t)$ and $\phi(t)$ into Eq. (1.2.27) gives the gravitational wave perturbation as a function of time. The two polarizations are

$$h_+(t) = -\frac{GM}{c^2 r} \left[\frac{c^3(t_c - t)}{5GM} \right]^{-1/4} \frac{1 + \cos^2 \iota}{2} \cos \left(2\phi_c - 2 \left[\frac{c^3(t_c - t)}{5GM} \right]^{5/8} \right) \quad (1.2.36)$$

$$h_\times(t) = -\frac{GM}{c^2 r} \left[\frac{c^3(t_c - t)}{5GM} \right]^{-1/4} \cos \iota \sin \left(2\phi_c - 2 \left[\frac{c^3(t_c - t)}{5GM} \right]^{5/8} \right), \quad (1.2.37)$$

where $t < t_c$. This is known as a ‘‘chirp’’ waveform because its frequency and amplitude both sweep up with time. The Newtonian chirp only depends on mass through the parameter $\mathcal{M} = \eta^{3/5} M$, which is referred to as the chirp mass.

1.3 Detection of Gravitational Waves using Advanced LIGO ²

The Advanced LIGO (Laser Interferometer Gravitational Wave Detector) instruments are currently two in number, One of them is located in Hanford, WA (H1) and the other in Livingston, LA (L1). A third detector that became recently operational is called Virgo and is located in Tuscany Italy. The LIGO detectors work on the principle of Michelson Interferometers. They comprise two orthogonal arms each containing two mirrors which act as test masses, separated by a distance of $4 \text{ km} = L_x = L_y$. A small change in the relative arm length i.e, $\Delta L = \delta L_x - \delta L_y = h(t)L$ due to a passing gravitational wave, can be measured as the strain signal $h(t)$. This is possible because this differential

²This section closely follows [3], [1], for more information on improvements done for advancedLIGO, please see [5]

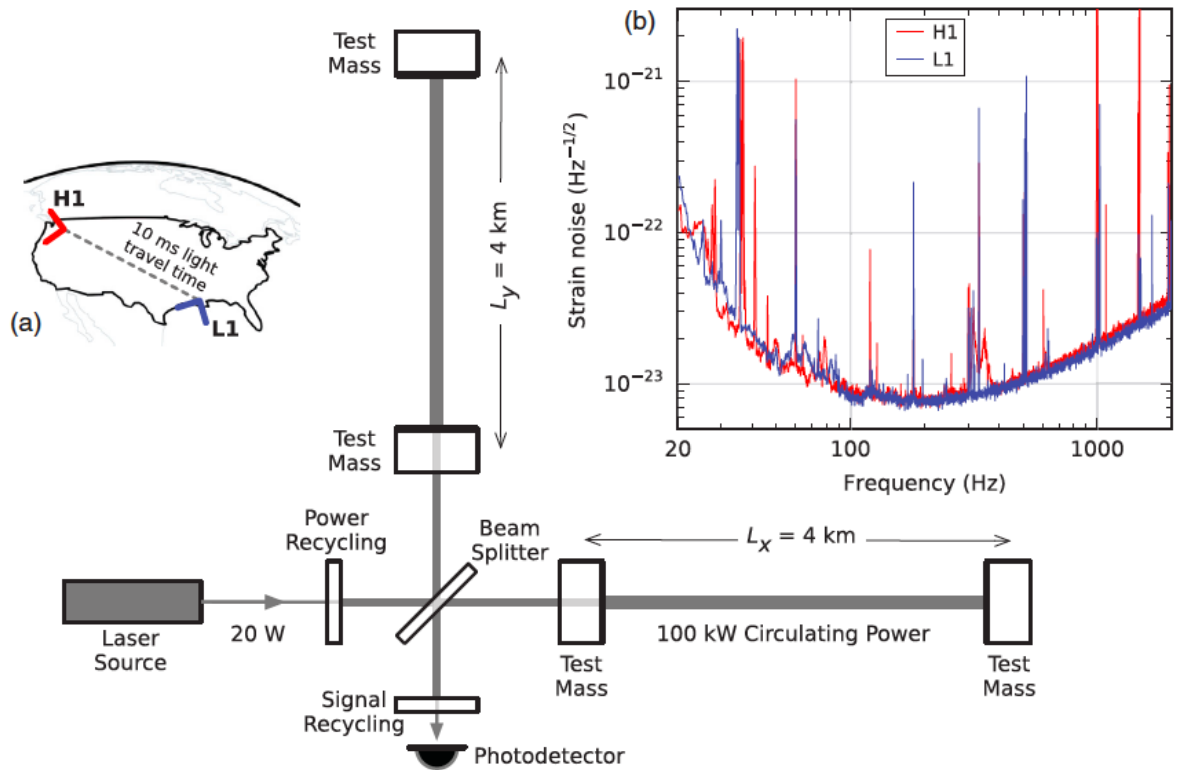


Figure 3 : [3]A simplified diagram of the Advanced LIGO detector. *Inset.* (a) Location and orientation of the detector at Hanford, WA (H1) and LLivingston, LA (L1). (b) The instrument noise for each detector.

change in length of the arms, shifts the phase between the interfering laser beams which return to the beam splitter, thus transmitting an optical signal which is converted to an electrical signal with the help of photo detectors. The amplitude of this electrical signal is proportional to the strain $h(t)$.

Several enhancements needed to be made to the basic Michelson Interferometer design so as to make the detectors sensitive enough.

1. Each arm contains a resonant optical cavity that multiplies the effect of gravitational waves on the shift of phases of the light by a factor of 300.
2. A power-recycling mirror is placed at the input, which is partially transmissive and provides additional resonant buildup of the laser light in the interferometer, this causes 20 W of laser input to be finally increased to 100 kW circulating in each arm.
3. A partially transmissive signal-recycling mirror at the output, helps optimize the

gravitational wave signal extraction by broadening the bandwidth of the arm cavities.

4. The interferometer used a 1064 nm Nd:YAG laser that is stabilized in amplitude frequency and beam geometry.
5. The gravitational wave signal is extracted at the output using a homodyne readout. These interferometry techniques help tackle photon shot noise, the principle high frequency noise source.
6. Lowering of displacement noise is achieved by isolating the test masses from low frequency seismic noise and designing them to have low thermal noise at intermediate frequencies. Each test mass is suspended as the final stage of a quadruple-pendulum system, supported by an active seismic isolation platform. These isolation techniques collectively provide 10 orders of magnitude of decoupling from ground motion above 10Hz.
7. Thermal noise is minimized by using low-mechanical-loss materials in the test masses and their suspensions.
8. To further minimize additional noise sources, all components other than the laser source are mounted on vibration isolation stages in ultra high vacuum.
9. Optical fluctuations and Raleigh scattering are reduced by maintaining a pressure of $1 \mu Pa$ in the 1.2 m diameter tubes containing the arm cavity beams.
10. Servo controls are used to hold the arm cavities in resonance and to maintain proper alignment of optical components.
11. A modulated calibration laser is used to measure the test mass response to photon pressure, in strain, and such uncertainty is maintained below 1σ .
12. the detectors response to gravitational waves is tested by injecting simulated waveforms with the calibration laser.

Other than this, the observatories are equipped with several monitors and sensors including, seismometers, accelerometers, magnetometers, microphones, radio receivers, ac power line monitors and cosmic-ray detectors. The data collection is synchronized to Global Positioning System (GPS) and is verified by an atomic clock.

1.4 Organization of this dissertation

This dissertation is organized in the following way:

In chapter 2 We summarize the studies undertaken to understand the sensitivity of a combined search for stellar mass and Intermediate mass types of compact objects.

In chapter 3 We investigate the possible existence of a gap in component masses of compact objects in the range $3-5 M_{\odot}$ by trying to find posterior support for events in such a gap. The gap is hypothesized as progenitor stars for compact objects in such a mass range are expected to explode in supernovae leaving no remnants.

In chapter 4 we describe the design and construction of the template bank used by the GstLAL-based inspiral pipeline in O2. We summarize the investigations that lead to such a design.

In chapter 5 We study the difference in sensitivity between the search for Intermediate mass black hole binaries in the 1st observing run of LIGO (O1) vs in the 2nd observing run (O2). We also investigate the effect of including higher order modes in the simulated waveforms used to estimate the sensitivity of the search.

In chapter 6 We briefly describe other contributions made to the first and the second observing runs of LIGO.

Chapter 2

Towards a combined stellar mass and intermediate mass search and its effect on the spacetime volume sensitivity of the search

2.1 Introduction

This is a study involving a heuristic combination of the intermediate mass binary black-hole (IMBBH) search bank, with the stellar mass search bank, to form a combined search template bank. Such a combined bank was then used to run over the first 16 days of data from the first observing run of advanced LIGO, using injections representing different populations of binaries. The sensitivity of this combined bank was studied mainly with respect to the IMBBH population of simulated signals, also called injections and this was compared with the sensitivity of the IMBBH bank. The behaviour of the relative sensitivity of the combined search with respect to IMBBH search, was found to be dependent on the total masses of the injections, prompting a possible mass-based weighting of the ranking statistics.

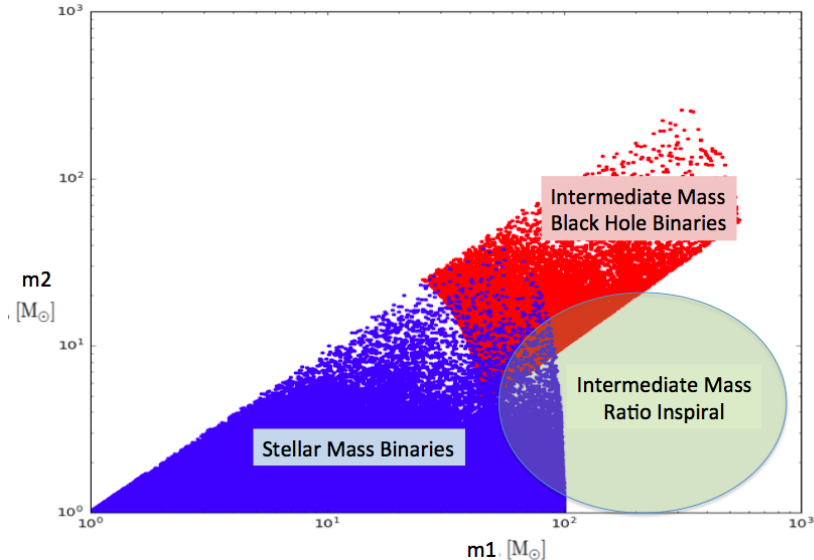


Figure 4 : A visual representation of the different searches in the log of the component mass space.

Search type	Range of total mass of binaries (M_{\odot})	type of template bank	number of templates
stellar mass	2-100	stellar mass	249077
IMBH	50-600	IMBH	44902
stellar mass + IMBBH	2-600	stellar mass + IMBBH	293979

Table 1 : Mass range and number of templates of the stellar and IMBBH search bank used for O1 and the combination of these.

2.2 Background

The different searches undertaken by Advanced LIGO are shown in Fig. 4. The gstlal pipeline uses matched filtering with designated template banks. The basic properties of the different template banks for the stellar search, done using the stellar mass bank and the intermediate mass binary black hole search (IMBBH search), done using the IMBBH bank, as used for advanced LIGO’s first observation run (O1), are shown in table 1.

Intermediate mass black holes (IMBHs) have a mass range of a few tens to about $10^5 M_{\odot}$. The IMBBH search currently, is sensitive to a total mass range of 50-600 M_{\odot} . The stellar mass search is sensitive to a total mass range of 2 to 100 solar masses. It has been a priority to combine these major searches together efficiently, so as to save analysis time and cost. A combined bank called Hyper bank was already used for O2, but here we will focus on the studies done with the intention of the construction of a basic combined bank by simply adding the two existing banks and testing to see how the search sensitivity changes for various populations of astrophysical objects.

Search parameters	stellar mass search	IMBH search	IMBH+stellar
lower cut off frequency (f_low)	30Hz	15Hz	15Hz
Gating of glitches threshold	50 standard deviations	no gating	no gating
Approximants	TaylorF2 [6], SEOBNRv2- ROM_DoubleSpin [7]	SEOBNRv2- ROM_DoubleSpin	TaylorF2, SEOBNRv2- ROM_DoubleSpin
\mathcal{M} boundary between 2 approximants	1.73	none	4.00
total template bins	200	100	100
number of χ bins	20	10	10
number of split banks in an svd bin	5	10	10

Table 2 : Differences between the three searches. SVD grouping of templates is explained in chapter 4. The parameters for the search using the combined bank, were kept mostly the same as for the IMBH only search.

2.2.1 Combined search

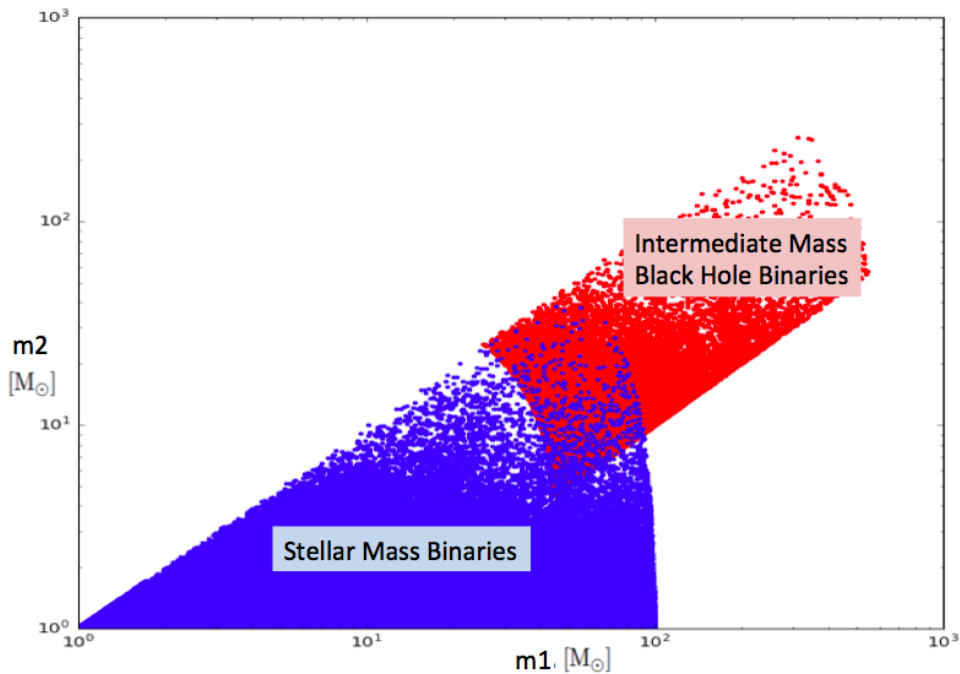


Figure 5 : Visual representation of a combined bank made by adding IMBBH and the stellar mass bank, in the component mass space.

A combined bank was constructed by simply concatenating the IMBH and stellar mass banks, as shown in Fig. 5. The combined analysis was mostly kept same as the IMBH, but there were slight differences. These have been indicated in table 2. The low cut off frequency (f_low) of the waveform, used for the analysis to avoid running into low frequency noise, was kept 15 Hz for both IMBH and combined searches, but was set at 30Hz for the stellar mass search. This is because, the stellar mass systems have longer waveforms and merge at higher frequencies. The SVD splitting for the combined

Search type	FAR	FAP	ln Λ	combined SNR	m1 m2 (M_{\odot})
stellar mass	3×10^{-39}	5.09×10^{-33}	84.7	24.03	47.93, 36.60
IMBH	4.48×10^{-33}	7.5×10^{-39}	66.4	22.85	67.37, 12.92
stellar mass + IMBH	5.8×10^{-32}	1.06×10^{-25}	68.9	22.99	54.44, 14.31

Table 3 : The False Alarm Rate (FAR), False Alarm Probability (FAP), log likelihood ($\ln \Lambda$), Signal to noise ratio (SNR) and component masses, compared between three searches for GW150914 event.

Search type	FAR	FAP	ln Λ	combined SNR	m1 m2 (M_{\odot})
stellar mass	5.63×10^{-09}	9.52×10^{-3}	18.1	9.86	50.09, 8.69
IMBH	1.76×10^{-11}	2.96×10^{-05}	19.2	9.94	40.09, 11.10
stellar mass + IMBH	8.48×10^{-10}	1.54×10^{-3}	19.9	10.04	40.09, 11.10

Table 4 : The False Alarm Rate (FAR), False Alarm Probability (FAP), log likelihood ($\ln \Lambda$), Signal to noise ratio (SNR) and component masses, compared between three searches for LVT151012 candidate. It is clear that the combined search seems to assign it a lower FAR (hence higher significance) than the stellar mass search and a slightly higher FAR than the IMBH search.

search, as explained in chapter 4 was kept the same as the IMBH run. The waveform approximants used were the same as the IMBH search, but the value of \mathcal{M} above which SEOBNR type waveforms [7] is used and below which TaylorF2 type waveform [6] is used, had to be increased to 4 for the combined run, as against 1.73 for the stellar run. This is because the lower cut off frequency was reduced from 30Hz in case of stellar to 15Hz in case of IMBH and combined, while the product of total mass and lower cut off frequency has a lower limit of 0.0005 Hz for ROM type waveforms to work. This is a result of the fact that the parameter space was expanded to include heavier mass systems, which merge at lower frequencies and have shorter waveforms, and so the lower frequency limit from which to start the analysis, had to be lowered.

This was used to search over the first 16 days of O1 data with GPS time range 1126051217-1129383017 (chunks 123).

2.2.2 Comparison of ranking between the searches

Much speculation has been going on regarding the LVT151012 candidate and its origin is still unclear. However from table 4 the combined search seems to assign it a lower FAR (hence higher significance) than the stellar mass search and a slightly higher FAR than the IMBH search. This inspired a study of the relative sensitivity of the two searches (combined and IMBBH) towards different populations of astrophysical objects. The idea

was to inspect how the overall search sensitivity changes by combining the searches.

2.3 Study of the sensitivity of different template banks to various simulations

This is a study that aims to contribute to the correct generation of the combination of the stellar mass and IMBBH banks. Here I studied how sensitive the different banks, i.e, the IMBBH, stellar mass and the combination of the two, are to signals from different populations of binaries.

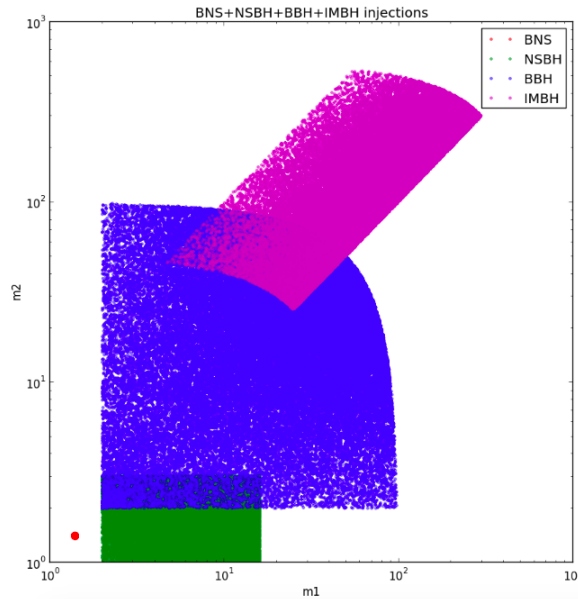


Figure 6 : A visual representation of the binary populations for which simulated waveforms were used, in the component mass space, in solar masses.

Volume sensitivity plots which show the volume in space and time that the detector is sensitive to, are generated by the GstLAL-based inspiral pipeline during an analysis run. The plots are generated for both real data and the simulations that are mixed in to test the sensitivity of the search pipeline.

The plots obtained for the injections, using both the stellar mass and IMBH banks are shown in Fig. 7 and 8.

A separate code using Monte Carlo integration was written to recreate these plots using only the injections. This was done to check if the pipeline's method of calculating

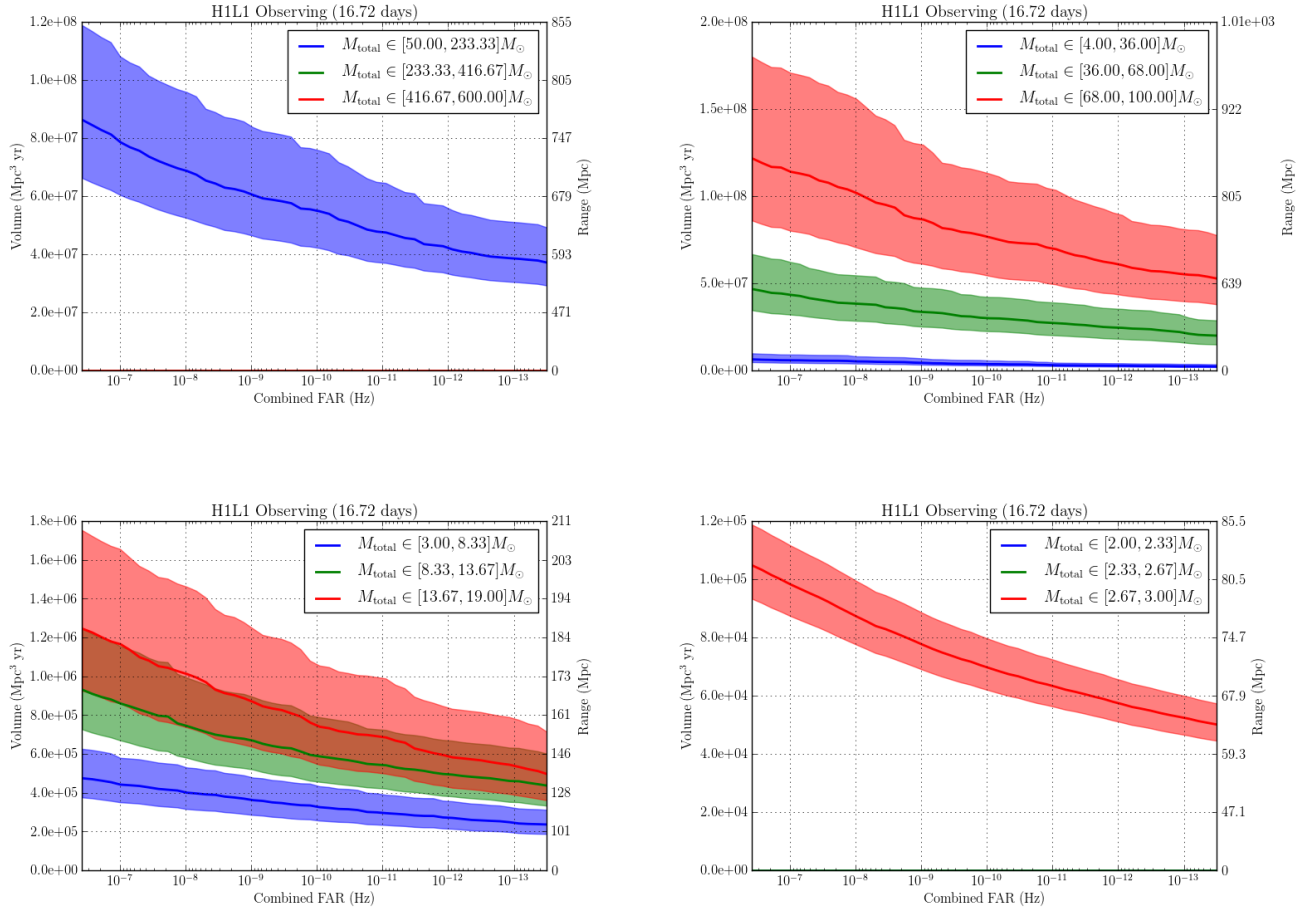


Figure 7 : Volume sensitivity vs CFAR plots using IMBH, BBH, NSBH and BNS injections with a stellar mass search bank (generated from GstLAL-based inspiral pipeline)

volume sensitivity is accurate.

This was followed up by writing an independent code to recreate the plots in the same way as the pipeline does, to check for consistency between all three methods of calculating volume sensitivity of the search.

2.3.1 Using Monte Carlo Integration

The basic method of Monte Carlo Integration states that the integral of a function f over multidimensional volume V is given by [8] :

$$\int f dv \approx V \langle f \rangle \pm V \sqrt{\frac{\langle f^2 \rangle - \langle f \rangle^2}{N}} \quad (2.3.1)$$

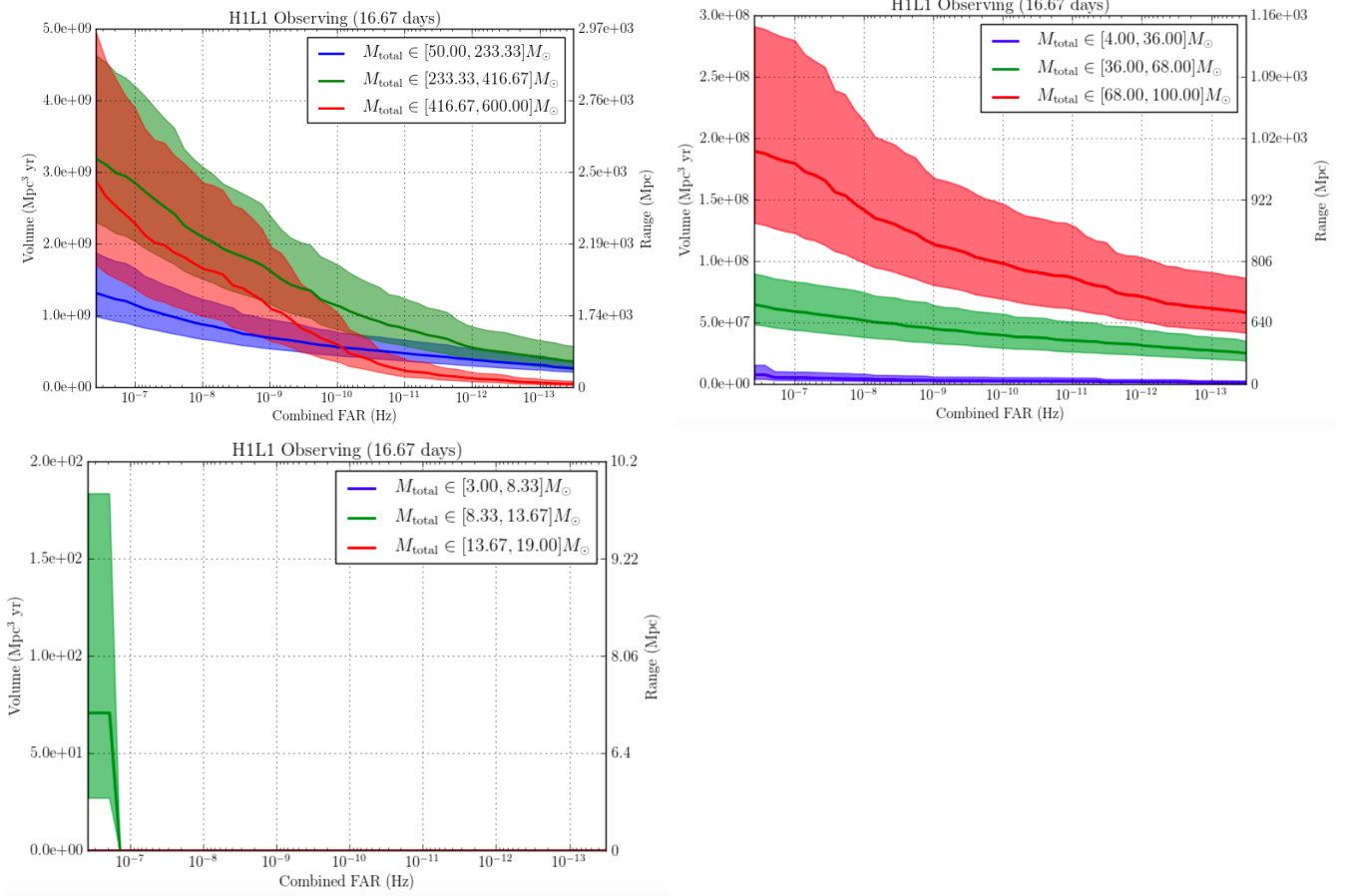


Figure 8 : Volume sensitivity vs CFAR plots using IMBH, BBH, NSBH and BNS injections with a IMBH search bank (generated from GstLAL-based inspiral pipeline)

where N random points x_i are uniformly distributed in V ,

$$V = \int dx \quad (2.3.2)$$

is the coordinate volume, where x is a multidimensional variable.

$$\langle f \rangle = \frac{1}{N} \sum_{i=1}^N f(x_i) \quad (2.3.3)$$

$$\langle f^2 \rangle = \sum_{i=1}^N f(x_i)^2 \quad (2.3.4)$$

Here volume refers to spacetime volume. The integral we are interested in computing looks like:

$$Volume = \int_{t_{min}}^{t_{max}} dt \int_{r_{min}}^{r_{max}} r^2 dr \int_{-1}^1 d(\cos\theta) \int_0^{2\pi} d\phi \quad (2.3.5)$$

The method used by the independent code to calculate volume sensitivity using Monte Carlo integration:

$$Volume = V \Delta T \frac{\sum_i^{c < c_n} r_i^2}{N_{inj}} \quad (2.3.6)$$

where,

$$V = \int_{r_{min}}^{r_{max}} dr \int_{-1}^1 d(\cos\theta) \int_0^{2\pi} d\phi \quad (2.3.7)$$

$\sum_i^{c < c_n} r_i^2$ = cumulative $\sum r_i^2$ for CFAR < nth CFAR (Combined False Alarm Rate),
 N_{inj} = total number of injections in a specific bin, ΔT = time duration of injections.

Hence

$$Volume = 4\pi(r_{max} - r_{min})\Delta T \frac{\sum_i^{c < c_n} r_i^2}{N_{inj}} \quad (2.3.8)$$

However, if the function to be integrated, f in equation 2.3.1 is such that x_i points are not uniformly distributed, then this distribution has to be accounted for by multiplying a weight factor to the function to be integrated. Let this weight function be $w(x)$. Then any integral over f can be written as:

$$\int f dx = \int \frac{f(x)}{w(x)} w(x) dx \quad (2.3.9)$$

Then equation Eq. (2.3.1) gets modified as:

$$\int f dv \approx V \left\langle \frac{f}{w} \right\rangle \quad (2.3.10)$$

where $V = \int w(x) dx$ is the multidimensional volume.

Doing this for the integral Eq. (2.3.5):

$$Volume = \int_{r_{min}}^{r_{max}} w(r) dr \int_{-1}^1 d(\cos\theta) \int_0^{2\pi} d\phi \Delta T \frac{1}{N_{inj}} \sum_i^{c < c_n} \frac{r_i^2}{w_i} \quad (2.3.11)$$

which has the same form as Eq. (2.3.6) if

$$V = \int_{r_{min}}^{r_{max}} w(r) dr \int_{-1}^1 d(\cos\theta) \int_0^{2\pi} d\phi \quad (2.3.12)$$

and r^2 is replaced by $\frac{r^2}{w(r)}$, where $w(r)$ is the weight factor taking care of the nonuniform distribution of r .

Using the Monte Carlo integration method, as shown in Eq. (2.3.1), and doing the integrals over θ and ϕ we can compute this V as:

$$V = 4\pi(r_{max} - r_{min}) \frac{\sum_{i=1}^{N_w} w_i}{N_w} \quad (2.3.13)$$

putting this back in Eq. (2.3.11) gives:

$$Volume = \frac{4\pi\Delta T(r_{max} - r_{min})}{N_{inj}} \frac{\sum_{i=1}^{N_w} w_i}{N_w} \sum_i^{c < c_n} \frac{r_i^2}{w_i} \quad (2.3.14)$$

The injection set for IMBBH and BNS were uniformly distributed in r but that for BBH and NSBH were uniformly distributed in r_{chirp} , which is the distance dependent factor ($GM/2c^2r$) in the plus and cross polarization amplitudes for the radiation. Hence the distribution for r in case of BBH and NSBH were taken into account by using a histogram of r as weight factor $w(r)$ as described above.

An example of a plot from independent Monte Carlo integration method code is shown in Fig. 9. The volume sensitivity obtained using the Monte Carlo code seem to be higher and that obtained by the GstLAL-based inspiral pipeline in Fig. 8. As we shall see, this is a result of the fact that a pruned or optimized injection set was used by the pipeline and the time segments were added accordingly by the pipeline, which was not done by our naive Monte Carlo code initially.

2.3.2 Using the efficiency parameter method used by the pipeline

The pipeline's way of calculating the sensitive volume [9] uses the following equation:

$$V = 4\pi \int_0^\infty dr r^2 \epsilon(r) \quad (2.3.15)$$

where $\epsilon(r)$ is defined to be an efficiency parameter giving the ratio of found to total simulations injected at a distance r . This is equivalent to computing:

$$Volume = 4\pi\Delta T \sum_j^N [(j + 0.5)\Delta r]^2 \Delta r \epsilon_j \quad (2.3.16)$$

where N is the total number of r bins, Δr is the bin size of histograms of r with which the simulations were recovered and injected. The index j runs over the distance bins. We

find these histograms of injected and found distances, with the same bin boundaries, so that simply dividing them, gives us $\epsilon(r)$. As in the Monte Carlo case, we compute this volume for r less than different CFAR values and then plot volume Vs CFAR.

2.4 Investigations and conclusions Using IMBH run with IMBH injection set

The IMBH injection set used to complete the GstLAL-based inspiral pipeline run was actually pruned. The pruning had been done to remove injections that were too far away to observe, or had low expected SNRs and were going to be missed. So to compute the efficiencies and hence sensitive volume in this method, one has to be careful to use the pruned injection file with the correct time segments, rather than the complete injection set, as in the latter case, the number of injections being higher, the efficiency will drop and will be lower than what the pipeline calculates. The various stages of this work and the progressive realization of various factors effecting the sensitivity has been described below.

2.4.1 Using the original full injection set and the pruned set

The Volume sensitivity Vs CFAR plots obtained using independent code replicating the pipeline's efficiency method, (hence forth referred to as the efficiency code) while considering the full IMBH injection set (left panel) and the pruned injection set (right panel), have been described below in Fig. 12. Fig. 11 is the same plot obtained from the GstLAL-based inspiral pipeline, as shown before in Fig. 8. and has been included here for comparison. Fig. 15 represents the volume sensitivity vs CFAR plot generated by the GstLAL-based inspiral pipeline for an IMBH only search using the full IMBH injection set. We expected Fig. 11 to match right panel of Fig. 12 and Fig. 15 to match left panel of Fig. 12. However, we can see that the right panel of Fig. 12 i.e the result of the efficiency code using the pruned injection set is very similar to what is obtained by the Monte Carlo code in Fig. 9. We also obtain the Monte Carlo plot with the full injection set and our results agree with the efficiency code results for the full injection set as shown in the left panel

method of calculating volume sensitivity	Volume sensitivity (for middle mass bin) at CFAR of 10^{-7}
gstllal pipeline (pruned injection set)	2.9×10^9
Monte Carlo Method (full injection set)	1.2×10^9
Monte Carlo Method (pruned injection set)	5.3×10^9
efficiency method (full injection set)	1.2×10^9
gstllal pipeline (full injection set)	1.2×10^9
efficiency method (pruned injection set)	5.5×10^9
efficiency method (pruned, with correct segments and livetime)	2.8×10^9

Table 5 : Comparison of Volume sensitivity obtained from different methods at CFAR of 10^{-7} for the middle mass bin, for IMBH run with IMBH injections. We see that for the full injection set, the results from the three different methods agree. For the pruned set, they agree between the Monte Carlo and the efficiency method, but not with the pipeline results.

of Fig. 12. Hence though the efficiency code and the Monte Carlo code agree for both the pruned and the full IMBH injection sets, they both agree with the pipeline results only in case of the full injection set and not the pruned set.

A tabular comparison of some of the results from the plots obtained from the three different methods is presented in table 5.

Though we expected the plot for the pruned set from the efficiency and Monte Carlo methods to tally with the plot from the pipeline, but this didn't happen. This is because, the pipeline removes vetoed segments of data from the stream and adjusts the total time accordingly, which was not being done initially by our independent codes.

2.4.2 Diagnostic plots to understand difference between pruned and full IMBH injection sets

We look at a few diagnostic plots before generating new plots removing vetoes. A good plot to look at is the efficiency parameter ϵ vs injection distance, as shown for the total injection set and the pruned set in Fig. 13. It shows us how much the efficiency parameter changes on pruning.

Another diagnostic plot was made to understand the difference between the pruned injection set and the full set. An efficiency was calculated using the pruned set as the found and the full set as the injected. So here the “effective efficiency” like quantity is the number of injections left after pruning in a bin over the total number of injections in that bin. The plot obtained using logarithmic distance binning is shown in Fig. 14. The usual efficiency is shown in red. The green line shows a “maximum efficiency” possible if

all the injections expected to be found after the pruning, were indeed found.

2.4.3 Regenerating the pipeline plot using the full injection set

The pipeline plot last shown in Fig. 11 was regenerated using the full IMBH injection set as shown in Fig. 15

The plot obtained using Monte Carlo integration and using the efficiency code for full IMBH injection set are included in Fig. 16 and Fig. 17 for comparison. These have been shown in earlier figures as well. All three methods seem to be in agreement for the full injection set.

But as pointed out before, Fig. 11 depicting the gstlal pipeline plot for the pruned does not seem to be agreeing with the left panel of Fig. 12, the plot obtained from efficiency code. We address this at the end.

2.4.4 Comparison of all three methods for IMBH run using IMBH injections

We can see Fig. 18 shows an overlay of Volume Vs CFAR plot made using all three methods, using full IMBH injection set, for IMBH search. The three methods seem to agree for the full IMBH injection set.

2.4.5 Folding in a trials factor for IMBH run with IMBH injection results

Finally, we want to compare the sensitivity of the IMBH search with the sensitivity of the combined search, using the same injection set i.e IMBH. But since the combined search is a combination of two independent searches, i.e stellar mass search and IMBBH search, hence to compare the combined search sensitivity with either of them. To compare with the IMBH search sensitivity, we have to fold in a trials factor of 2 for the CFAR values of the IMBH sensitivity plot. This causes the volume vs CFAR plot for IMBH analysis, to shift left, i.e towards higher CFAR values or lower significance. So the same events are now recovered with a higher CFAR, after taking the two independent searches into consideration. This is also physically justified as a bigger search has more accidentals and hence the sensitivity goes down, or in other words, the CFAR goes up. Fig. 19 shows the shift due to folding in the trials factor. This is a conservative estimate and we expect

the sensitivity of the combined search to be higher than the trials adjusted estimation of the IMBH search sensitivity. It is conservative because it assumes the IMBH and stellar mass searches to be independent, but as we can see from Fig. 5, the two searches overlap.

2.4.6 Comparison between IMBH and combined search sensitivities for IMBH injections

Comparing overlay plots

In order to do this comparison, we will first look at plots that overlay the Volume Vs CFAR plots for IMBH and combined runs, using the full IMBH injection set, both with and without accounting for the trials factor as shown in Fig. 21 and Fig. 20 respectively. Of course, the plot accounting for the trials factor is the only one that makes physical sense and hence will be used for the said comparison. The other one (without trials factor) is shown, just to show the difference.

It seems that the combined search is more sensitive than the IMBH search, at least at a CFAR of $10^{-7}Hz$, after accounting for the trials factor. This is indeed what we in general expect because a single combined search should be more sensitive than individual IMBH or stellar search results after accounting for the trials factor, since as pointed out earlier, the two “independent searches”, IMBH and stellar mass, accounted for by a trials factor of 2, are really not that independent, having an overlap region in the total mass range of 50 to 100 solar masses.

Next we want to see how the relative volume sensitivity of the combined and IMBH searches vary over CFAR.

Comparing by looking at the ratio plots

We focus on the relative sensitivity plot that accounts for the trials factor in Fig. 23. It is easy to see that if both the combined and IMBH searches were equally sensitive, then the ratio plots, which are plots of the ratios of the volume sensitivity from the two searches, would lie very close to the 1.0 line shown in red. Which also means, that the region lying below the 1.0 line indicates that the combined search is more sensitive, while the region above the 1.0 line indicates that the IMBH search is more sensitive.

The magenta plot denotes the overall trend for the whole injection set, without any mass binning. We can see that for the overall injection set, the combined search is more sensitive almost uniformly over the CFAR window considered.

Similarly, for the lowest mass bin shown in blue, the combined search is more sensitive.

This is not true however, for the highest and the second highest mass bins, shown in red and green. For these mass bins, we see that at lower CFAR values, the IMBH search sensitivity takes over and is higher than the sensitivity of the combined search. But at the high CFAR region, the combined search is still more sensitive. The transition point seems to be close to a CFAR value of $10^{-9}Hz$.

Possible causes for transition of relative sensitivity at low CFAR

We did not fully understand why such a transition was seen at this stage. A few possible explanations were:

1. Change in background noise around $10^{-9}Hz$
2. The combined search is not well designed. A well designed combined search would be more sensitive than the individual IMBH search after folding in a trials factor of 2, since the stellar mass and IMBH searches are not independent. Our combined bank has overlap of the two individual search banks, each of which were made with different search priors, which may have changed the overall prior.
3. The density of templates of the IMBH bank is much lower than the density of templates of the stellar mass bank, since IMBH bank was made with a low cut off frequency (f_{low}) of 15 Hz while the same for stellar mass bank it was 30Hz. Since our combined bank simply adds the two banks without regenerating them, there are regions of vastly varying template densities. The lower template density regions (in

this case, the higher mass region) can easily have higher sensitivity, having lower possibility of accidentals. This is the same reason why the IMBH search is more sensitive in general to stellar mass search.

2.4.7 Comparison of pipeline and efficiency methods for IMBH run using IMBH pruned injections and the mystery of earlier disagreement

As shown earlier, Fig. 11 depicting the GstLAL-based inspiral pipeline plot for the pruned set was not in agreement with the left panel of Fig. 12, the same plot using the efficiency method. This turned out to be so, because, the pruning was not done uniformly in time, but was based on expected SNR. Injections with an SNR value below a detectable threshold, were pruned out. Because of this, simply using the pruned injection set along with the total time of the experiment is not good enough, one has to add data segments the way the pipeline does and also use the correct “live time”, which is less than the total experiment time of 16 days, but is the correct time corresponding to the segments which are obtained by an intersection of the ones found in the two detectors. That is how the pipeline adds the segments.

The pipeline’s unique way of adding the segments matter in the pruned case particularly because of the non-uniformness of pruning in time. Because of this, the ratio of live time to number injected per bin for the coincident segments, is not the same as total time to the number injected per bin, got by simply binning the total number of injections. The ratio of correct live times to number of simulations injected after removing vetoed regions is the same in case of the full injection set, to the ratio of the total time of the experiment to the total number injected and hence we have an agreement between efficiency plot and pipeline plot for the full injection set. The ratio stays the same for the full set even after selecting and adding segments because removal of injection corresponds to reduction of time as segments are removed, which does happen for the pruned set as such pruning is not done uniformly in time. We note that in our code with mass binning, we use the difference between maximum injection time and minimum injection time in a certain mass bin to get the time interval, but this is

approximately proportional to the total experiment time. Also, pruning injections from a certain mass bin will keep this time interval, possibly the same but will reduce total injections, thus giving us a higher value of sensitivity.

Fig. 26 compared with Fig. 11 shows that there is overall agreement even for the pruned injection set, when the veto regions have been taken into account.

2.5 Looking Forward

To summarize, we see the IMBH search being more sensitive at higher significances, than a combined search even after accounting for a trials factor, given the IMBH and stellar searches can be considered independent. Hence the real reason behind the transition of the relative sensitivity needs to be understood .

A more carefully constructed combined search can be executed where the bank is not a naively concatenated version of two other searches. This might redress the problem. Also, mass based weighting can be used to rank candidate events, so that the effect of change of sensitivity with mass can be taken care of.

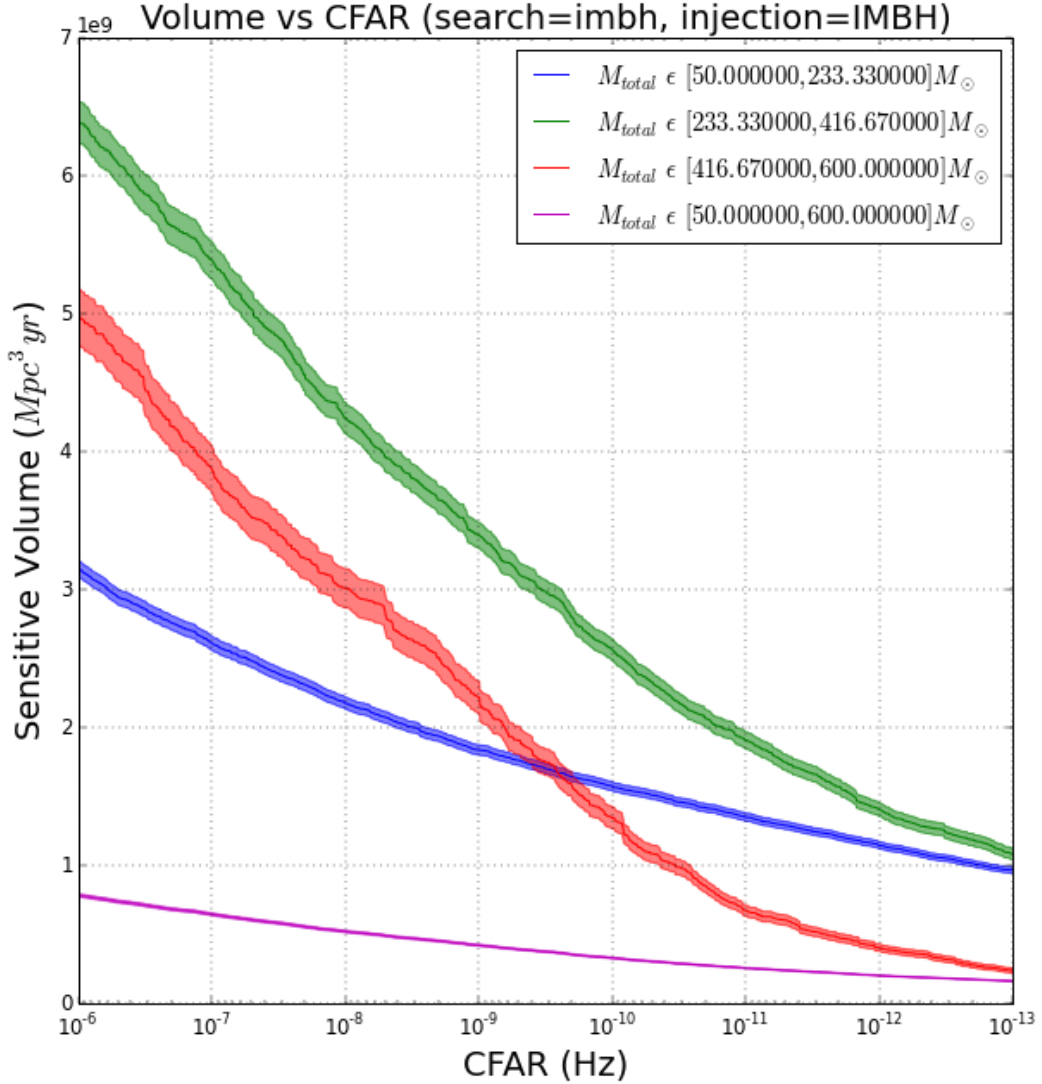


Figure 9 : Volume sensitivity plot using a pruned IMBH injection set with an IMBH bank using Monte Carlo Integration. The volume sensitivity obtained using the Monte Carlo code seem to be higher than that obtained by the GstLAL-based inspiral pipeline in Fig. 8. As we shall see, this is a result of the fact that a pruned or optimized injection set was used by the pipeline and the time segments were added accordingly by the pipeline.

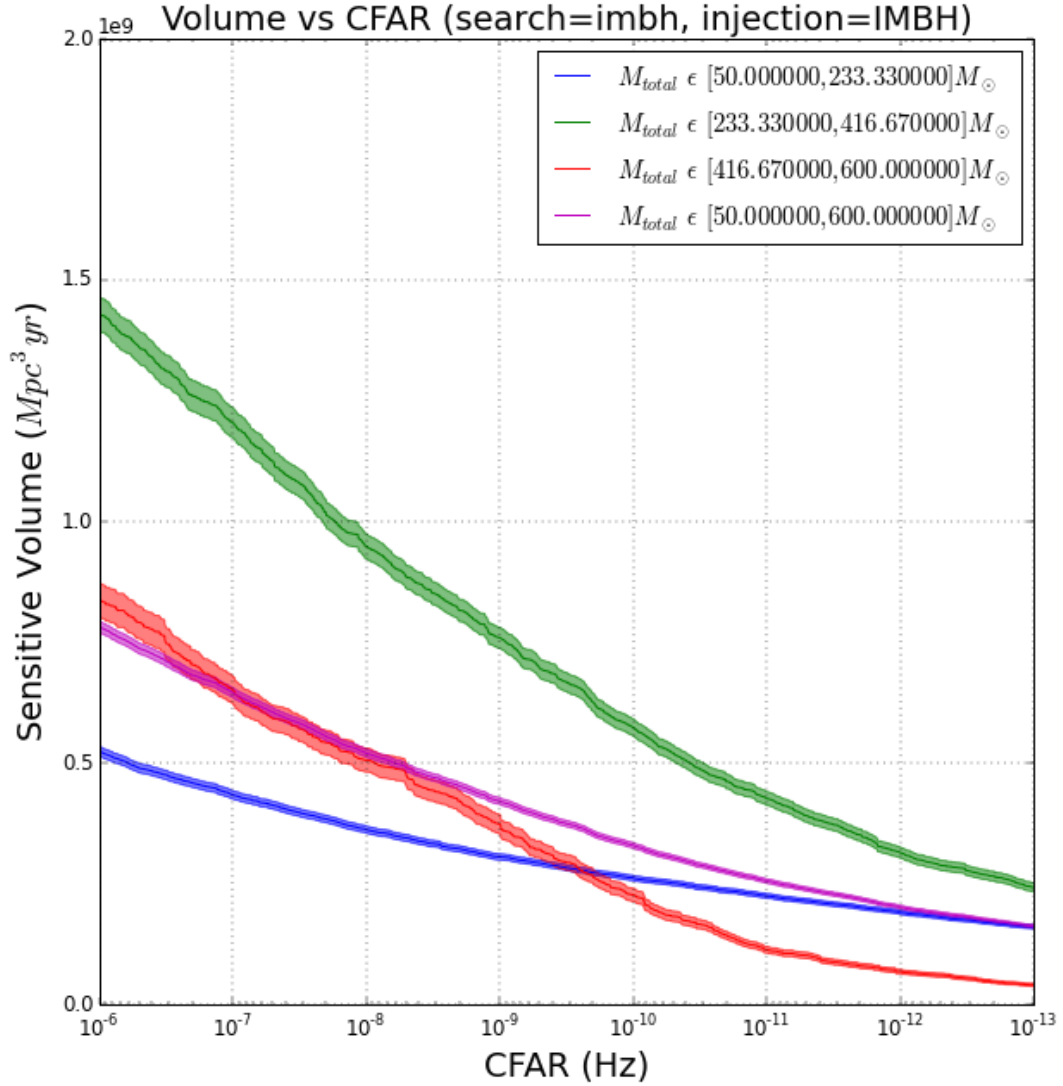


Figure 10 : Volume sensitivity plot using a full IMBH injection set with an IMBH bank using Monte Carlo Integration. This is lower than what was obtained with the pruned set in Fig. 9. The pruned set having fewer injections, causes the ϵ ratio to be higher as the same number of injections are still found. This will agree with the pipeline results only when the correct time segments are added.

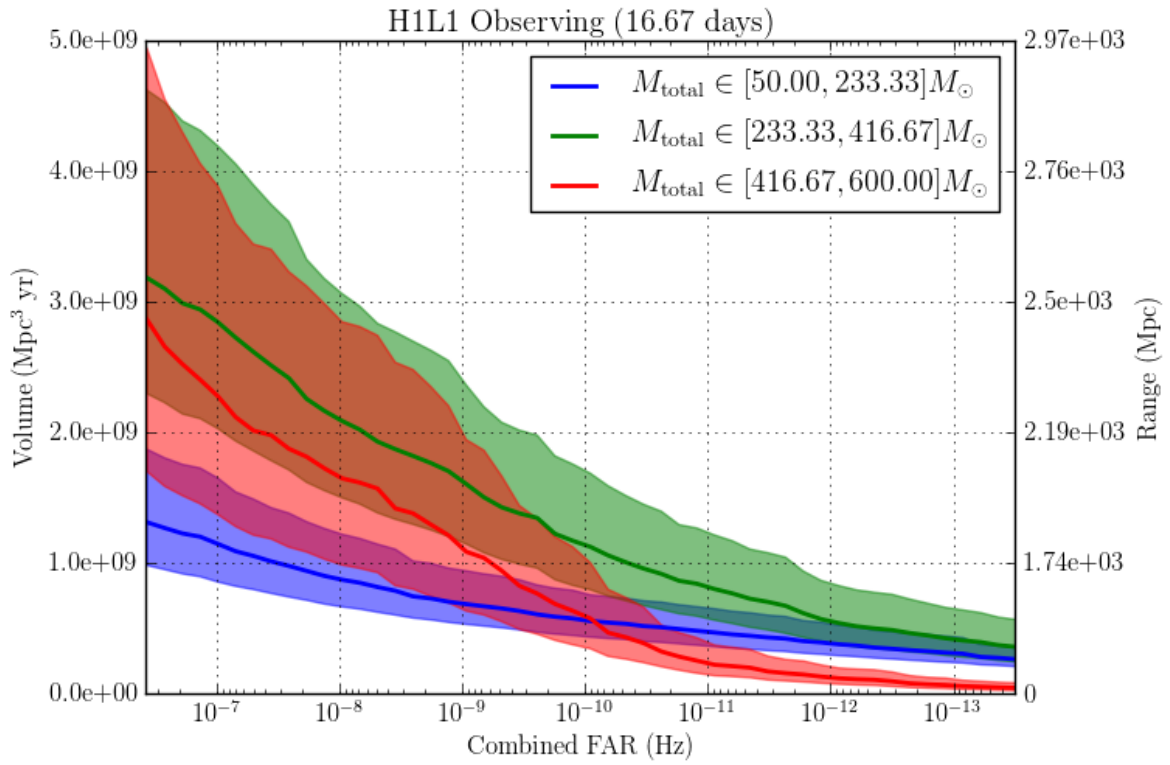


Figure 11 : Volume sensitivity plot using a pruned IMBH injections set with an IMBH bank (from GstLAL-based inspiral pipeline).

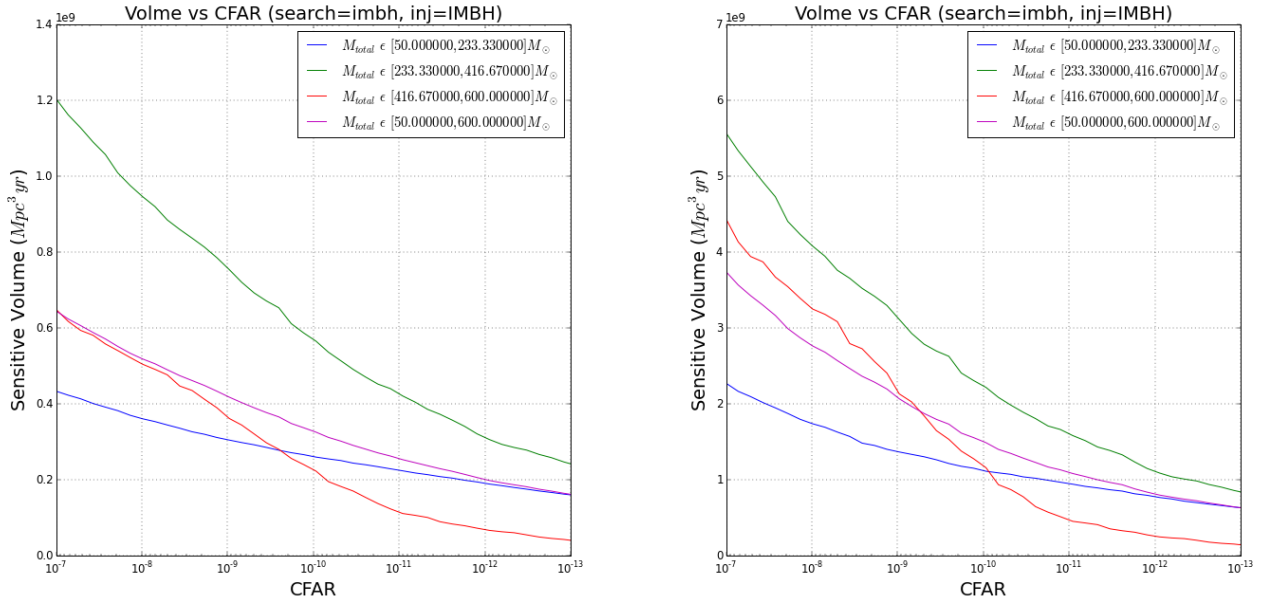


Figure 12 : Volume sensitivity plots using the full IMBH injections (left) and with the pruned IMBH injection set (right) with an IMBH bank (independent efficiency code). In case of a pruned set, the volume sensitivity is higher as fewer injected simulations are considered for the same number of found injections, thus increasing the efficiency. However this increase does not correspond to what is seen by the plot obtained for the pruned injection set by the GstLAL-based inspiral pipeline in Fig. 11. This is because the pruning was not done uniformly in time and the pipeline adds the data segments and their time correctly, which was not naively, initially not implemented by the independent efficiency code.

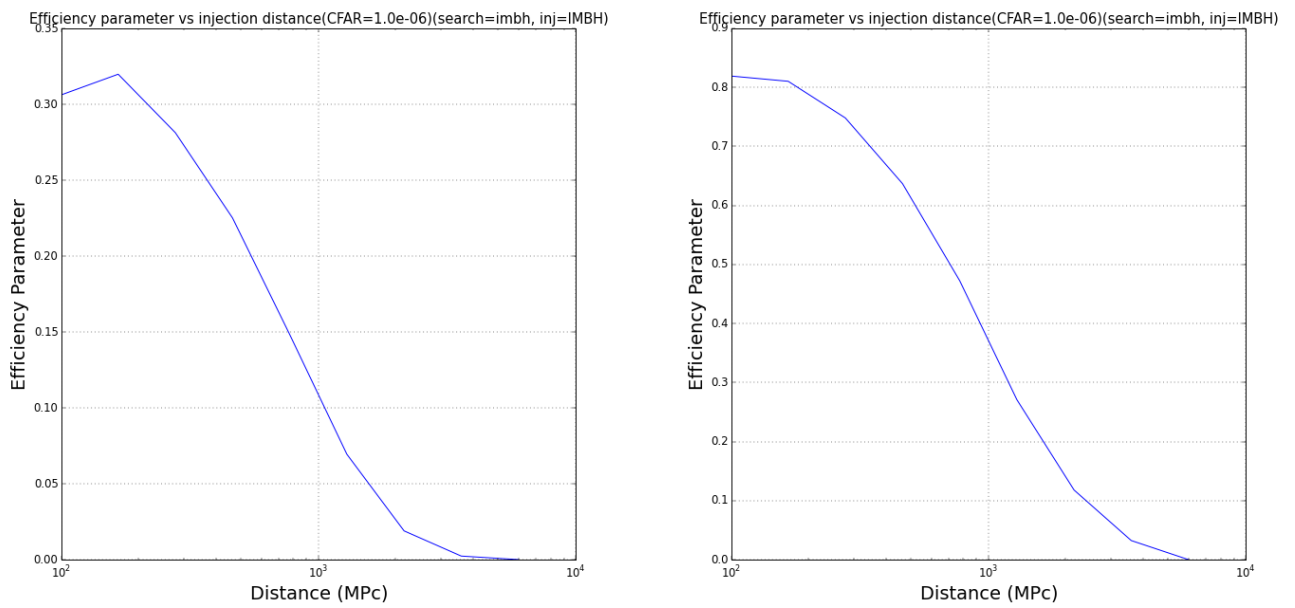


Figure 13 : ϵ vs log of injection distance using full (left panel) and pruned (right panel) injection set. We can see that it is higher for the pruned set, as the calculation of the efficiency ratio still considers the same number of injections to be found as the injections that could be missed were already removed by pruning, while the number injected is higher for the full set, thus lowering the ratio.

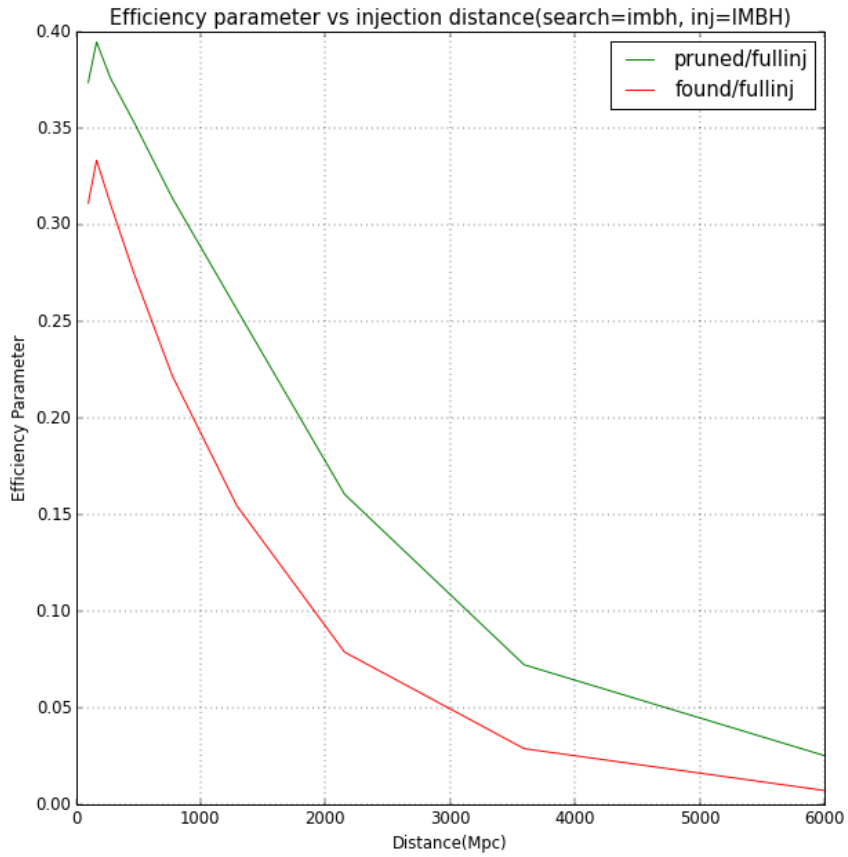


Figure 14 : ϵ vs injection distance using pruned set as found (green) using number of found injections as numerator (red). The usual efficiency is shown in red. The green line shows a "maximum efficiency" possible if all the injections expected to be found after the pruning, were indeed found.

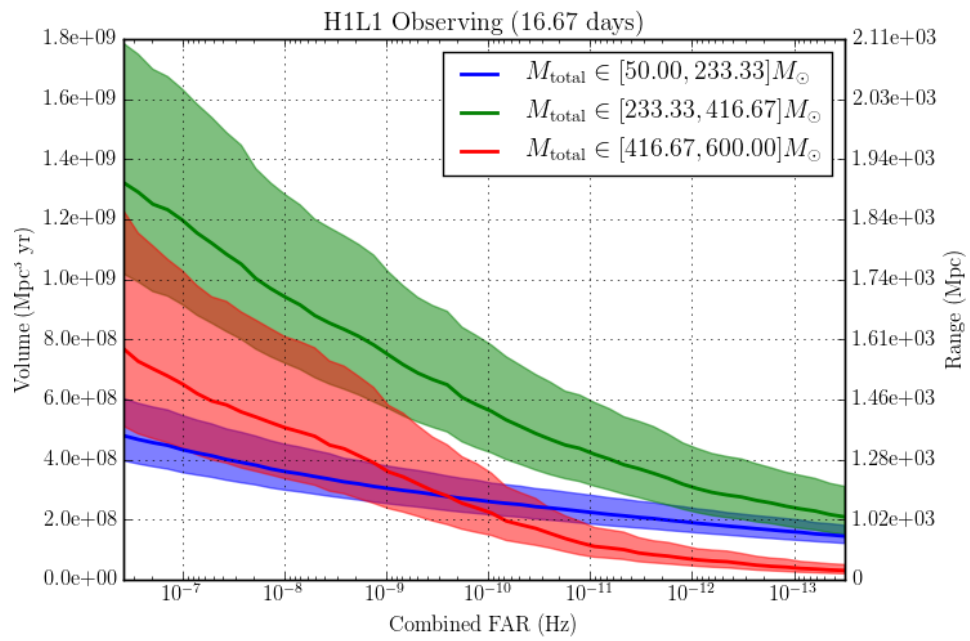


Figure 15 : gstlal pipeline plot regenerated using full IMBH injection set.

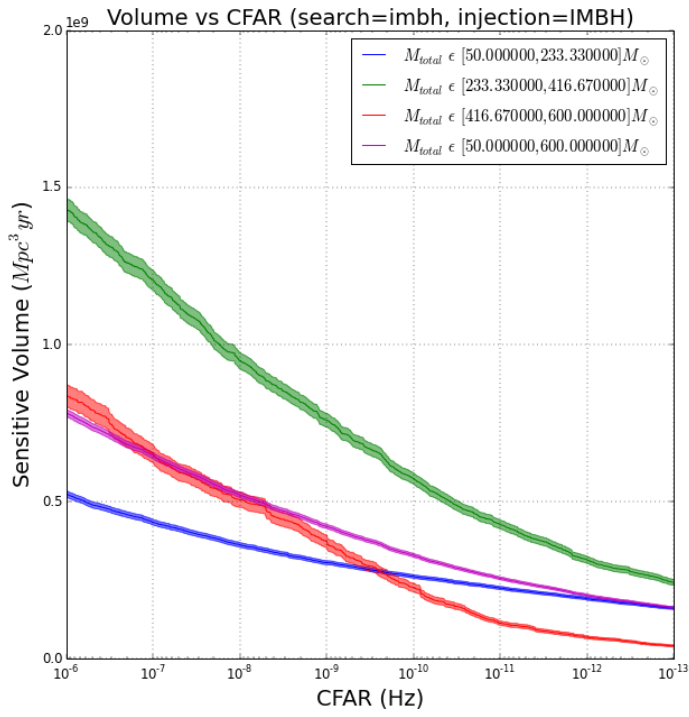


Figure 16 : Volume sensitivity vs CFAR for IMBH run using full IMBH injections (using Monte Carlo Integration)

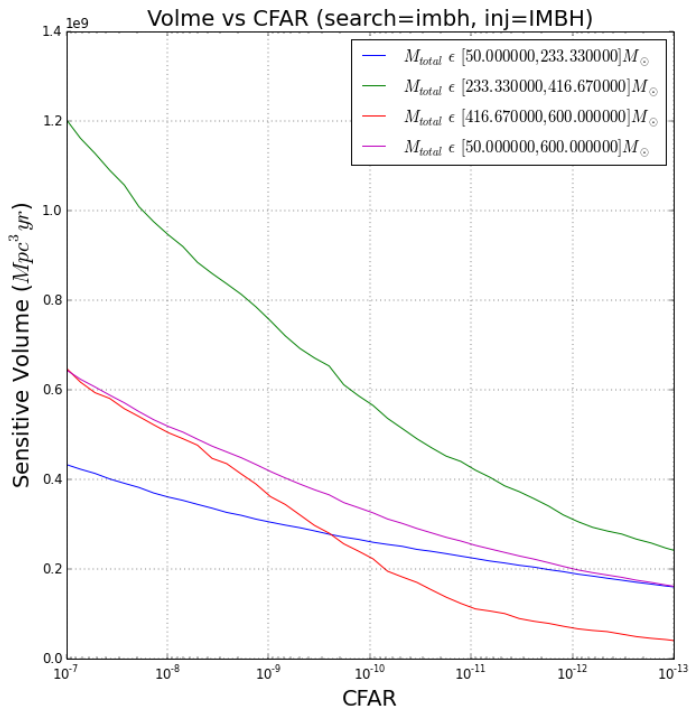


Figure 17 : Volume sensitivity vs CFAR for IMBH run using full IMBH injections (using independent code)

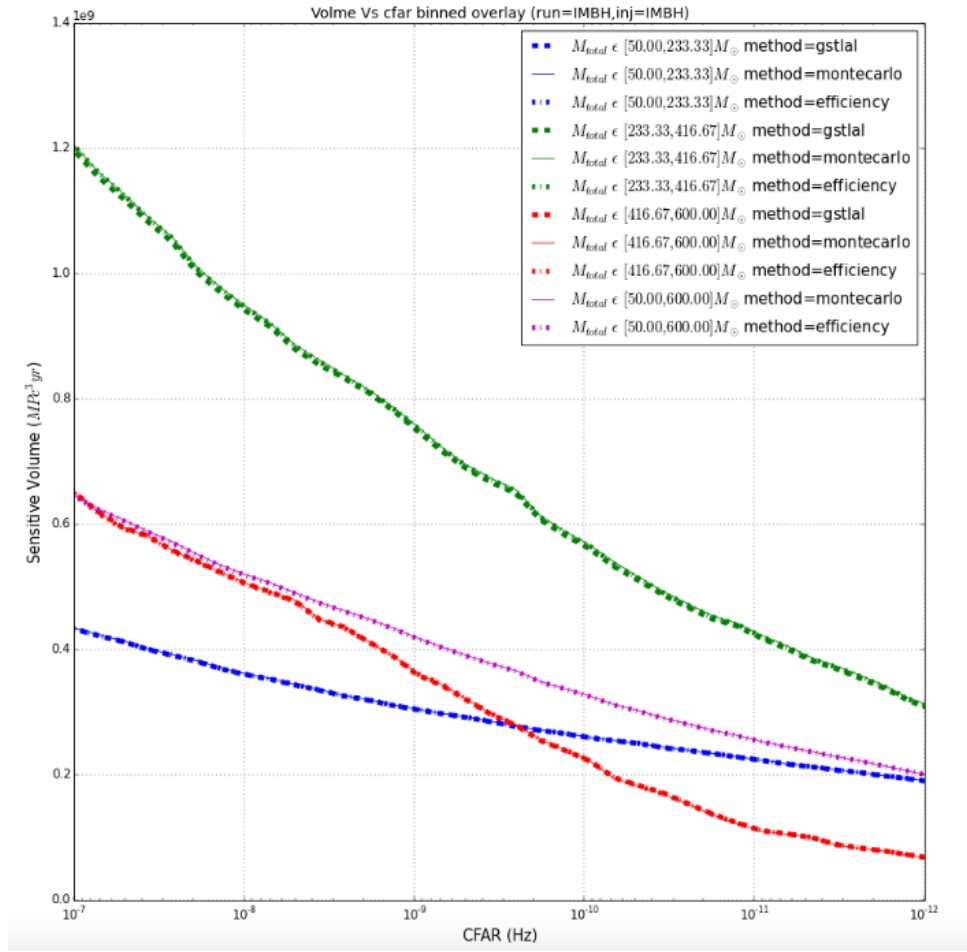


Figure 18 : Overlay of Volume Vs CFAR plot made using all three methods, using full IMBH injection set, for IMBH run. The three methods seem to agree for the full IMBH injection set.

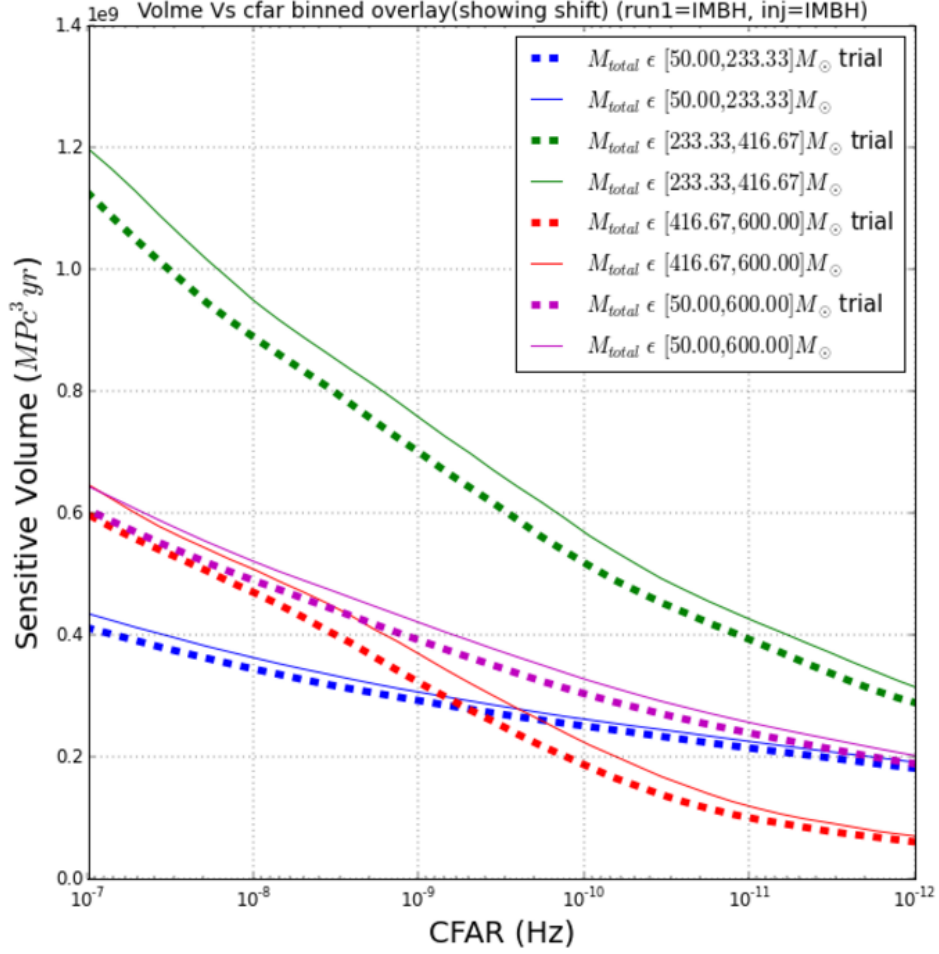


Figure 19 : Shift in the Volume vs CFAR plot using full IMBH injection set, for IMBH analysis, on multiplying CFARs by a trials factor of 2, accounting for the two independent searches, in order to compare with combined search.

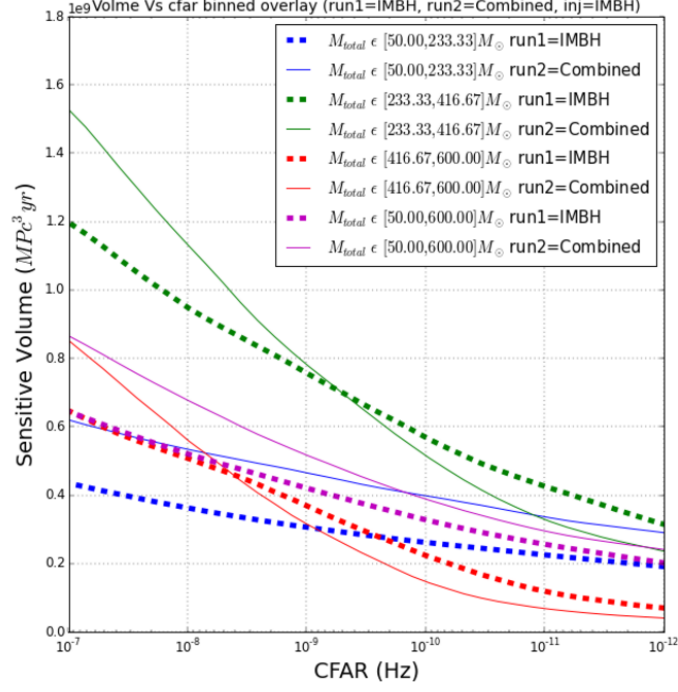


Figure 20 : Overlay of volume sensitivity vs CFAR for IMBH run and combined search using full IMBH injections, without a trials factor.

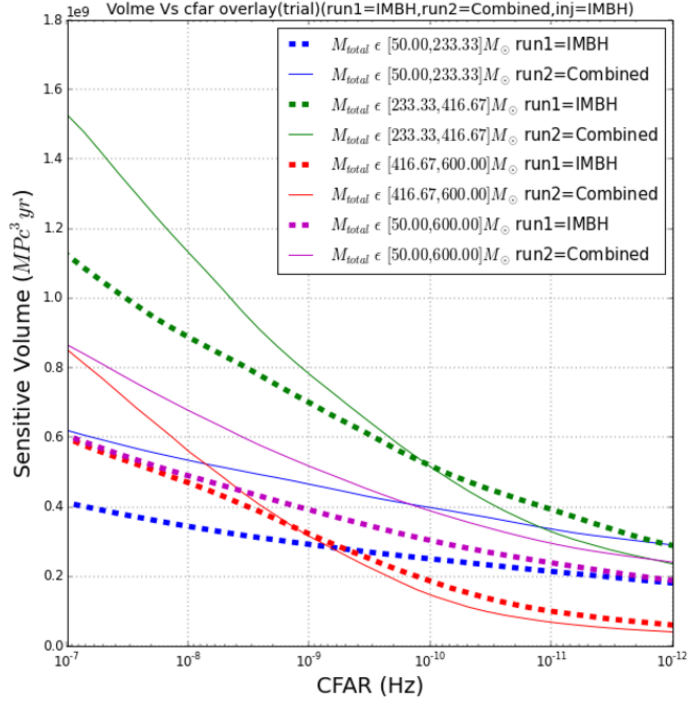


Figure 21 : Overlay of volume sensitivity vs CFAR for IMBH search and combined search using full IMBH injections, with a trials factor. The plot for the IMBH search shifts to the left, a region of higher CFAR, hence lower significance, to account for the fact that the IMBH search only covers a part of the parameter space being covered by the combined search.

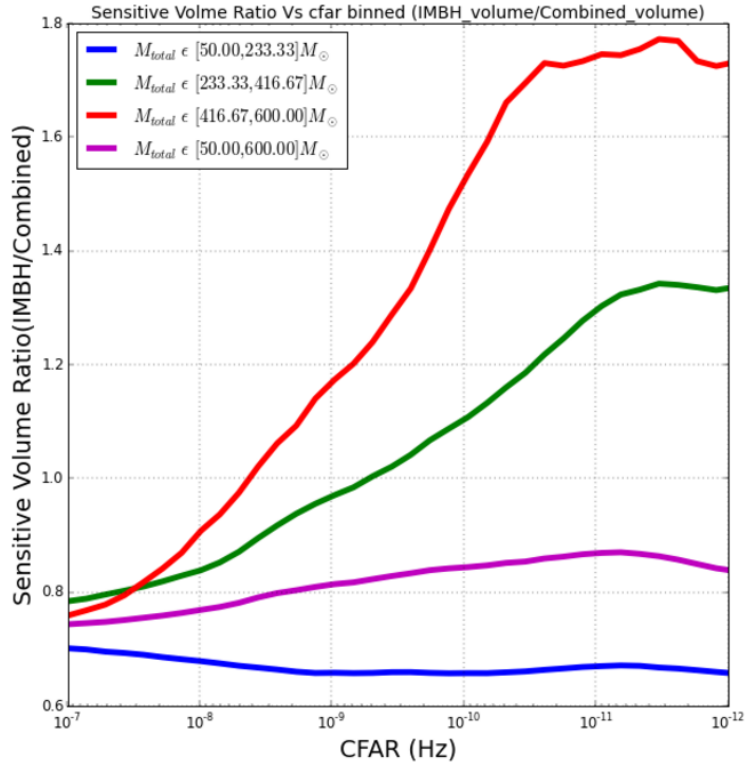


Figure 22 : Relative volume sensitivity vs CFAR for IMBH search and the combined search using full IMBH injections, without a trials factor.

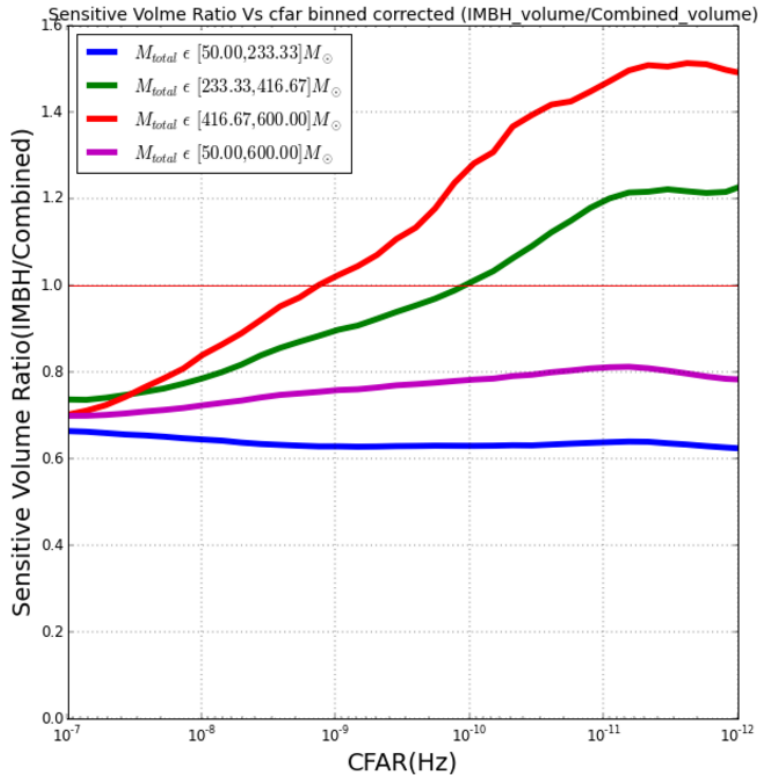


Figure 23 : Relative volume sensitivity vs CFAR for IMBH search and combined search using full IMBH injections, with a trials factor. Inclusion of the trials factor gives us the physical results.

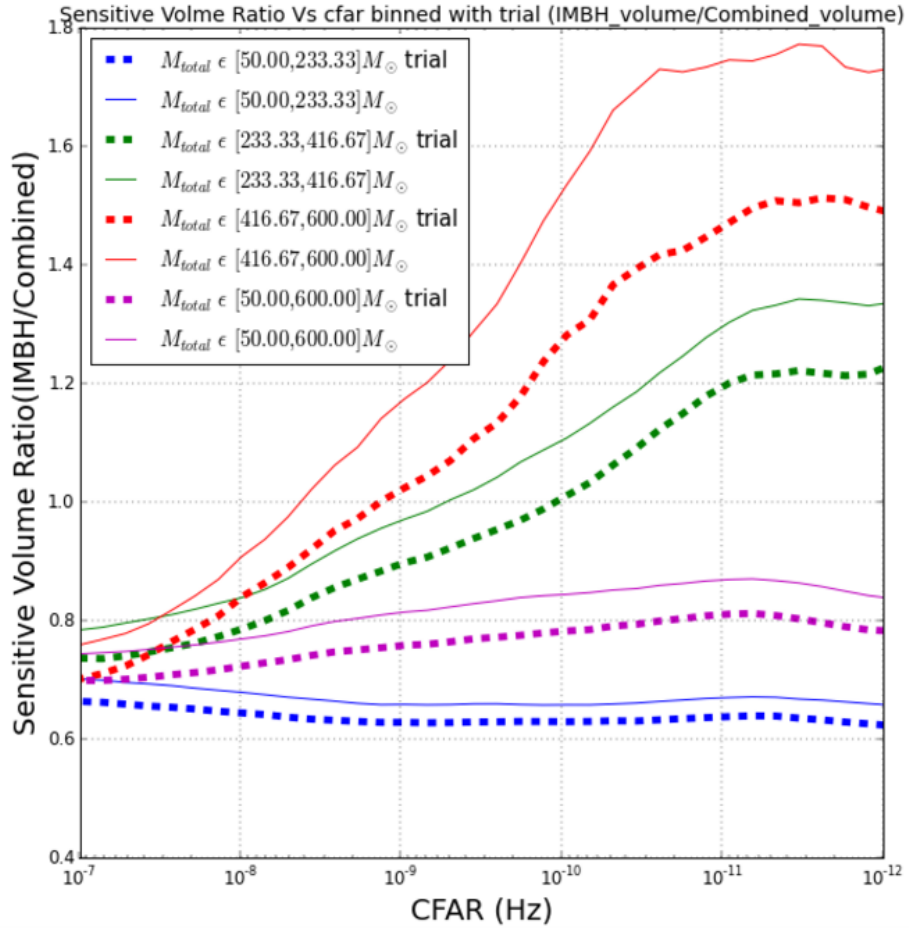


Figure 24 : Relative volume sensitivity vs CFAR for IMBH search and combined search using full IMBH injections, with and without a trials factor for comparison. Inclusion of the trials factor gives us the physical results.

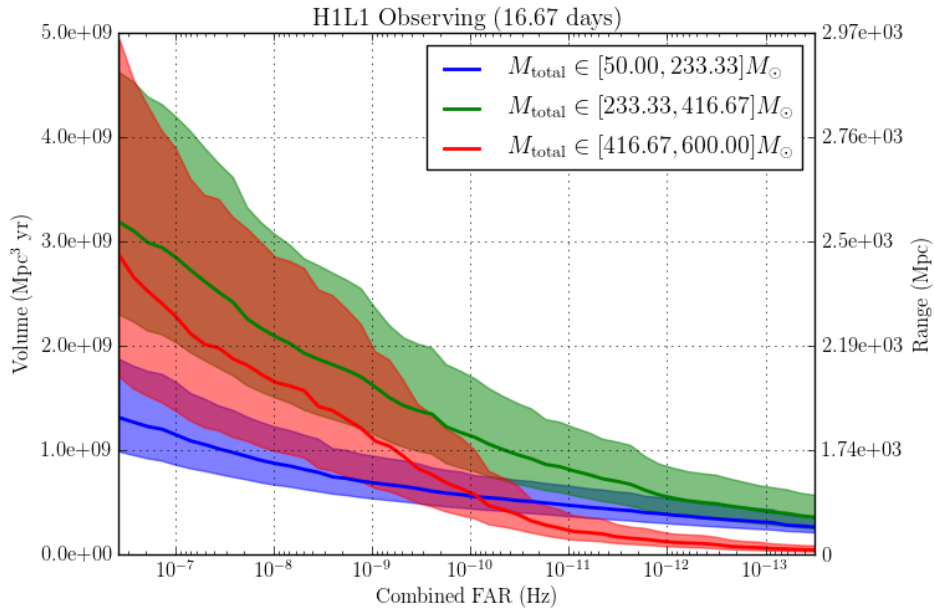


Figure 25 : Volume sensitivity vs CFAR for IMBH run using IMBH pruned injections (gstlal pipeline)

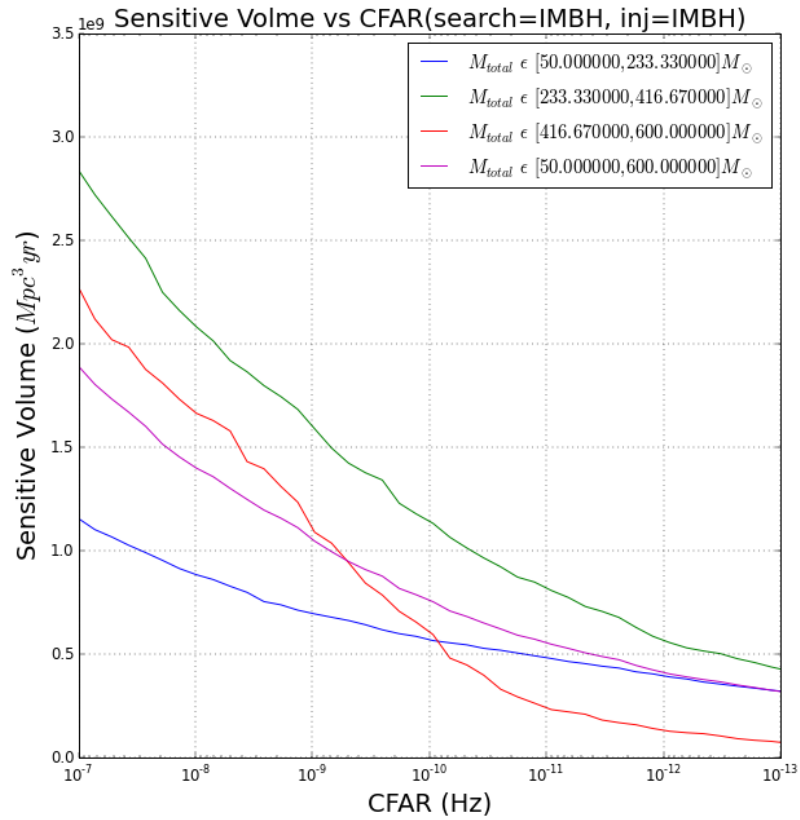


Figure 26 : Volume sensitivity vs CFAR for IMBH run using IMBH pruned injections (efficiency method, using appropriate segments and live time. This is in agreement with the plot obtained by the GstLAL-based inspiral pipeline in Fig. 25 as expected.)

Chapter 3

Does a Supernova Mass Gap Really Exist? using source-dependent template-weighting and FGMC formalism to investigate the SN mass gap

3.1 Background

3.1.1 Astrophysical motivation for inspecting the mass gap

It is well understood that the distribution of the masses of progenitor stars is uniform in the range $0.1-100 M_{\odot}$, but the distribution of their compact remnants are not seen to follow the same pattern. As first observed by Bailyn et al [10] there seems to be no observed compact remnants in the range $2-5 M_{\odot}$, which has later been called a “mass gap” [11]. Inspecting and understanding this gap is crucial to understanding neutron star equations of state and the supernova mechanism or engine for formation of compact objects [12].

In the paper by Beczynski et al 2012 [12], possible mechanisms for the formation of such a mass gap is explored. As shown in Fig. 27, different models of supernova mechanism

and the results of a population synthesis code are compared against observations for the galactic population of Roche lobe overflow and wind fed X-ray binaries. The “rapid” model, refers to a mechanism where during the initial core collapse of a supernova, a proto-neutron star is formed and the infalling material bounces off the surface of it. This creates an outgoing shock which runs into the infalling matter causing the shock to be stalled. Neutrinos are absorbed, heating the region between the stalled shock and the proto-neutron star thereby creating a turbulent atmosphere. Growing instabilities in this region can cause violent displacement of the layers, causing an explosion in the first 200 to 300 ms or at a rapid time scale. This creates no remnant as the entire star explodes, thus causing a mass gap, which is in agreement with observations. The creation of other types of instabilities above the stalled shock, can cause a delayed growth of instability and explosion as described by the “delayed” model. These instabilities cause the star to explode, if at all in about a 1000 ms after the first collapse. This allows the star enough time to cool and any explosion the star undergoes is likely to be weak, causing remnants to be formed. In this case no mass gap is observed, which agrees with the population synthesis code, which predicts a more continuous distribution of remnants. Hence depending on which mechanism is undertaken by the supernova explosion, a mass gap is either observed or not observed. This makes looking for a mass gap important.

Also, as Baczynski et al 2012 [12] points out, such observational “evidence” could be biased as they could depend on transient behaviour of the components or biased inclination and hence mass measurements due to inaccuracies in light curve analyses [13]. Hence investigation of the possibility of the presence of a mass gap using gravitational wave rate estimates seems to be in order.

Littenberg et al 2015 [14] used LALInference software library [15] to recover the mass parameters of compact systems around the proposed mass gap of 3-5 M_{\odot} . From Fig. 28 from their paper, we see that the error bars for the mass gap objects straddle the gap, causing the gap to be difficult to distinguish. In their paper they also found that depending on the underlying distribution of masses, it takes about 10s to 100s of detections to confirm the mass gap.

We attempt to check some of these conclusions using rate estimations and data analysis

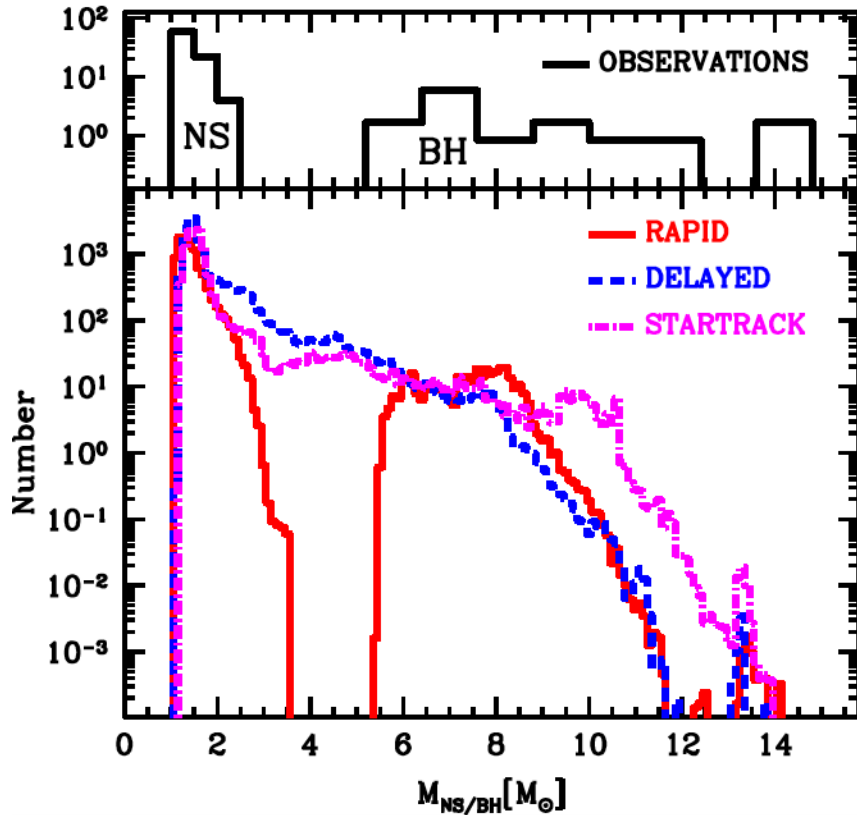


Figure 27 : [12] Predicted galactic neutron star/black hole mass distribution. From Rapid ($< \sim 100 - 200 \text{ ms}$) and Delayed ($> \sim 500 - 1000 \text{ ms}$) models of supernova explosion and from Star Track population synthesis code. From the Rapid model, almost no compact objects with mass $2-5 M_{\odot}$ is noted, as found in the observations of X-ray binaries, shown in the top panel. The Delayed model predicts a more continuous distribution of remnants as does the population synthesis code.

using O2 data. We look for posterior support for mass gap objects in the data.

3.2 Methods and techniques used

In order to investigate the possibility of presence of a mass gap, we need to be able to obtain count posteriors for events within the mass gap. Hence we use the counting formalism developed by Farr, Gair, Mandel, Cutler, hereafter known as FGMC [16]. This is used in conjunction with source dependent template weighting based on the idea of down-ranking triggers from other populations when trying to find posteriors for a specific population [17] [18].

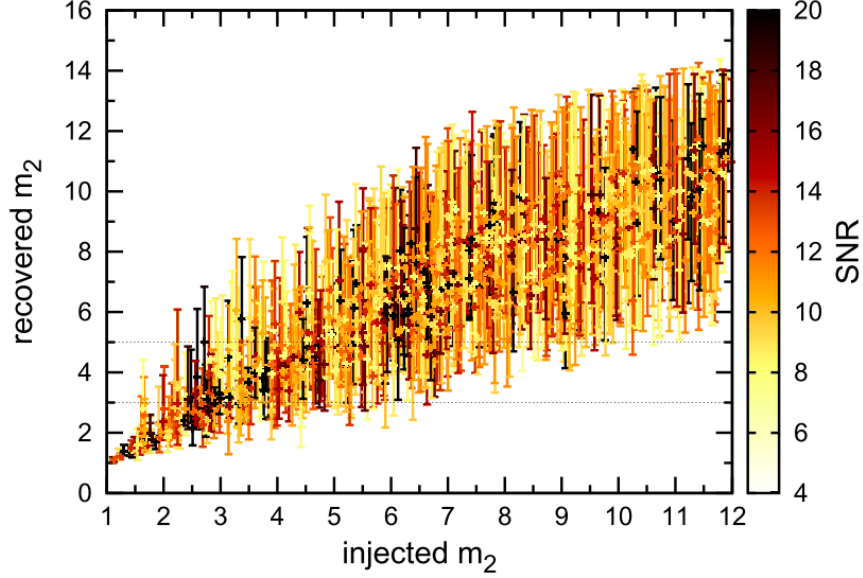


Figure 28 : [14]90 % credible intervals for recovered m_2 as a function of the true mass. Each entry is colored by the network SNR of the source. Horizontal lines denote the mass gap [11]. We see that the error bars for the mass gap objects straddle the gap, causing the gap to be difficult to distinguish

3.2.1 Two component Rates computation for CBC ¹

For a given set of event data $\{x_1, x_2, \dots, x_M\}$, and probability distributions $p_0(x)$ and $p_1(x)$ for background (noise) and foreground (signal) models, with a prior distribution, $p(\Lambda_0, \Lambda_1)$, the posterior distribution is:

$$p(\Lambda_0, \Lambda_1 | \{x_1, x_2, \dots, x_M\}) \propto p(\Lambda_0, \Lambda_1) \exp(-\Lambda_0 - \Lambda_1) \prod_{i=1}^M [\Lambda_0 p_0(x_i) + \Lambda_1 p_1(x_i)]. \quad (3.2.1)$$

where, the count of background events is Λ_0 , and foreground events is Λ_1 . For our considerations, x_i would represent the data points including parameters of the systems, for instance mass.

3.2.2 Multi component Rates computation using FGMC formalism ²

Equation 3.2.1 can be extended to multiple components as shown in [20]:

$$p(\Lambda_0, \Lambda_\alpha | x_\alpha) \propto \prod_{j=1}^N [\Lambda_0 W_0(m_j) + \sum_\alpha \frac{f(x_j | m_j)}{b(x_j | m_j)} \Lambda_\alpha W_\alpha(m_j)] e^{-\Lambda_0 - \sum_\alpha \Lambda_\alpha} \quad (3.2.2)$$

¹This section has been written referring to notes by Jolien Creighton which lie in LIGO document control (dcc) repositories [19].

²This section has been written referring to notes by Shavath Kapadia which lie in LIGO document control (dcc) repositories [20].

where, the weights are computed as:

$$W_\alpha(m_j) = \frac{A_\alpha(m_j)}{\sum_{no.ofSVDbins} A_\alpha(m_j)} \quad (3.2.3)$$

α goes over multiple population categories

j goes over zero lag (coincident) triggers

A_α = activation counts. m_j are template parameters like mass.

Λ_0 = constant = number of zero lag triggers

W_0 = 1/number of SVD bins, f = foreground, b = background

We assume a uniform prior on counts. We only use triggers that are well found, i.e, ones that are found with a false alarm rate $CFAR > 1/30$ days. Eq. 3.2.2 pins the probability distribution of the background to a constant W_0 which assumes any of the bins can be activated by noise. On the other hand the total foreground probability distribution is given by the ratio of the earlier foreground distribution for the 2 component case and the distribution of background noise, which is now weighted by Eq. 3.2.3, which is the probability that a particular trigger, recovered by a certain SVD bin which is explained in chapter 4 belongs to a certain astrophysical category, as represented by α . The activation counts are the number of times a specific group of templates or bin, recovers simulated signals, in other words, gets activated. The activation count and hence Eq. 3.2.3 is computed by using simulated signals of the different astrophysical categories as injections into the pipeline so it can recover them. Then the distribution of such recovery across the space of the SVD template bins is used to compute the weights.

3.3 Steps undertaken to obtain a posterior for mass gap populations

In order to obtain $p(\Lambda_0, \Lambda_\alpha | x_\alpha)$ in equation 3.2.2, we need to compute the the weights as shown in equation 3.2.3 and hence A_α the activation counts. As discussed in chapter 4, for efficient matched filtering, the templates are grouped or binned by parameters like \mathcal{M} and χ after which they undergo a single-valued decomposition (SVD) which returns only the most representative basis waveforms called SVD banks or bins. These bins can thought of as being “activated” when a certain trigger is recovered by a certain bin. The

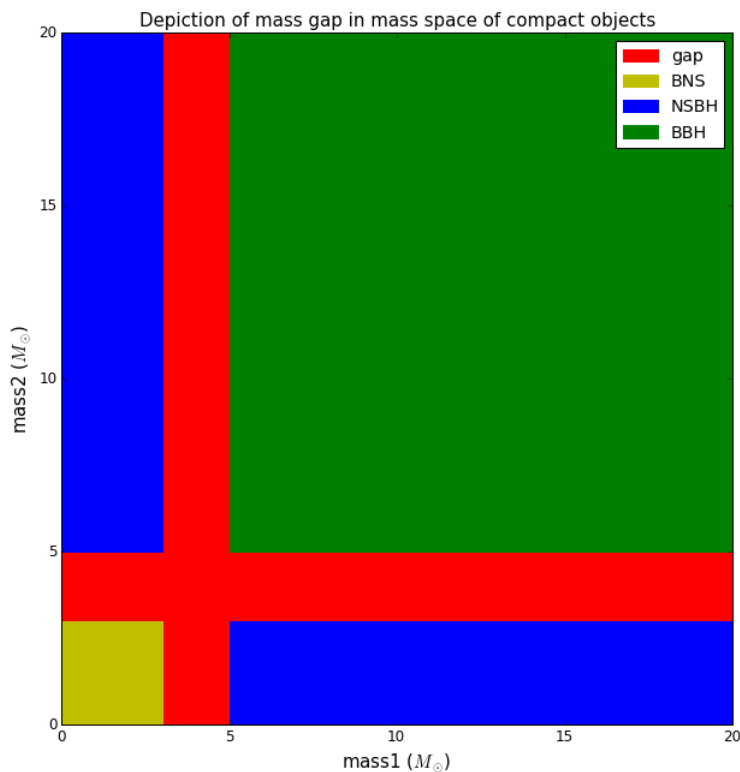


Figure 29 : Representation of the categories of different populations of compact binaries in their component mass space. Sets of simulated injections are used corresponding to each category to obtain the weights.

number of times each SVD bin recovers triggers or simulations gives its activation count. A normalized value of this activation count forms the weight corresponding to each SVD bin. Hence we select injections suitable to our study as described below and obtain the weights based on the distribution of the recovery of these simulations across the template bins. This is then used to compute the posterior.

3.3.1 Injections and data used

We use data corresponding to O2 chunk 21 (GPS times: 1186624818-1187733618, i.e 13th -25th August 2017) including GW170814 a BBH event [21] and GW170817 a BNS event [22] and added to this is GW170608 a low mass BBH event [23].

The injections chosen for each type of population is as shown in figure 29 and in table 6.

Population	$m_1(M_\odot)$	$m_2(M_\odot)$	$m_1 + m_2(M_\odot)$
BNS	$m_1 \in [1, 3]$	$m_2 \in [1, 3]$	
NSBH	$m_1 \in [5, 100]$	$m_2 \in [1, 3]$	$m_1 + m_2 < 100$
NSBH	$m_1 \in [1, 3]$	$m_2 \in [5, 100]$	$m_1 + m_2 < 100$
BBH	$m_1 \in [5, 100]$	$m_2 \in [5, 100]$	$m_1 + m_2 < 100$
gap	$m_1 \in [3, 5] \ m_1 > 1$	$m_2 \in [3, 5] \ m_2 > 1$	$m_1 + m_2 < 100$

Table 6 : Description of different categories of astrophysical populations in terms of the component masses of the systems. The simulations used to obtain posteriors for each category, satisfy these requirements.

3.3.2 Distribution of recovery of injections across groups of template banks

Fig. 30 shows the distribution of the recovered template bank parameters across the \mathcal{M} - χ or SVD bins. It is noticeable that the different types of signals, especially the NSBH and BBH types, often activate overlapping bins.

3.3.3 Obtaining count posteriors for 5 categories of populations and comparison with the earlier 4 categories ³

We obtain the counts posteriors using the weights described in the previous section. We use the FGMC module. We use a 4-component FGMC formalism at first, the 4 components or in our case, categories of compact object populations being binary neutron stars (BNS), neutron star black hole binaries (NSBH), binary black holes (BBH), and a population of terrestrial noise.

Fig. 31 shows the posterior distributions considering categories BNS, NSBH and BBH. The plot for NSBH shows a mode of 0 consistent with no observations of NSBH, while the plot for BBH shows a mode ~ 2 consistent with the two BBH events in our data. The plot for BNS injections shows a mode of ~ 2 even though the data has a single BNS event. This is because addition of a high significance event or trigger, increases the probability of the other events in the set to be of astrophysical origin and may cause them to have a mode greater than 1. The BNS event is the most significant event detected so far. Hence the 4-component FGMC module generates count posteriors mostly consistent with our expectations.

³This section used the FGMC module developed by Shavath Kapadia and Jolien Creighton, which is under review and testing, and has been documented by Shasvath Kapadia which lie in LIGO document control (dcc) repositories [20].

We then extend this study to include a 5th component of a mass gap category as described in table 6.

Fig. 32 shows the posterior distributions considering categories BNS, NSBH BBH and mass gap. The posterior distribution for NSBH is still 0 as expected, that for BBH is still close to ~ 2 and that BNS is greater than 1 and is ~ 2 just as in the 4-component case and is expected.

The significant result is we see a mode of 0 for the mass gap population, which is consistent with our expectation as no mass gap events were observed.

3.4 Effect of adding an event at the center of the gap

We now investigate if it is at all possible to detect an event in the mass gap by observing a shift in the mode for the corresponding posterior distribution of the mass gap. In order to do this, we introduce simulated events in the mass gap. We choose a low significance simulated event with a signal to noise ratio $\text{SNR}=8.5$, which corresponds to an equal mass system with component masses $3.9 M_{\odot}$. The posterior obtained is shown in the left plot of Fig. 33, which shows no detection.

Next we choose a high significance event with an $\text{SNR}=15.2$, corresponding to a system with component masses $3.9M_{\odot}$ and $2.9M_{\odot}$. The posterior obtained is shown in the right plot of Fig. 33 which shows a shift in the mode and hence a detection.

3.5 Number of events needed for a detection in the mass gaps for different mass distributions

Since a significant event in the mass gap can be detected, it is natural to ask, how many events do we need in the mass gap to be able to make a detection given varying underlying mass distributions. The number of events needed for a detection are likely to depend on an underlying mass distribution as for heavier masses, the error bars on the estimated component mass increases, as can be appreciated from Fig. 28. We inject simulated events in two regions, a low mass region within the gap between $3-4 M_{\odot}$ and the higher mass

region $4-5M_{\odot}$ in component masses and find the number needed to see a shift in the mode of the posterior. The plots obtained are shown in Fig. 34. We need about 5 events if the mass distribution on compact objects in the gap are biased towards lower masses while we need about 6 of these if the bias is towards higher masses. This is consistent with the fact that with increase in component masses, the error bar on the estimation of the component masses increases, thus requiring more detections to falsify the gap.

3.6 Effect of events at the edge of the gap

Fig. 35 shows that if the events lie close to the edges of the gap, they can cause the mass gap posterior to peak away from zero and thus look like a mass gap event. 7 events were added closer to $3 M_{\odot}$, with 1 outside the gap and 3 events were added closer to $5 M_{\odot}$. Both cases return a mode close to 5, showing that there isn't clear distinguishability as to whether the event lies within the mass gap, if it is very close to the edges. The formalism is limited in this respect.

3.7 Results, conclusions and looking forward

The conclusions we have drawn are:

1. No mass gap events were contained in the data set considered.
2. In case of a presence of a significant event at the centre of the mass gap, it will cause the mass gap posterior to peak away from 0, thereby showing a detection.
3. The number of events needed to falsify a mass gap, depends on the underlying mass distribution. Heuristically, if the distribution is biased towards lower mass objects, we need 5 events in the mass gap to see a non zero mode in the posterior. If the bias is towards higher masses, we expect to see a shift in the mode for at least 7 events in the gap.
4. The method has limited ability to distinguish between mass gap events and non mass gap events, if they lie very close to the edges of the gap.

5. The method assumes a hypothetical gap going from 3 to 5 M_{\odot} and proceeds to look for posterior support for events within. A more robust study would require keeping the edges of the gap floating or obtain a distribution of mode of counts posteriors with respect to component masses.

The mass gap category of compact objects are worth while looking into and an investigation into the possible presence of a gap has astrophysical significances. Hence a rates posterior statement about this category has been planned when cataloguing events and discoveries made at the end of O2.

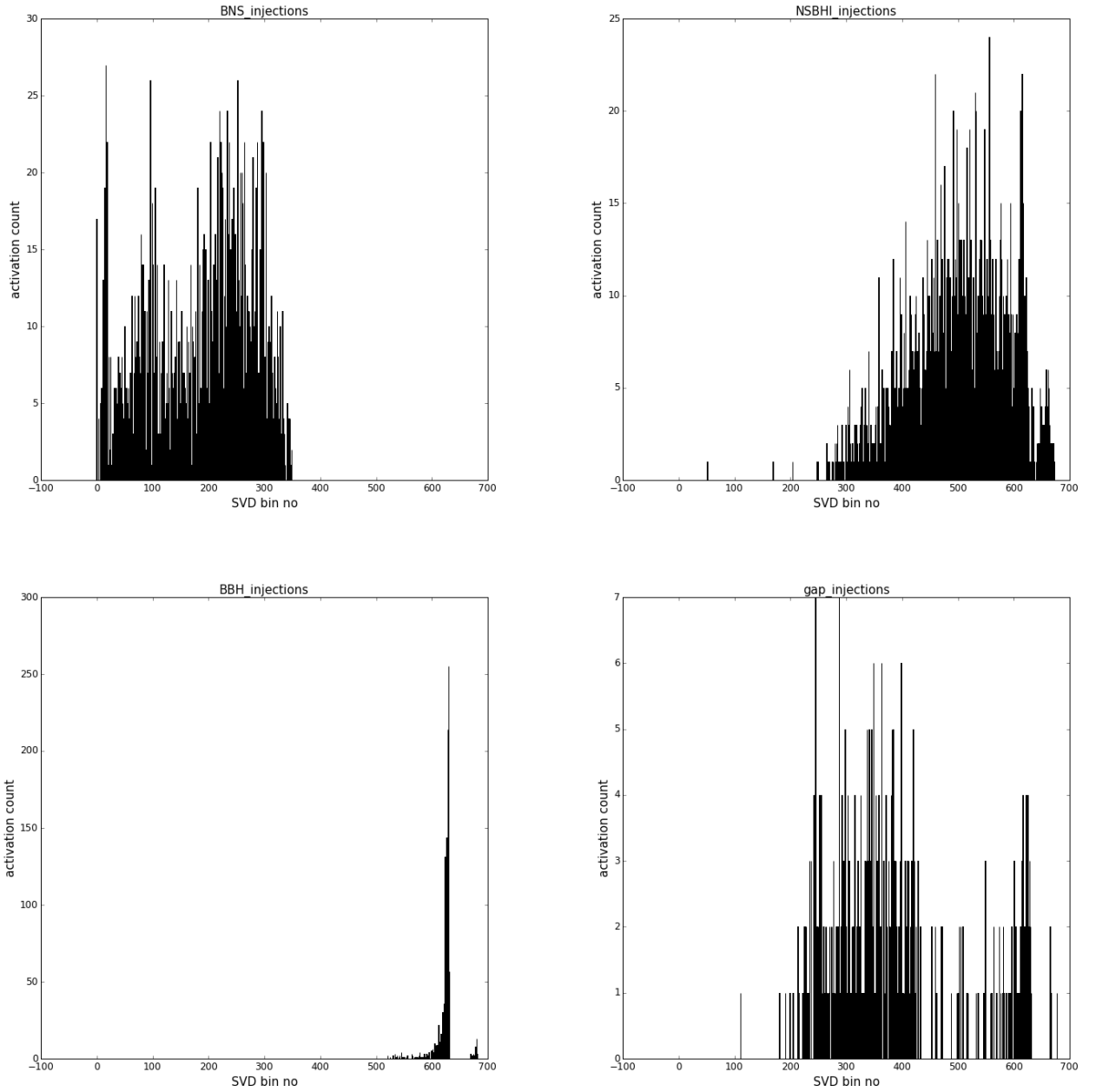


Figure 30 : Number of times each template bin is activated by a simulation, in other words number of simulations recovered by a specific bin, plotted against the bin number. NSBHI refers to the population of NSBHs that have $m_1 \in [1, 3]$ & $m_2 \in [5, 100]$, i.e the population to the left in Fig. 29

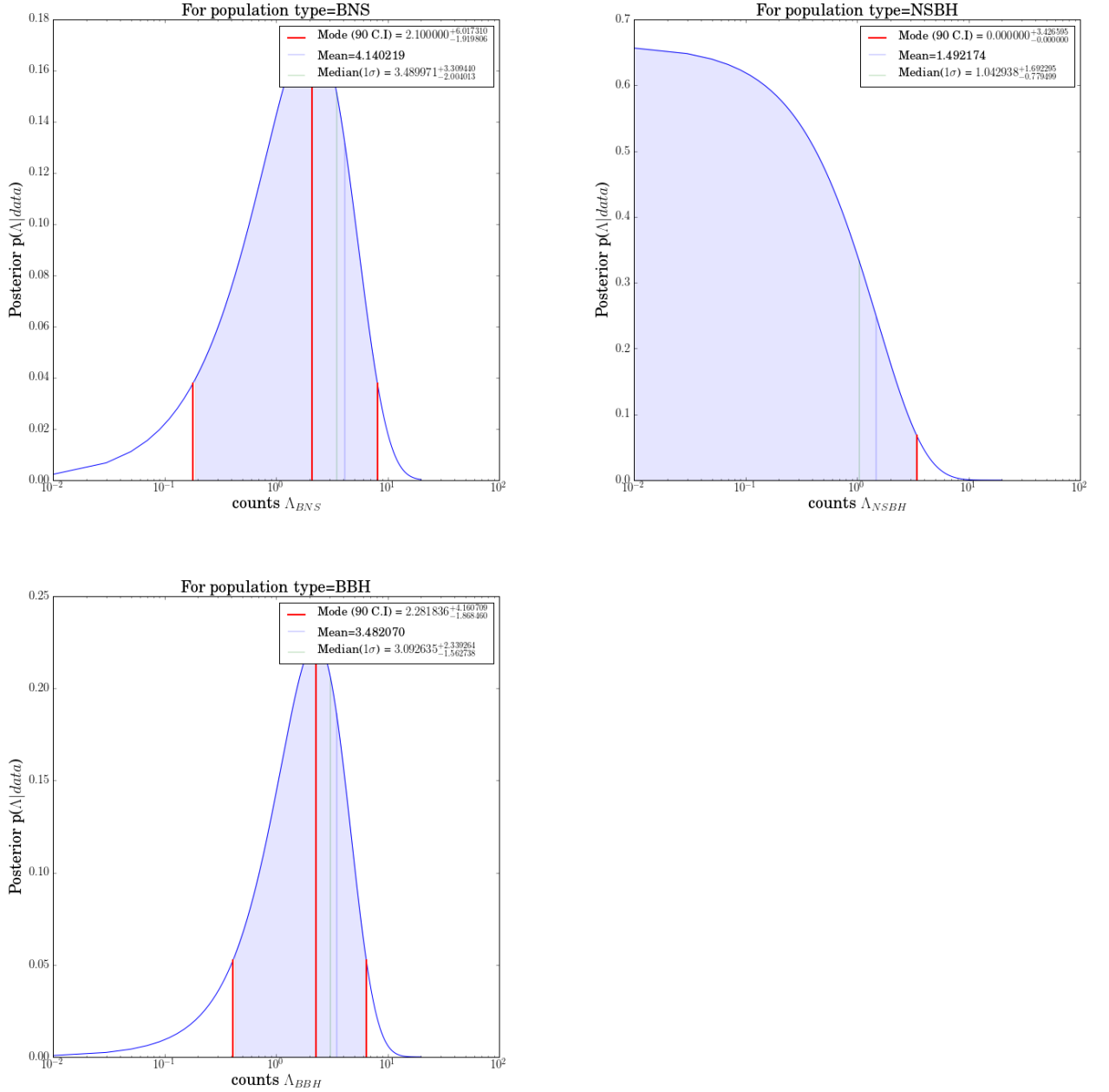


Figure 31 : The count posteriors are plotted against the number of counts for BNS, NSBH and BBH populations. The plot for NSBH shows a mode of 0 consistent with no observations of NSBH, while the plot for BBH shows a mode ~ 2 consistent with the two BBH events in our data. The plot for BNS injections shows a mode of ~ 2 even though the data has a single BNS event. This is because addition of a high significance event or trigger, increases the probability of the other events in the set to be of astrophysical origin and may cause them to have a mode greater than 1. Hence the 4-component FGMC module generates count posteriors mostly consistent with our expectations.

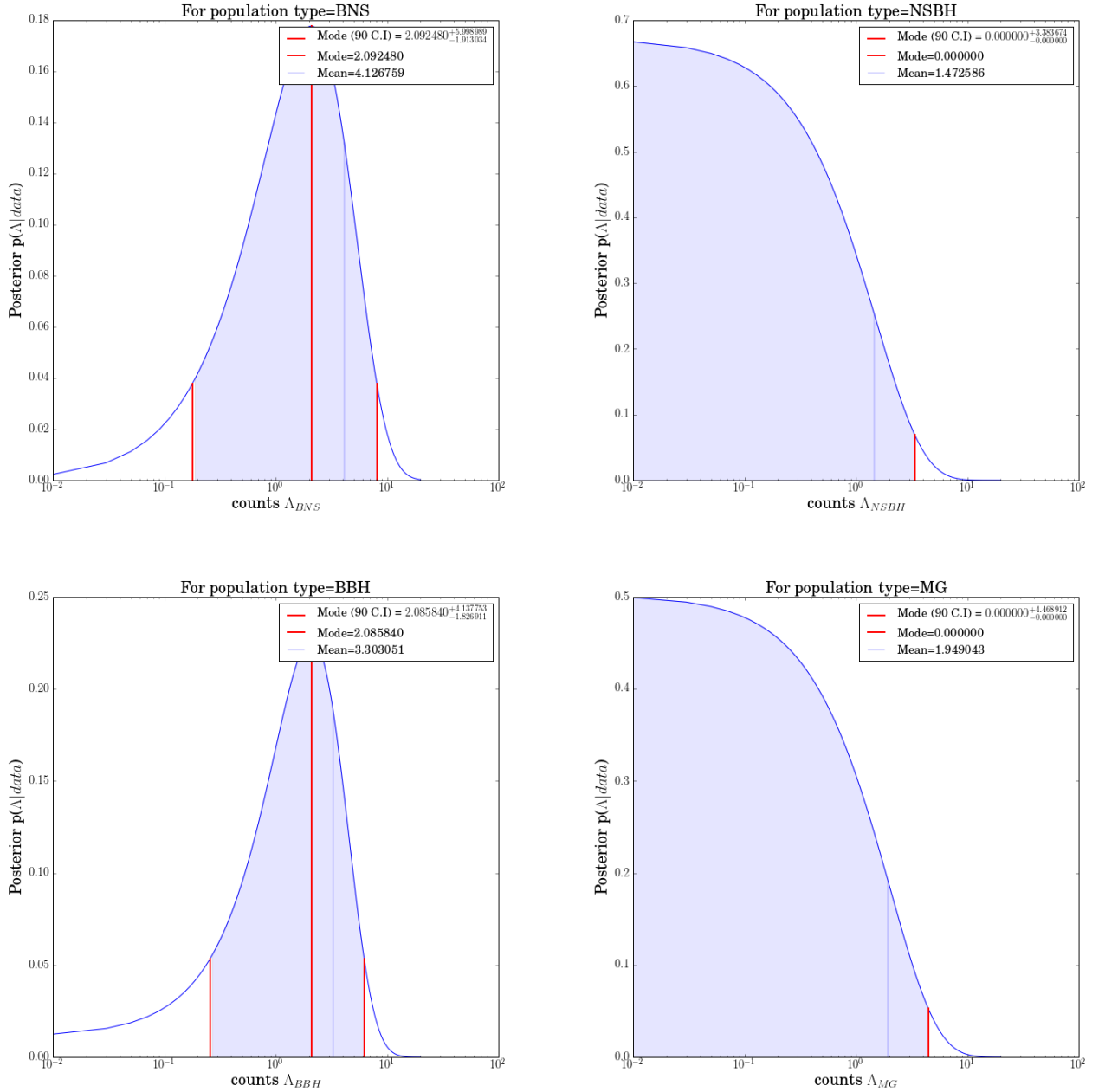


Figure 32 : The count posteriors are plotted against the number of counts for BNS, NSBH, BBH and mass gap categories of populations. The posterior distribution for NSBH is still 0 as expected, that for BBH is still close to ~ 2 but that for BNS is greater than 1 and is ~ 2 , just as in the 4-component case and is expected. The significant result is we see a mode of 0 for the mass gap population, which is consistent with our expectation as no mass gap events were observed.

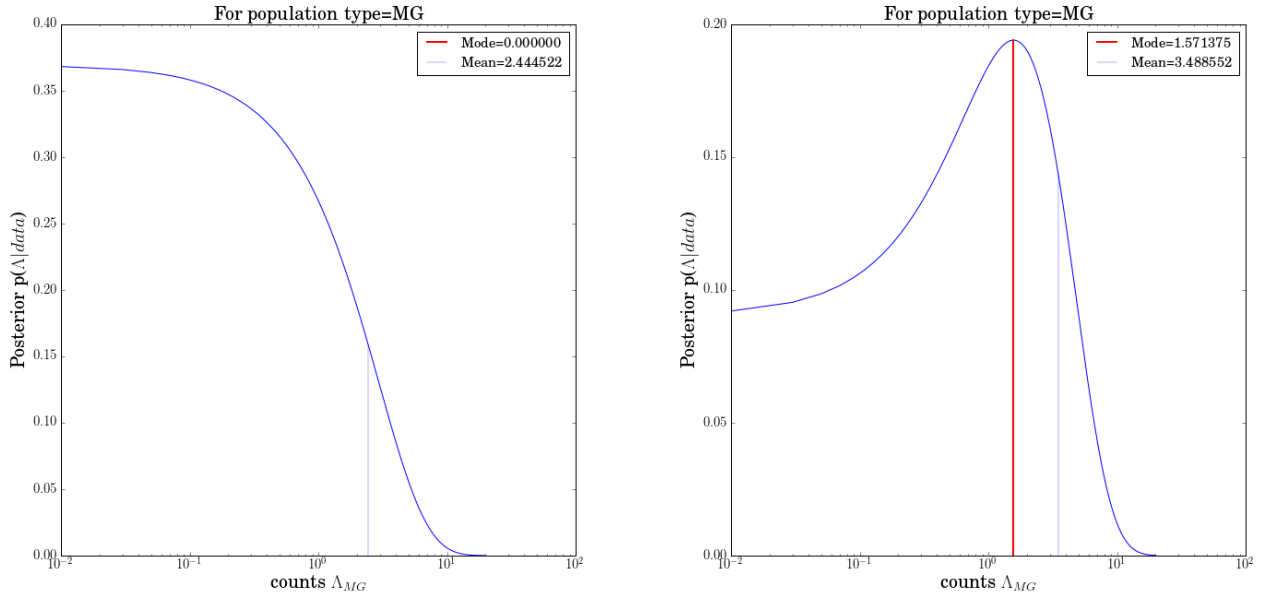


Figure 33 : The count posteriors for the mass gap are plotted after introducing a low significance (SNR=8.5) (left plot) and a high significance (SNR=15.2) (right plot) simulated event in the mass gap. The left plot shows no detection for the low significant event, but the right plot, i.e. the case of the high significance event, shows a detection.

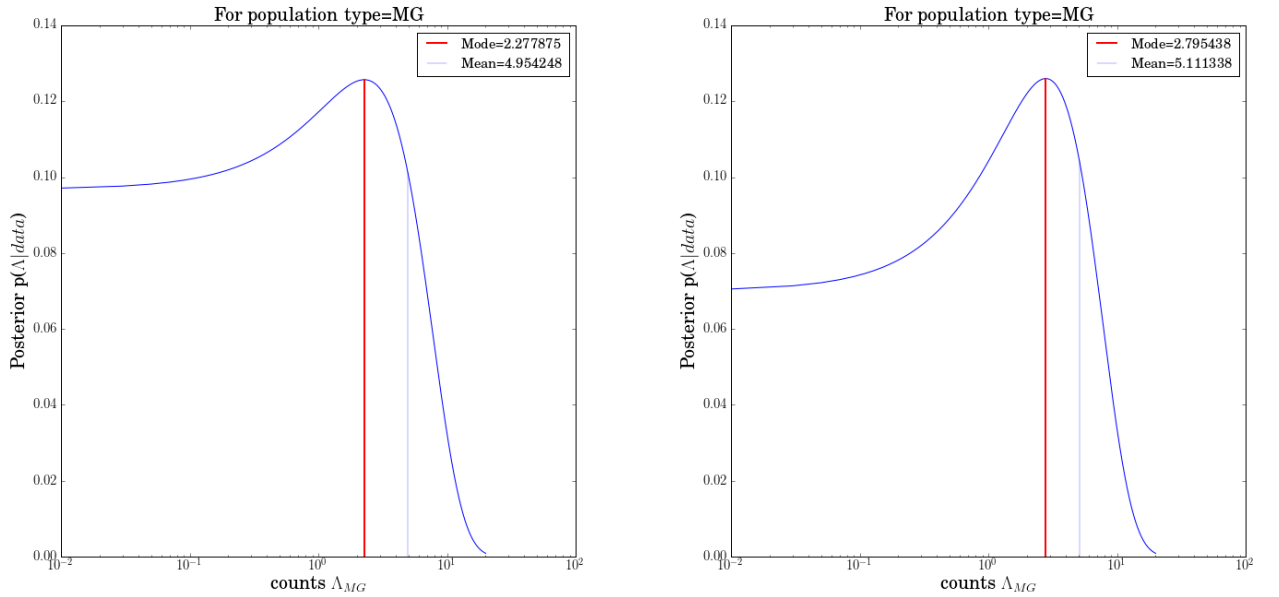


Figure 34 : The count posteriors for the mass gap are plotted after introducing significant events ($50 < \ln L < 60$) (left plot) 5 were needed for detections in range 3-4 M_{\odot} . (right plot) 6 were needed for detections in range 4-5 M_{\odot} .

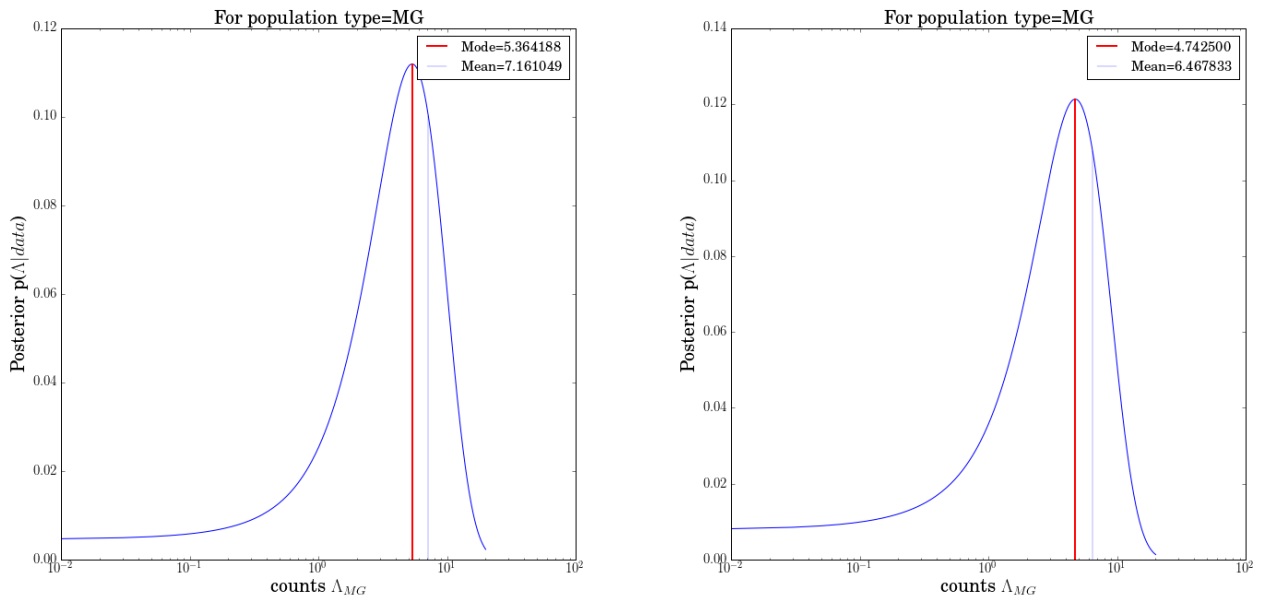


Figure 35 : The count posteriors for the mass gap are plotted after introducing significant events ($50 < \ln L < 60$) (left plot) 7 events were added closer to $3 M_{\odot}$, with 1 outside the gap. (right plot) 3 events were added closer to $5 M_{\odot}$. Both cases return a mode close to 5, showing that there isn't clear distinguishability as to whether the event lies within the mass gap, if it is very close to the edges.

Chapter 4

Contributions to the template bank used by the offline Gstlal pipeline for the 2nd observing run ¹

4.1 Introduction

We describe the template bank used by the template based search pipeline or the GstLAL-based inspiral pipeline to analyze data from the second observation run of the advanced LIGO. The bank includes templates covering a total mass range of 2-400 in solar masses (M_{\odot}). It combines searches for various coalescing compact binary systems, including neutron star-neutron star systems, neutron star-black hole binaries and black hole-black hole binaries. The component masses of the neutron star binaries are less than $2M_{\odot}$ with spin aligned, with the effective spin parameter in range $(-0.05, 0.05)$. The black hole binaries have component masses greater than $2M_{\odot}$ with aligned spin, the effective spin parameter in range $(-0.999, 0.999)$. Such a combined search, targeting a wide range of astrophysical objects, was not done for the first observing run. Below a total mass of $4M_{\odot}$ the waveforms are approximated using TaylorF2 waveforms [6], while above $4M_{\odot}$ an effective-one-body approximant (SEOBNR) [7] is used. The mass ratios lie in the range 1-97.989. We neglect the effect of precession and higher order modes in

¹Most of this chapter is under preparation for a publication

our templates, but they are capable of detecting higher order modes. The bank includes about 700,000 templates, including those, placed with a higher density in the higher mass region of the bank, in order to reduce the effect of coincident noise in time-shifted data. However, these extra templates limit the sensitivity of the bank in the higher mass end, which is an issue still under investigation.

4.2 Background

When Advanced LIGO is going through a phase of collecting data for scientific use, it is said to be going through an observing run. Advanced LIGO recently completed its second observing run on August 26, 2017. The first observing run of Advanced LIGO, otherwise known as O1, lasted between September 12, 2015 to January 19, 2016. In this period a total of two coalescence events were observed, The first being GW150914 on September 14, 2015 [3] and GW151226 on December 26, 2016 [24] both of which were binary black hole (BBH) mergers with over 5σ significance. The second observing run of Advanced LIGO, also called O2, began on November 30, 2016. On 4th January, 2017 a heavy binary black hole system was seen to merge with high significance, named GW170104 [25]. These and less significant candidate events led to computation of merger rates that showed a high probability of observation of more such events from black holes with companion masses $>\sim 25 M_{\odot}$ in the near future [26], [27].

The GstLAL-based inspiral pipeline used for the search [9], is derived from GStreamer [28] and the LIGO Algorithm Library [29] and based on the GstLAL library [30]. The GstLAL-based inspiral pipeline can function both in the online and offline configuration. In the online or low-latency mode, it can check for gravitational waves in the data, provide point estimates of parameters and assign a significance to a candidate event or trigger. The offline mode of operation uses archived data and has the advantage of improved data quality and background estimation.

Search pipelines correlate detector data with template waveforms, predicted by general relativity using a technique called matched filtering. These templates contain information

about the coalescence and various parameters of the binary, like companion masses, spins and waveforms. They together span over a multi-dimensional parameter space, forming a *template bank*. A detection coincidence in both detectors consistent with 10 ms inter-site propagation time, indicates a possible signal. This method can be used for both online and offline searches. There are other pipelines that use the matched filtering method, but we will focus on describing the template bank used by the GstLAL-based inspiral pipeline.

4.3 Design and construction of the O2 bank

4.3.1 Astrophysical sources targeted:

The compact objects targeted by the O2 GstLAL-based inspiral pipeline based search include binary neutron stars (BNS, total mass range 2-6 M_{\odot}), neutron star black hole binaries (NSBH, with total mass range 3-100 M_{\odot}), binary black holes (BBH, having a total mass range of 4-100 M_{\odot}) and intermediate mass binary black holes (IMBH, 100-400 M_{\odot}).

The two events detected in O1, GW150914 and GW151226 and the less significant candidate LVT 151012, were used to find the rates of mergers from such stellar mass binaries (spanning over binaries with a total mass range of 2-100 M_{\odot}), which turned out to be in the range 9-240 $Gpc^{-3}yr^{-1}$ [26]. Since no events were detected by the IMBH search (total mass range of 50-600 M_{\odot}), it was used to constrain the merger rates of IMBBHs, the tightest constraint being, less than 0.93 $Gpc^{-3}yr^{-1}$ [31]. The January event from O2, GW 170104 updated the rate of binary black hole mergers (searched over a total mass range of 2-400 M_{\odot}) to 12-213 $Gpc^{-3}yr^{-1}$ [25]. Such estimates have helped constrain the formation models or evolutionary methods of such binaries. However, the presently known formation channels do not seem to explain the full rate, but could contribute to the total if multiple formation channels are in use. Gaining precise knowledge about such formation channels, requires more detections. The increased knowledge of mass and spin distribution and its alignment to the orbital angular momentum from such detections, will help us understand the formation and evolution mechanism of these binaries better,

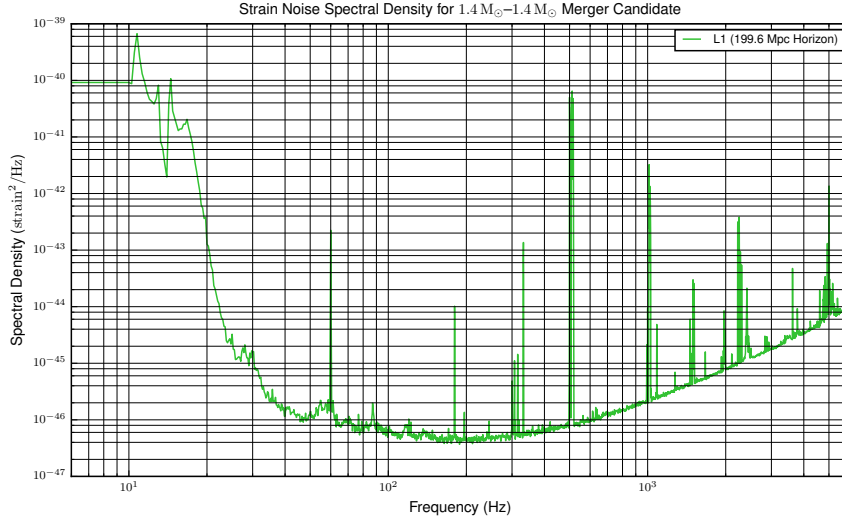


Figure 36 : A visual representation of the power spectral density used to model detector noise.

making such searches necessary.

4.3.2 Construction of the O2 bank

Modeling the detector noise

The noise power spectral density (PSD) is calculated by taking the harmonic mean of the power spectral densities from the individual detectors (Hanford and Livingston), measured over 9 hours of O2 data as shown in Fig. 36. Calculation of the PSD has been explained in [9] and in [32].

Parameter space covered and waveforms used

For O1, the GstLAL-based inspiral pipeline based search for compact binaries was divided into two separate searches. The stellar mass search was for binary neutron stars, black hole binaries and neutron star-black hole binaries. The Intermediate Mass Binary Black Hole (IMBBH) search looked for intermediate mass binary black holes. The two searches used separate template banks as they were looking for different objects. But they also overlapped.

Each of the templates represent systems that can be identified by the component masses m_i and the dimensionless spin parameters $\chi_i = \vec{S}_i \cdot \hat{L}/m_i^2$ for $i = 1, 2$, where \vec{S}_i are the spin vectors and \hat{L} is the orbital angular momentum unit vector. They are combined into

two quantities that characterize the templates, the chirp mass of the binary \mathcal{M} and an effective spin parameter χ_{eff} . They are defined as:

$$\chi_{\text{eff}} \equiv \frac{m_1\chi_1 + m_2\chi_2}{m_1 + m_2}, \quad (4.3.1)$$

$$\mathcal{M} = \frac{(m_1 m_2)^{3/5}}{(m_1 + m_2)^{1/5}}. \quad (4.3.2)$$

The template bank used for O1 stellar mass GstLAL-based inspiral pipeline based search, targeted binary systems with individual masses from 1 to 99 M_{\odot} and covered a total mass range of 2-100 M_{\odot} . For objects less than 2 M_{\odot} , the component object's spin was limited to $0.05 < \chi < 0.4$. For components heavier than 2 M_{\odot} , $0 < \chi < 0.9895$. Above a \mathcal{M} of 1.74, the waveforms of the binary systems were approximated by an effective-one-body formalism, combining results from the post-Newtonian approach, black hole perturbation theory and numerical relativity to model the complete inspiral, merger and ringdown waveform. The spins of the objects were also assumed to be aligned with the orbital angular momentum of the system. Below an \mathcal{M} of 1.74 the binary systems were approximated by an inspiral waveform accurate to third-and-a-half post-Newtonian order called the TaylorF2 waveform model [6] [33]. The lower cut-off frequency at which GstLAL-based inspiral pipeline began its analysis was 30Hz. There were a total of about 250,000 templates. The IMBBH region was searched by a bank with about 45000 templates covering a total mass range of 50-600 M_{\odot} . The templates used reduced-order model of a double aligned-spin effective-one-body waveform [34]. The spin parameters spanned over $(-0.99, 0.99)$ where negative and positive values denoted spin anti-aligned and aligned with the angular momentum of the system. The lower cut-off frequency in this case was 15 Hz, due to the noise characteristics at the lower frequency end [31].

For O2 a combined bank was used which searches over the aforementioned stellar mass region, as well as part of the previous IMBBH search region, covering a total mass range of 2-400 M_{\odot} . The filtering frequency was also reduced to 15 Hz, from 30 Hz which is what it was in the O1 stellar mass search. Component masses in neutron star binaries being less than 2 M_{\odot} with spin aligned in range $(-0.05, 0.05)$. Black hole binaries have component masses greater than 2 M_{\odot} with aligned spin in range $(-0.999, 0.999)$. Individual masses of

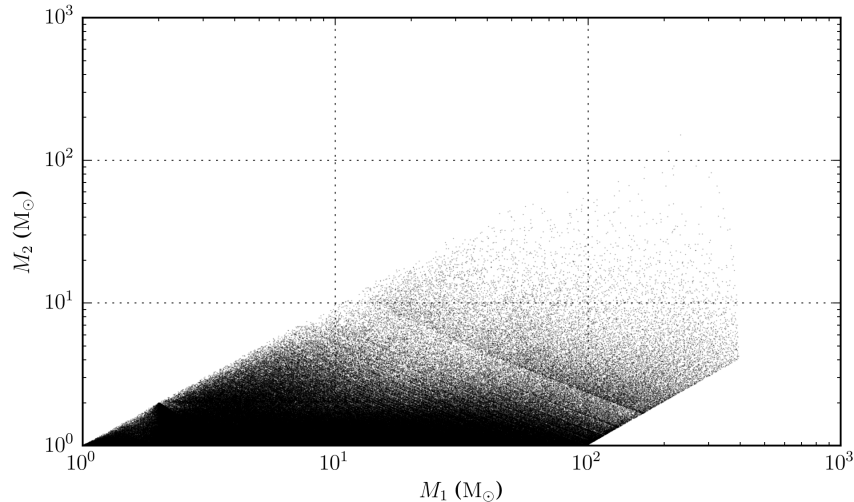


Figure 37 : A visual representation of the original O2 search bank in the component mass space .

systems, lie in the range 1-399 M_{\odot} with mass ratios in the range 1-97.989. As in the case of the O1 stellar mass bank, above an \mathcal{M} of 1.74, the waveforms of the binary systems were approximated by an effective-one-body formalism, below an \mathcal{M} of 1.74, the binary systems were approximated by a TaylorF2 waveform model [6]. We neglect the effect of precession and higher order modes in our templates.

Initial placement of templates

The template bank is created in two stages, creating two sub banks. For templates with total mass less than 4 M_{\odot} , the TaylorF2 approximation is used and templates are laid down using the geometric technique, using a metric [35]. For the other sub bank, covering templates with total mass greater than 4 M_{\odot} , the effective-one-body approximant, is used with templates placed stochastically, which is a method of placing templates randomly and then removing those that are “too close” [36]. A minimum match of 97% between the templates was set. The two sub banks were added to form the full bank with a total of 661335 templates.

The initial bank generated this way, as shown in Fig. 37 was used to find the 1st event detected during O2, GW170104 [25]. The higher density of the bank at lower masses is an expected feature, since low mass systems that spend longer in the LIGO frequency band, have longer waveforms, leading to higher ability to distinguish between

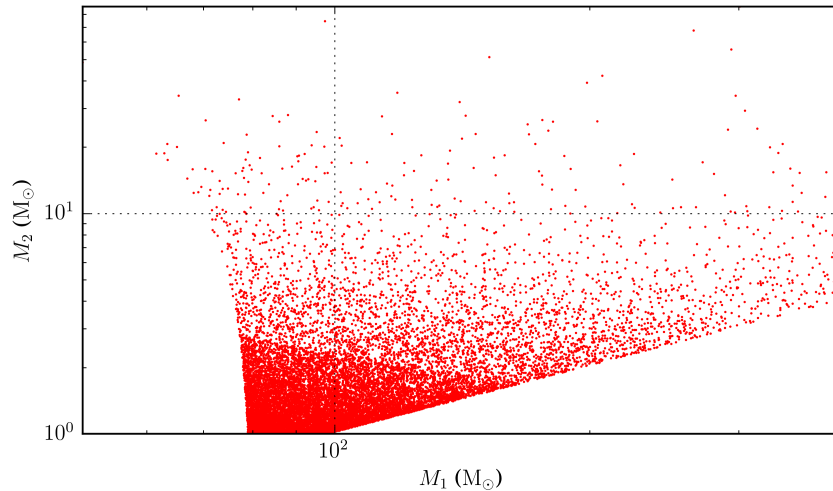


Figure 38 : The extra 14667 templates that were added to the original O2 bank, with a higher minimum match above a total mass of $80 M_{\odot}$ in the component mass space.

two different systems. This ends up grouping templates with vastly different properties, together at the less dense, higher mass region of the bank, if the same number of templates are grouped together throughout, as was done in O1. This lead to suboptimal estimation of noise properties of these groups and hence incorrect estimation of the significance of coincident noise. Hence, two different recourses were taken. The bank was populated with extra templates in the higher mass region and templates in the higher mass region were grouped differently from those in the denser lower mass region. The methods used to add these extra templates is outlined below.

Addition of extra templates in the higher mass end of the bank

Extra templates were added to the initial bank in the total mass range of $80-400 M_{\odot}$ as shown in Fig. 38. To do this, a new bank was made, using the initial bank as seed, with templates in the total mass range of $80-400 M_{\odot}$ and a minimum match of 98%. No template duration threshold was used and a total of 14667 templates were added to the initial bank.

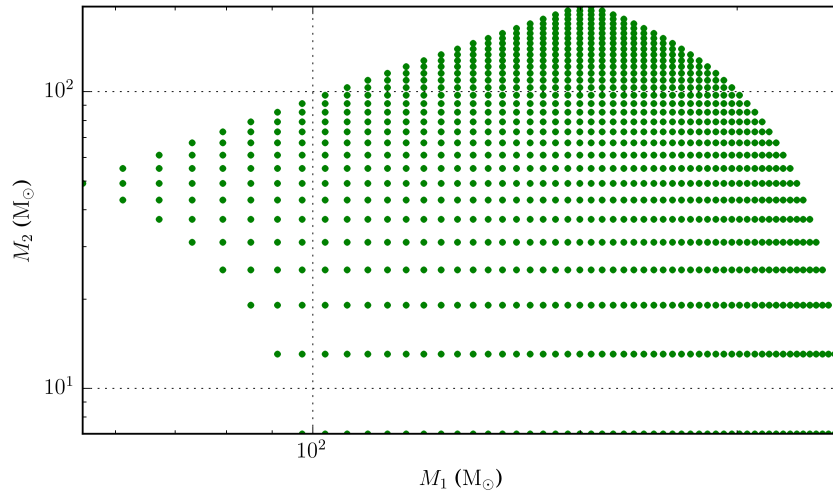


Figure 39 : The uniform grid bank with a 1000 templates spanning 100-400 M_{\odot} in total mass .

Placement of a grid of templates in the higher mass end

A grid of templates was formed using steps in the component masses of the templates, in the total mass range of 100-400 M_{\odot} , with mass ratios 1-97.9. A total of 1000 templates were generated without any cut on the template durations. The placement of the templates in such a grid was motivated by the intention of better assessment of noise properties. This gridded bank as shown in Fig. 39, was then added to the full bank.

All together, the final, improved O2 bank has a total of about 677000 templates as shown in Fig. 40.

Template bank used for the online GstLAL search

The online GstLAL-based inspiral pipeline search used a similar bank as was used by the initial offline search, before extra templates were added at the higher mass end, except it only had templates going up to a total mass of 150 M_{\odot} . The grouping of background noise was over the \mathcal{M} and χ parameters, done uniformly over the whole bank. It is the bank shown in Fig. 41

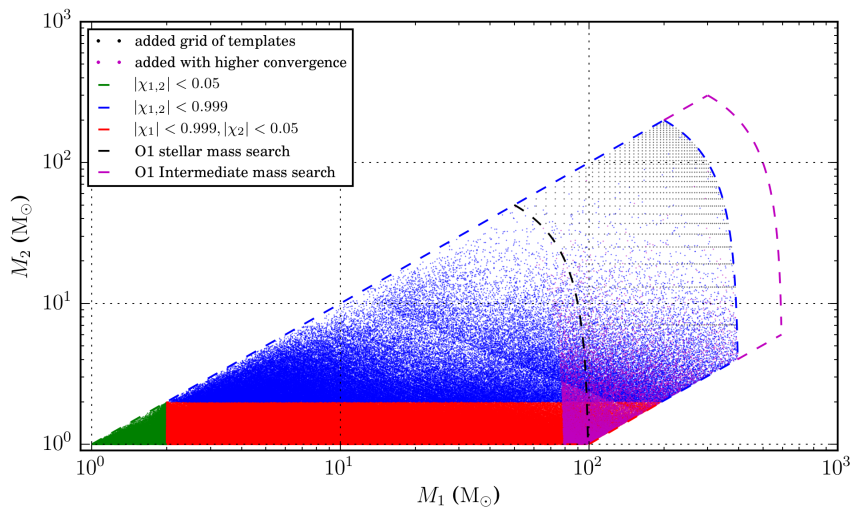


Figure 40 : A visual representation of the template bank used by the gstlal offline search in the second observing run in the component mass space.

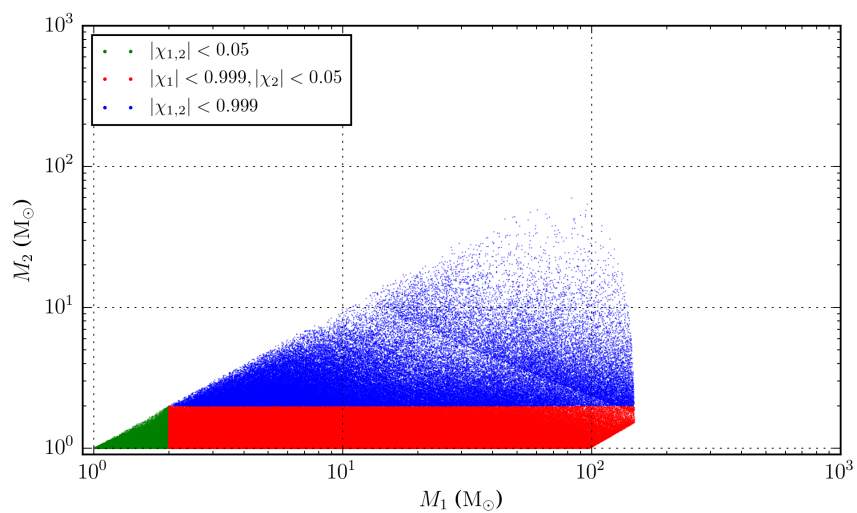


Figure 41 : A visual representation of the template bank used in the low-latency mode of the GstLAL-based inspiral pipeline, in the second observing run in the component mass space.

4.3.3 Overview of SVD binning and bank splitting done by GstLAL-based inspiral pipeline²

In order to detect a signal, the data has to be filtered through a bank of templates, which is not continuous, while the true binary parameter space is continuous. Since this introduces a loss in SNR (signal to noise ratio), an efficient method of covering the parameter space is required. Even then, a bank contains a lot of redundant templates that make the search cumbersome. Hence the GstLAL-based inspiral pipeline employs the LLOID method which combines singular value decomposition (SVD) with near critical-sampling to construct a reduced set of orthonormal templates to filter the data [9].

There are two major ways in which this can be done. The templates can be binned using the chirp mass and effective spin parameter χ_{eff} , hence forth referred to as χ parameter, or they can be binned equivalently by their time duration.

$\mathcal{M} - \chi$ binning: The template bank is first binned by χ , the number of such bins can be set. These bins are further binned by \mathcal{M} . Each of the final bins are called “split-banks”. The LLOID method of decomposing the bank, divides each split-bank into time slices, after ensuring each template has the same number of sample points after which the SVD algorithm is performed on them such that only the most important basis waveforms are returned [9].

duration binning: In this method, the original template bank is initially binned by template duration. These split-banks are then SVD decomposed like before.

The \mathcal{M} and χ are leading order parameters in the inspiralling phase of the waveform and hence are appropriately used to group or bin the templates for the lower mass systems. But for the higher mass systems (total mass $> 80M_{\odot}$) the part of the waveform within the LIGO band is dominated by the merger and ringdown phases, due to which \mathcal{M} and χ cannot be used for the grouping. Hence, below a total mass of 80, an $\mathcal{M}-\chi$ binning was used but above a total mass of 80, the templates are grouped by their duration in

²The methods described in this section are elaborated in [9].

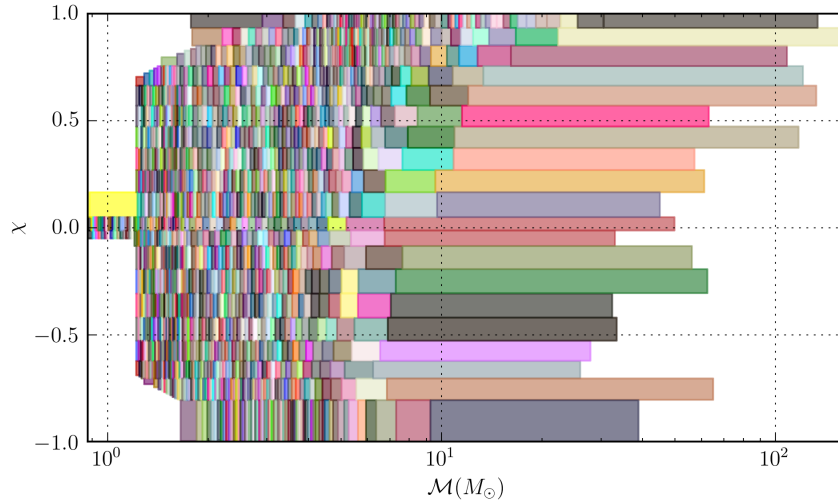


Figure 42 : The initial $\mathcal{M} - \chi_{\text{eff}}$ split banks where each color denotes a different svd bank

the LIGO band and a smaller number of templates are included in each group to ensure that templates with similar noise characteristics are grouped together.

4.4 Investigations of changes in template placement and binning styles

We present a step wise comparison of changes in the template and binning styles. We also discuss what effect such changes have on various aspects of the search.

We discuss the effect on the range sensitivity of the search, which is the distance out in space to which the detector is sensitive and is simply obtained from the space time volume sensitivity.

We also discuss the effect on the injection recovery which is shown by the characteristic SNR Vs \mathcal{M} plots where the injections that are missed or are found are shown. Injections at low SNRs are expected to be missed as the detector is not sensitive to them.

The closed box and the open box version of the number of events Vs inverse false alarm rate (IFAR) plots are shown. Closed box refers to a time shifted analysis i.e shifting by a time greater than the time of light propagation between the two detectors, so that data is not coincident. This is done to estimate background noise. The open-box results are the actual search results using coincident data. Our changes described here were

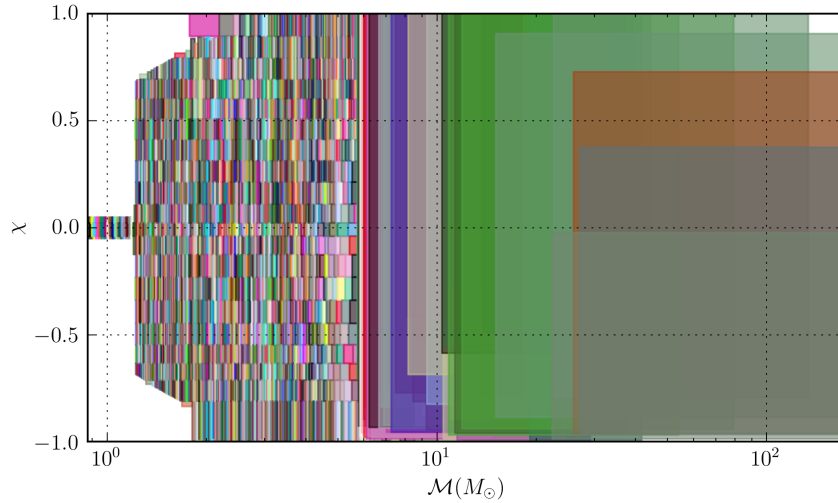


Figure 43 : A visual representation of the improved $\mathcal{M} - \chi_{\text{eff}}$ split banks where each color denotes a different svd bank. Above a total mass of $80 M_{\odot}$ the binning was done by template duration instead of the $\mathcal{M} - \chi$ binning done below it.

mostly intended to reduce the coincident noise as seen in the closed-box plots. Vast deviations from the dashed expected line, indicates loud or significant trigger. Binning together templates that are widely different in noise characteristics, in the higher mass region of the bank, cause incorrect background estimation and hence incorrect ranking of coincident triggers which is what caused loud noise to show up in the time-shifted closed box plots.

These investigations were what inspired the changes applied to the initial version of the bank, as described earlier.

4.4.1 \mathcal{M} - χ binning Vs template duration based binning

As shown in Fig. 44, range sensitivity is seen to fall for duration binning compared to \mathcal{M} - χ binning at high masses (almost no change for lower masses).

Duration binning causes more injections to be missed at higher SNRs compared to \mathcal{M} - χ binning.

\mathcal{M} - χ binning, compared to duration binning shuffles the significances and it is hard to conclude.

Duration binning seems to find a marginally interesting candidate while \mathcal{M} - χ binning binning does not.

4.4.2 \mathcal{M} - χ binning vs duration based binning with unequal number of templates (hierarchical) in each bin

As shown in Fig. 45, the hierarchical binning lowers the range slightly (within error bars) for the higher mass bins.

Hierarchical binning causes more injections to be missed, both at lower and higher \mathcal{M} . Hierarchical binning reduces multiple noise events and replaces them with one louder noise event.

Hierarchical binning leads to a candidate with a high IFAR.

4.4.3 1000 template grid addition Vs 5000 template grid addition to the bank

As shown in Fig. 46, going from a grid of 1000 to 5000 increases range for the highest \mathcal{M} bin, decreases it for the 2nd highest \mathcal{M} bin, especially at high CFAR and leaves the lower \mathcal{M} bins unaffected.

Also, more injections are missed for the 5000 grid at higher SNR.

Almost no difference seen for the closed-box plot, while for the open box plot one loud candidate seen for both.

4.4.4 Uniform duration based binning Vs duration based binning with unequal number of templates (hierarchical) in each bin

As shown in figure 47, hierarchical binning increases range for higher \mathcal{M} bins, especially at lower CFAR.

Hierarchical binning shifts around the missed and found injection, but does not change the overall recovery appreciably.

With Hierarchical binning noise is better constrained within ~ 1 sigma.

A loud candidate is seen for both, but with higher IFAR for hierarchical binning.

4.4.5 No grid Vs addition of 1000 template grid to the bank in case of \mathcal{M} - χ binning

As shown in Fig. 49, addition of 1000 template grid lowers the range for higher \mathcal{M} bins. More injections are missed with the addition of the 1000 template grid.

A louder non-zero lag noise seen for the 1000 template grid addition.

Zero lag or coincident noise seems better constrained with the addition of the grid.

4.4.6 No grid Vs addition of 1000 template grid to the bank in case of duration based binning

As shown in Fig. 49, range decreases at high CFAR and increases at low CFAR on addition of the grid for the highest \mathcal{M} bin, range increases almost uniformly for the 2nd highest \mathcal{M} bin, on adding the grid.

More high \mathcal{M} injections are missed on adding the bank.

No appreciable change for the closed-box or non-zero lag plot.

Louder coincident noise seen on adding the bank at zero lag.

4.5 Effectiveness of the O2 bank ³

For a matched filter based search, recovering the maximum SNR that can be recovered for a given astrophysical system (called the optimal SNR) requires the maximum possible match between the signal and the waveform of the template. However, since the template bank is discrete and the accuracy to which gravitational waveforms from different astrophysical systems can be modeled at present is limited, not all of this optimal SNR can be recovered. The fraction of the optimal SNR recovered by the bank is known as the fitting factor ϕ . Hence for a population of finite sources that can be detected with ideally matching templates, only a fraction can be actually observed, which is known as

³reference for definition of fitting factor arXiv:1705.01845. The plots for this section were generated in close collaboration with Sarah Caudill and Surabhi Sachdev and are most likely to be a part of the paper in preparation.

the recovery fraction α and it is less than 1. Hence fitting factor can be defined as:

$$\alpha = \frac{\int d\vec{x} \phi(\vec{x})^3 \sigma(\vec{x})^3}{\int d\vec{x} \sigma(\vec{x})^3} \quad (4.5.1)$$

where \vec{x} is the parameters of the source (excluding the luminosity distance), while $\sigma(\vec{x})$ is the distance at which the optimal SNR of the source takes a fixed value, which when taken to be 8, causes $\sigma(\vec{x})$ to be the horizon distance. Hence banks need to be tested against simulated waveforms of different types of astrophysical populations and the fitting factor between the waveforms and the templates, calculated so as to form an idea about the effectualness of the bank, which effects the sensitivity of the search. It is expected to be higher than 90% in most cases. To compute Eq. 4.5.1, the integral is replaced by a summation over the finite set of simulations, which are large enough in number. Simulations of merger signals from various populations of such objects, called injections, are typically mixed into the data searched by the pipeline, to check their recovery by the search. To check for the effectivity of the bank, multiple injection sets of the same population were used, varying in the type of waveform, mass ranges covered and whether the spin is aligned to orbital angular momentum. Non spinning, higher order mode type of injections for the IMBH binaries were also used and recovered, showing that the search is capable of such detections in the IMBH region. SpinTaylorT4 [37] and TaylorF2 [6] types of waveforms were used for BNS injections, while the NSBH injections were used with IMRPhenomPv2 [38] for the precessing case and SEOBNRv4_ROM [39] for the non precessing case. SEOBNRv4_ROM was used for BBHs. SEOBNRv4_ROM type of injections were used for the spin aligned IMBHs while EOBNRv2HM_ROM were used for the non-spinning higher order mode injection set.

For the TaylorF2, spin aligned BNS injection set in Fig. 51, the fitting factors seem to be above 0.97 below a total mass of 4, however the fit declines down to 0.94 thereafter. A possible reason could be lack of sufficient injections around 4 solar masses in total mass, where the templates change waveform from TaylorF2 to the SEOBNRv4_ROM type. The spinning BNS injection set in Fig. 50 is recovered with lower fitting factors, especially outside $-0.1 < \chi < 0.1$. The high mass aligned spin NSBH injections in Fig. 52 seem to be recovered with adequately high fitting factors, the lowest being above 0.96.

Population	Mass(M_{\odot})	Spin	Waveform
BNS	$m_{1,2} \in [1, 3]$	$\chi_{1,2} \in [0.0, 0.4]$ pre-cessing	SpinTaylorT4
BNS	$m_{1,2} \in [1, 3]$	$\chi_{1,2} \in [0.0, 0.05]$ aligned	TaylorF2
NSBH	$m_1 \in [2, 399]$ $m_2 \in [1, 2]$	$\chi_{1,2} \in [0.0, 0.99]$ pre-cessing	IMRPhenomPv2
NSBH	$m_1 \in [1, 3]$ $m_2 \in [3, 97]$	$\chi_1 \in [0, 0.4]$ $\chi_2 \in [0, 0.989]$ aligned	SEOBNRv4_ROM
BBH	$m_1 \in [2, 99]$ $m_2 \in [2, 99]$	$\chi_1 \in [0, 0.99]$ $\chi_2 \in [0, 0.99]$ aligned	SEOBNRv4_ROM
IMBH	$m_1 \in [1, 399]$ $m_2 \in [1, 399]$	$\chi_1 \in [0, 0.998]$ $\chi_2 \in [0, 0.998]$ aligned	SEOBNRv4_ROM
IMBH	$m_1 \in [50, 350]$ $m_2 \in [50, 350]$	non-spinning	EOBNRv2HM_ROM

Table 7 : Description of different categories of astrophysical populations, in terms of their mass and spin parameters, that were used as the simulations, injected to test the sensitivity of the bank towards them.

The aligned spin BBH in Fig. 54 injections seemed to be recovered well, except for very low masses and χ higher than about 0.5, for which the fitting factor is found to be relatively low. The precessing NSBH injections in Fig. 53 seem to be recovered well for the positive χ_{eff} systems, but not so well for the negative ones. On the other hand the extreme mass ratio systems seem to be recovered with a poorer fit, which is what we expect. For the spinning IMBH injections in Fig. 55, the fitting factor is lower for the highly spinning injections. The non precessing IMBH injections including higher order modes in Fig. 56 have lower fitting factor for higher masses and for more extreme mass ratios. This is to be expected as our bank does not include templates including higher order mode waveforms and higher order modes become more prominent at higher mass ratios.

Overall, most of the injections seem to be recovered to match templates by a fitting factor over 90%. The fitting factor seems to be lower for very low mass BNS systems around the templates where a transition in waveforms happen and for the non spinning IMBH injections including higher order modes.

4.6 Results and conclusions

We have tried to present the construction and the effectuality of the bank used by the GstLAL-based inspiral pipeline, for the second observing run of LIGO. The bank we have described, covers a diverse parameter space and is capable of recovering gravitational signals from binary neutron stars, binary black holes, neutron star and black hole binaries and even intermediate mass binary blackholes. The search was expanded from being a stellar mass only search in O1 to being an integrated search including heavier mass black hole binaries, going up to a total mass of 400 solar masses.

The present bank however contains templates that assume the spins of the stars to be aligned with their orbital angular momentum. They do not include precession. Hence precessing waveforms are recovered with a lower fit with the templates that recover them.

The bank also does not include templates with higher order modes in their waveforms. Hence while signals or simulations containing higher order modes can be recovered, but the match between the signals and the template that recovers them, is low. Presence of higher order modes is significant for higher mass ratio systems, and are capable of increasing the sensitivity of the search towards higher mass systems. This is because, the higher order mode enters the LIGO frequency band earlier than the fundamental mode and hence allows more power within the band which is significant for the detection of the short glitch-like signals of the higher mass systems. Hence it will become important to include templates containing higher order modes in their waveforms.

The bank includes templates for systems with mass ratios going from 1-97.989. It could be expanded to include systems with higher mass ratios as well.

Finally, the density of the bank and the grouping of the background noise of the search is suboptimal. Grouping of very different templates together in the higher mass end of the bank, in the initial version of the O2 bank, caused incorrect calculation

of significances of glitches due to erroneous estimation of the background. This was corrected, as described earlier, by the current version of the bank, which includes extra templates in the higher mass end and also groups together templates with more similar noise characteristics. However including more templates in the higher mass region, increased possible accidental recoveries and hence decreased the sensitivity of the template bank in this region. A more optimally constructed bank would be needed in the future.

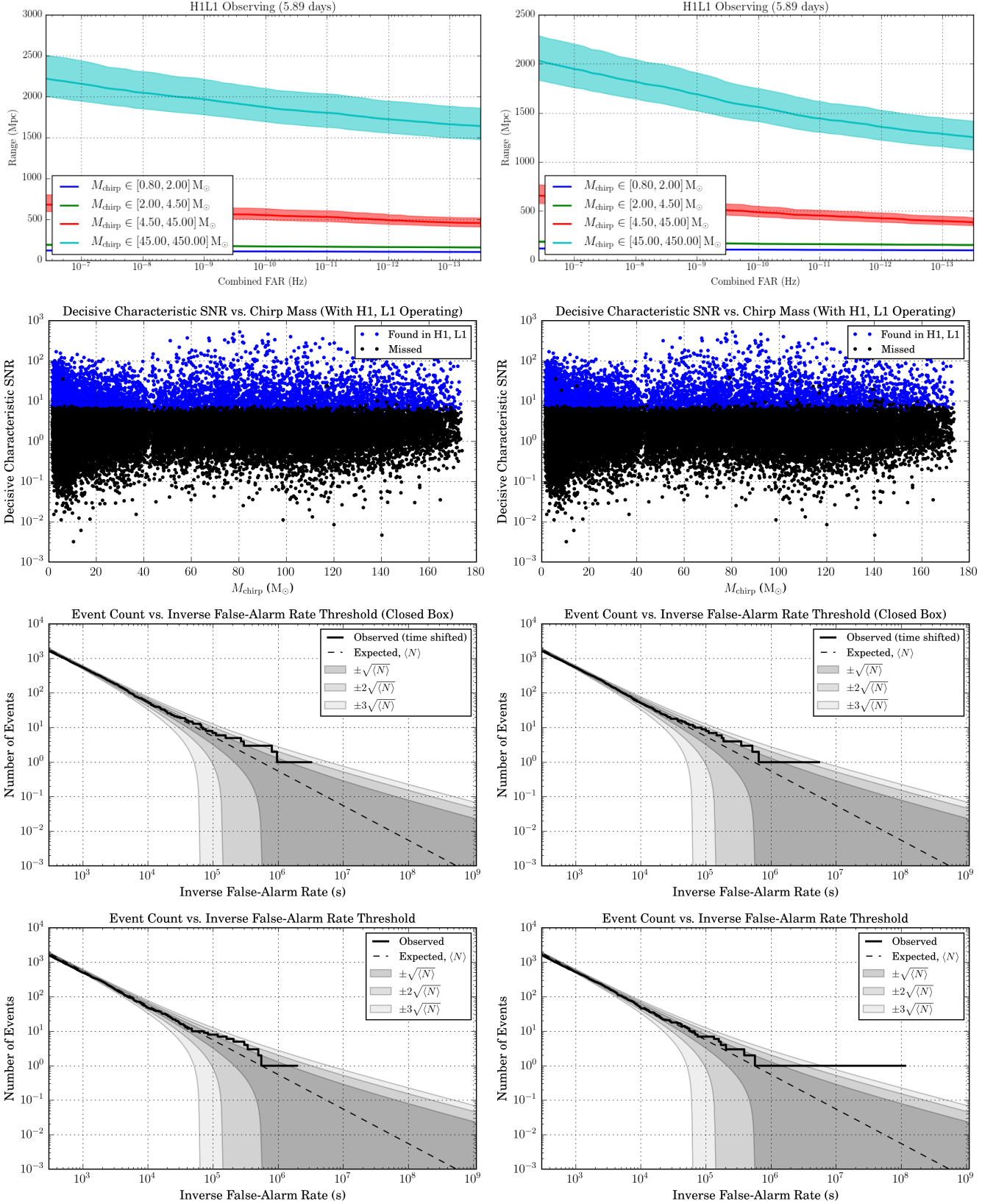


Figure 44 : Plot comparisons between two runs over the same chunk of data, i.e O2 chunk 6 (GPS: 1170948618-1171632618) but using different banks. The plots on the left are from an analysis where the templates were binned by \mathcal{M} - χ while those on the right are from an analysis where the binning was by template duration. On the whole, duration binning causes more injections to be missed and range sensitivity to be lower.

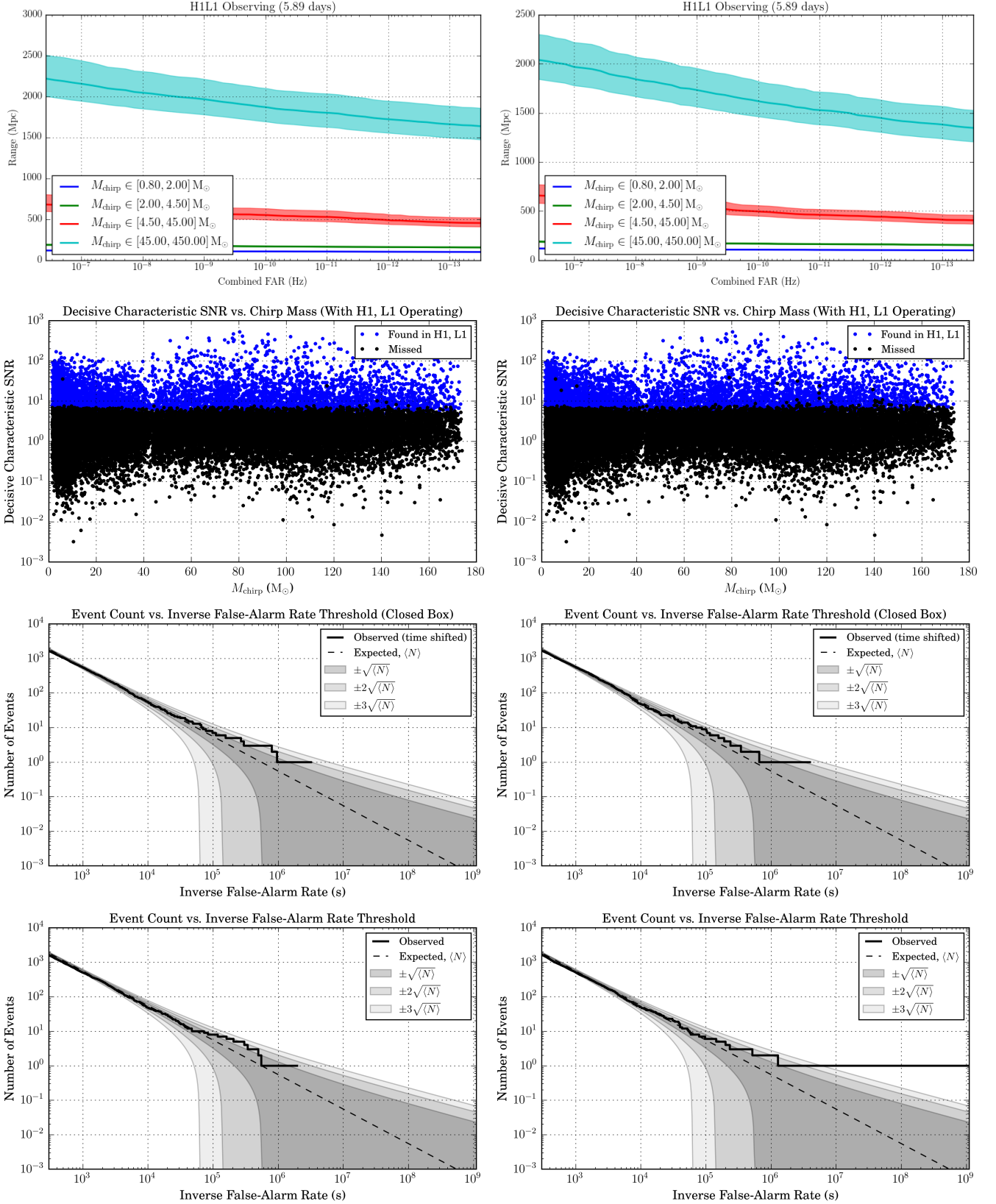


Figure 45 : Plot comparisons between two runs over the same chunk of data, i.e O2 chunk 6 (GPS: 1170948618-1171632618) but using different banks. The plots on the left are from an analysis where the templates were binned by $\mathcal{M}\text{-}\chi$ while those on the right are from an analysis where the binning was by template duration with unequal number of templates in each bin. Hierarchical duration binning seems to cause more injections to be missed.

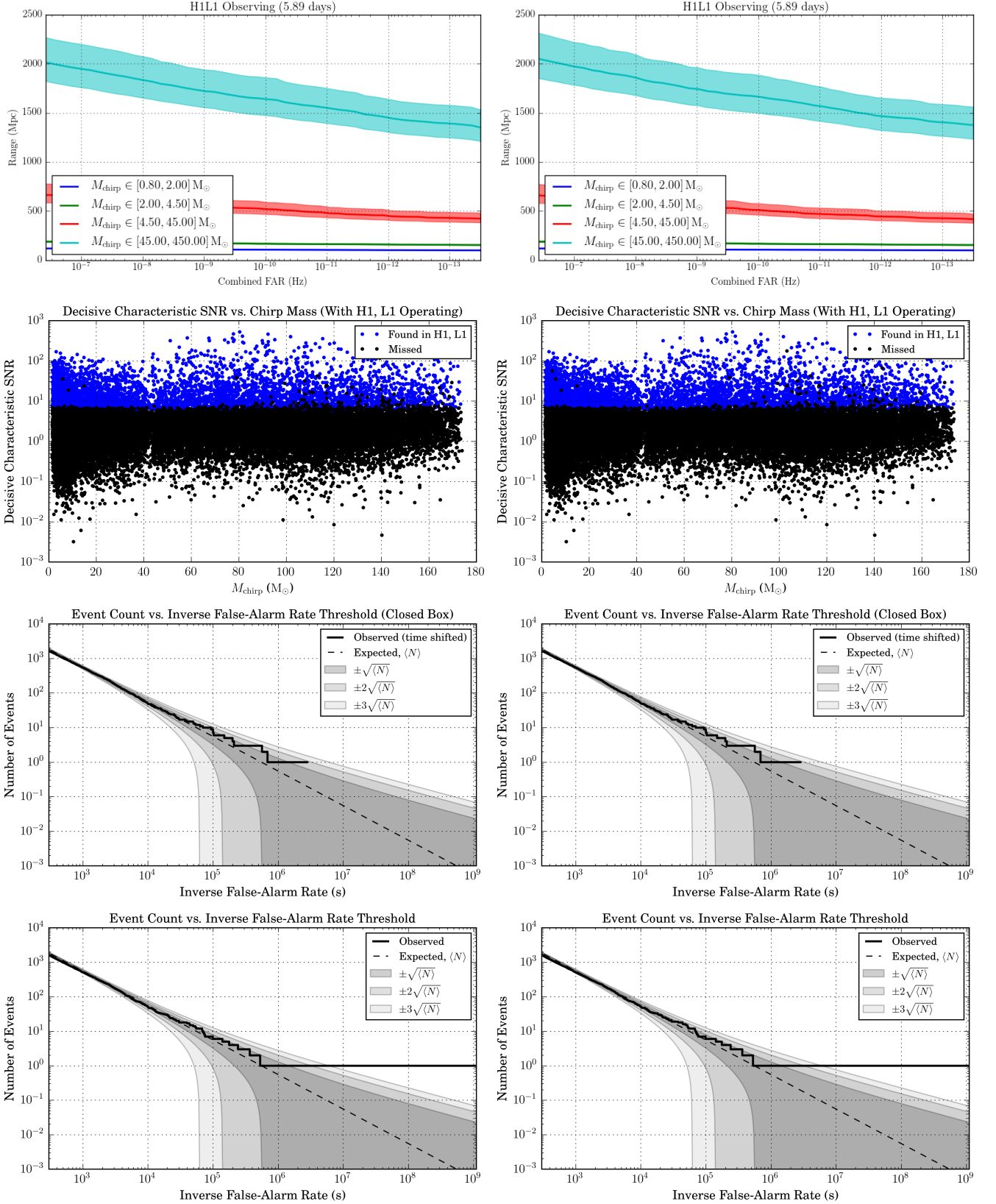


Figure 46 : Plot comparisons between two runs over the same chunk of data, i.e O2 chunk 6 (GPS: 1170948618-1171632618) but using different banks. The plots on the left are from an analysis where a grid containing 1000 templates were added to the bank, while those on the right are from an analysis where a grid with 5000 templates was added. It seems the addition of a larger grid causes a marginal increase in range sensitivity for higher masses, but also increases the number of injections missed.

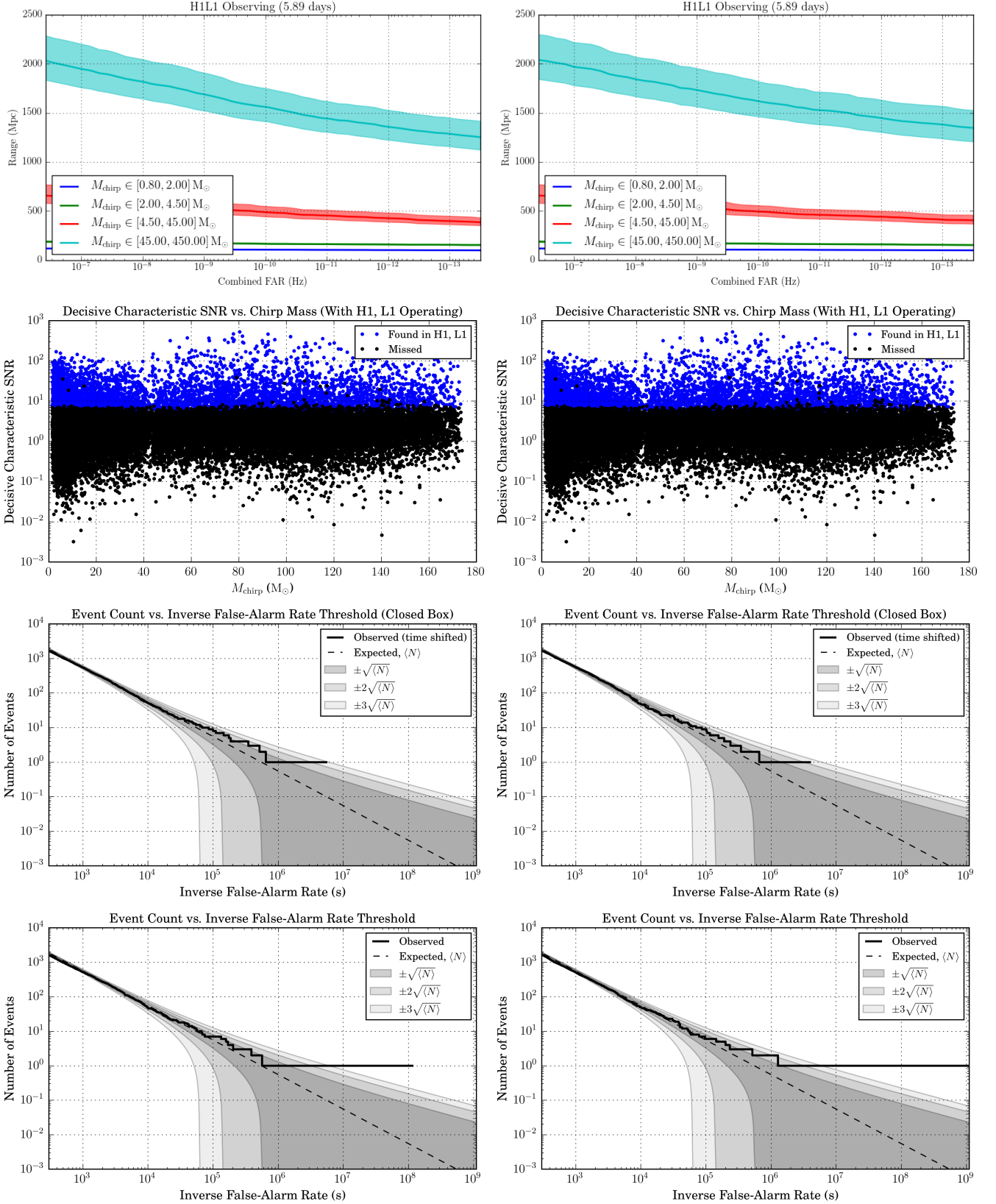


Figure 47 : Plot comparisons between two runs over the same chunk of data, i.e O2 chunk 6 (GPS: 1170948618-1171632618) but using different banks. The plots on the left are from an analysis where the templates were binned by template duration with equal number of templates in each bin while those on the right are from an analysis where the binning was by template duration with unequal number of templates in each bin. The hierarchical binning seems to constrain noise better and increases range for higher masses.

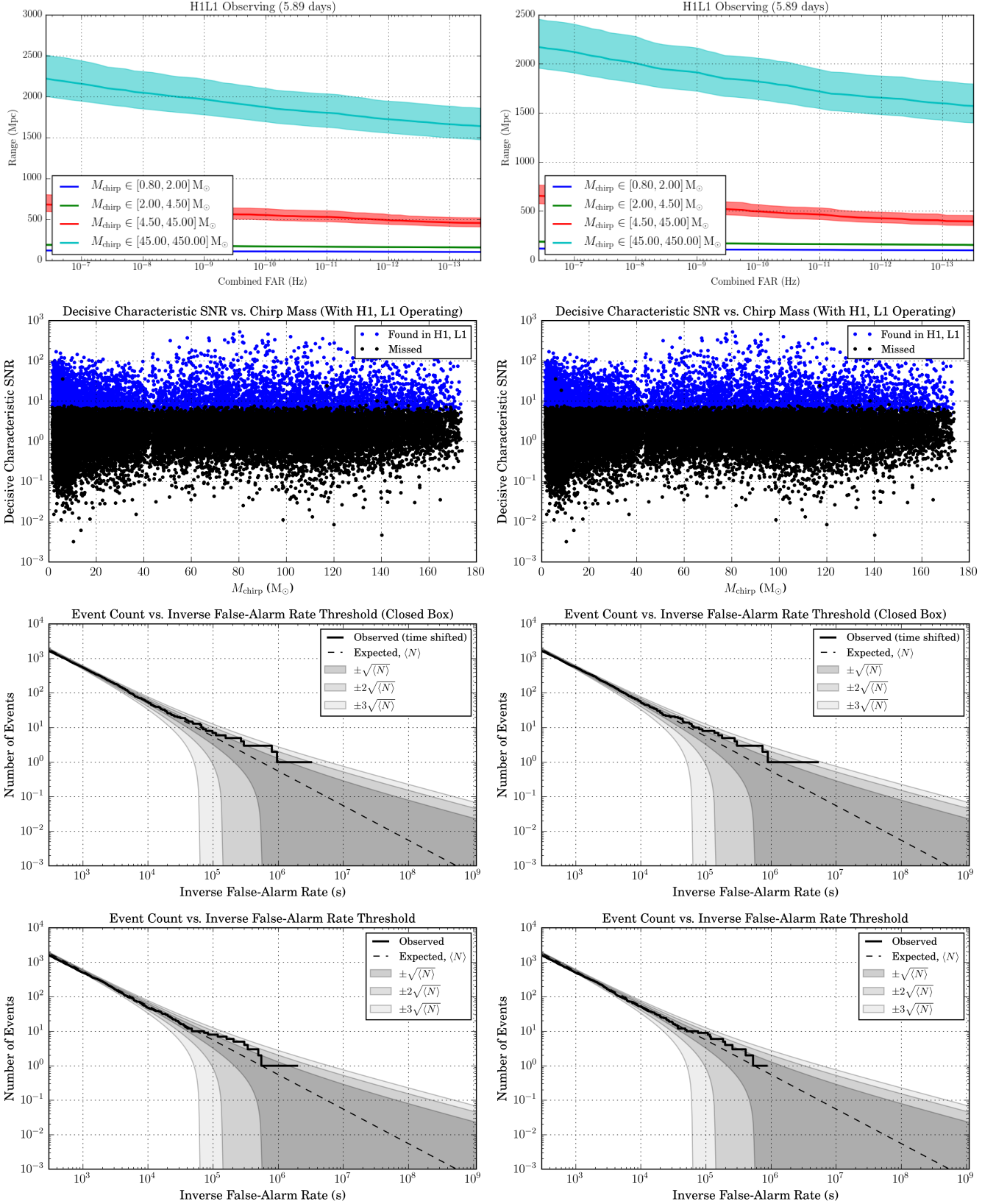


Figure 48 : Plot comparisons between two runs over the same chunk of data, i.e O2 chunk 6 (GPS: 1170948618-1171632618) but using different banks. The plots on the left are from an analysis where the bank did not contain a grid while those on the right are from an analysis where a 1000 template grid was added, both cases using an \mathcal{M} - χ binning. The grid increases missing of injections, but constrains coincident noise better.

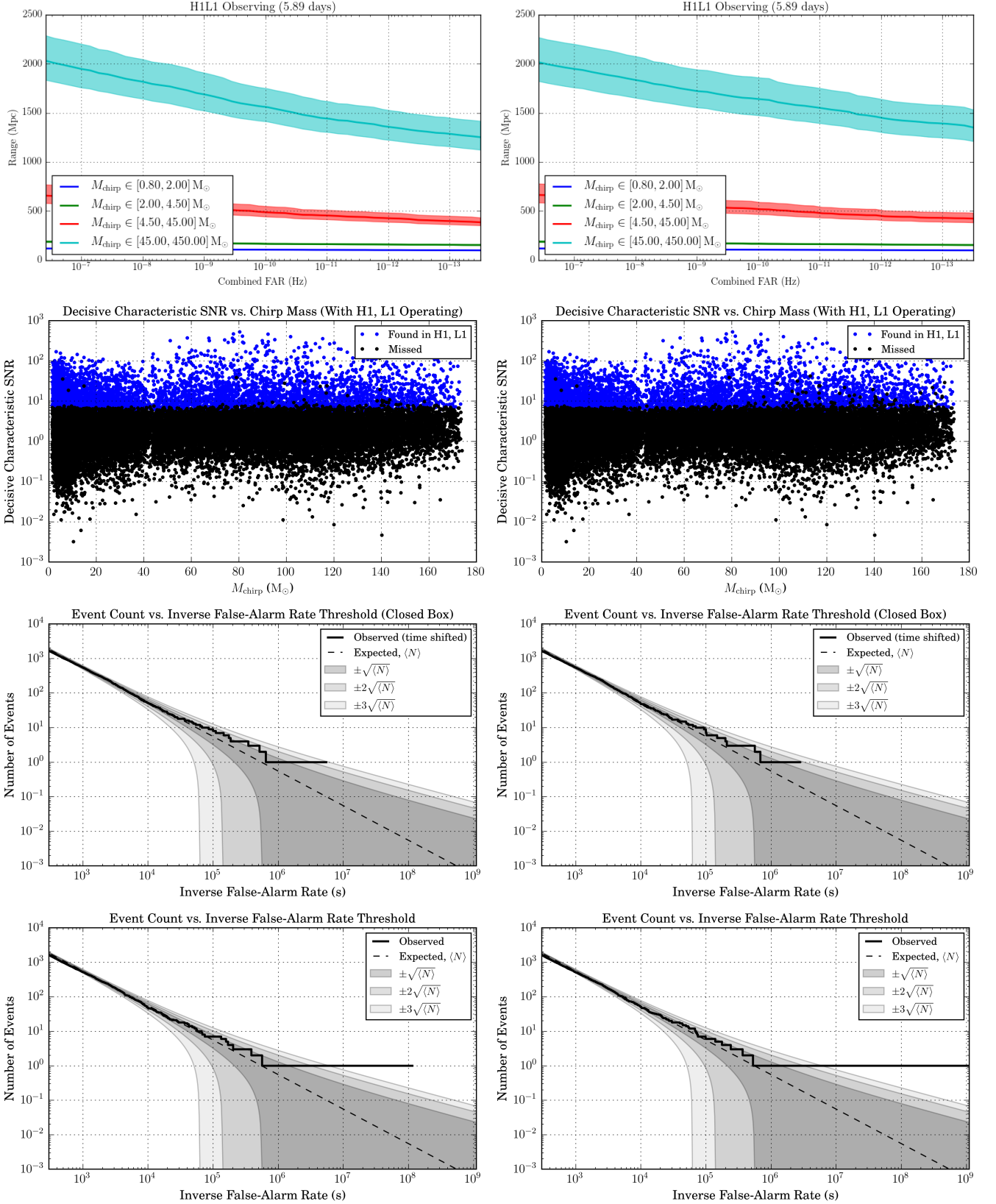


Figure 49 : Plot comparisons between two runs over the same chunk of data, i.e O2 chunk 6 (GPS: 1170948618-1171632618) but using different banks. The plots on the left are from an analysis where the bank did not contain a grid while those on the right are from an analysis where a 1000 template grid was added, both cases using a duration based binning. Range decreases at high CFAR and increases at low CFAR on addition of the grid for the highest mass bin

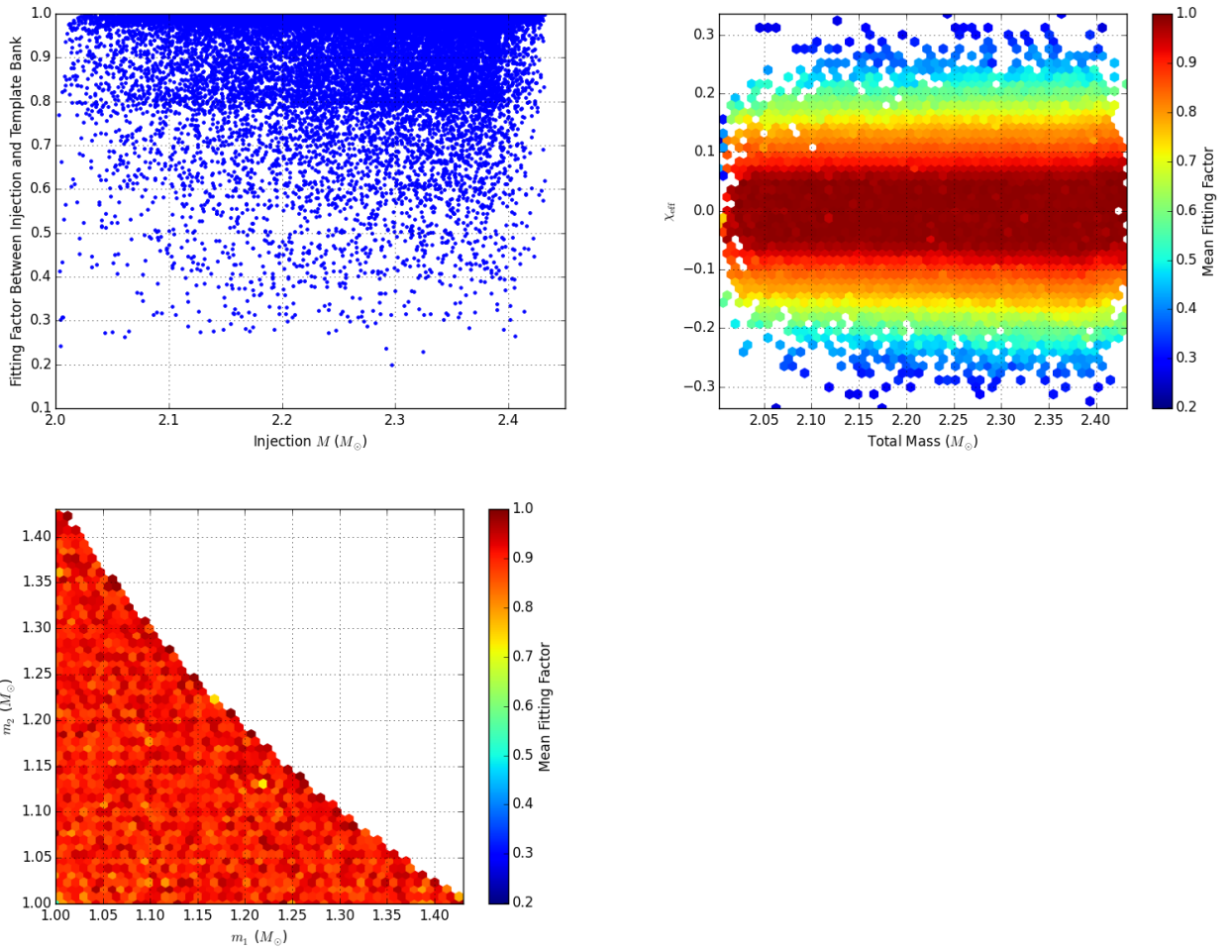


Figure 50 : The plots show the fitting factor between the templates and the waveforms of the BNS SpinTaylorT4 type of injections. The 1st plot shows the fitting factor as a function of the injected total mass, the 2nd plot shows the fitting factors in the \mathcal{M} - χ_{eff} plane, the 3rd plot shows the same in the component mass plane. The injections seem to be recovered with lower fitting factors, especially outside $-0.1 < \chi < 0.1$

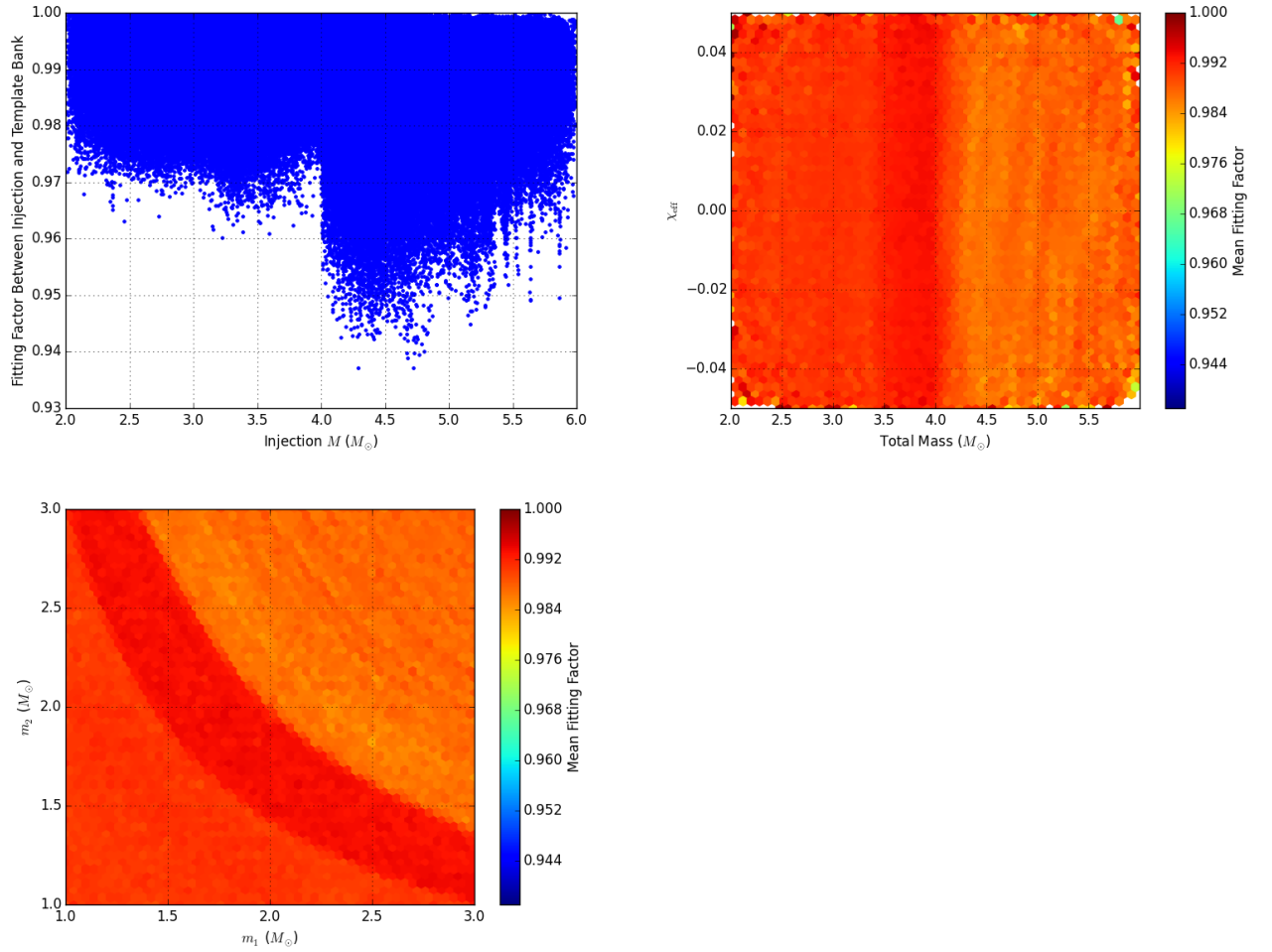


Figure 51 : The plots show the fitting factor between the templates and the waveforms of the BNS TaylorF2 type of injections. The 1st plot shows the fitting factor as a function of the injected total mass, the 2nd plot shows the fitting factors in the \mathcal{M} - χ_{eff} plane, the 3rd plot shows the same in the component mass plane. The fitting factors seem to be above 0.97 below a total mass of 4, however the fit declines down to 0.94 thereafter, possibly due to lack of sufficient injections around 4 M_\odot where the template bank changes its approximants.

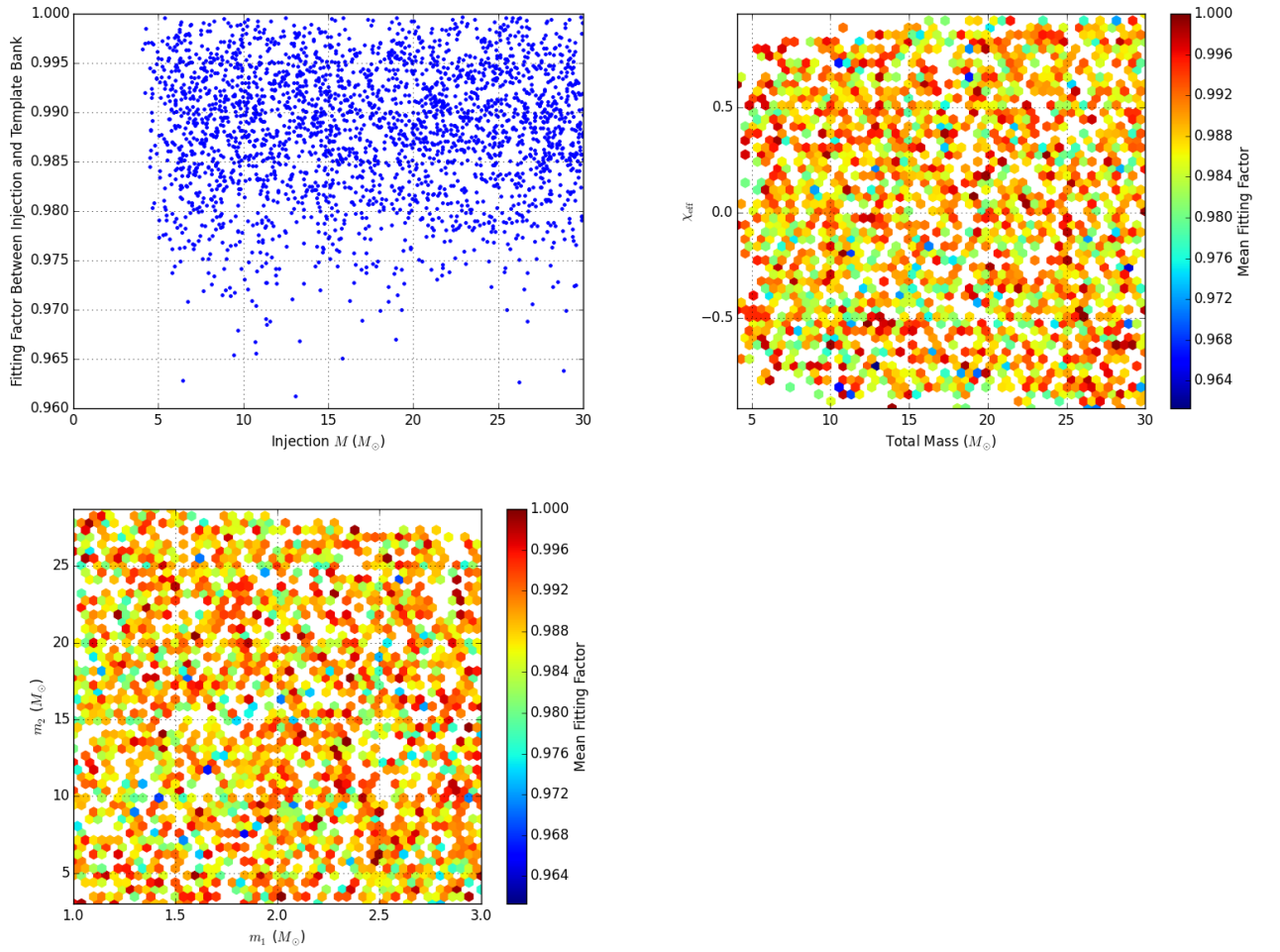


Figure 52 : The plots show the fitting factor between the templates and the waveforms of the NSBH SEOBNRv4_ROM type of injections. The 1st plot shows the fitting factor as a function of the injected total mass, the 2nd plot shows the fitting factors in the \mathcal{M} - χ_{eff} plane, the 3rd plot shows the same in the component mass plane. The injections are covered with adequately high fitting factors, the lowest being above 0.96.

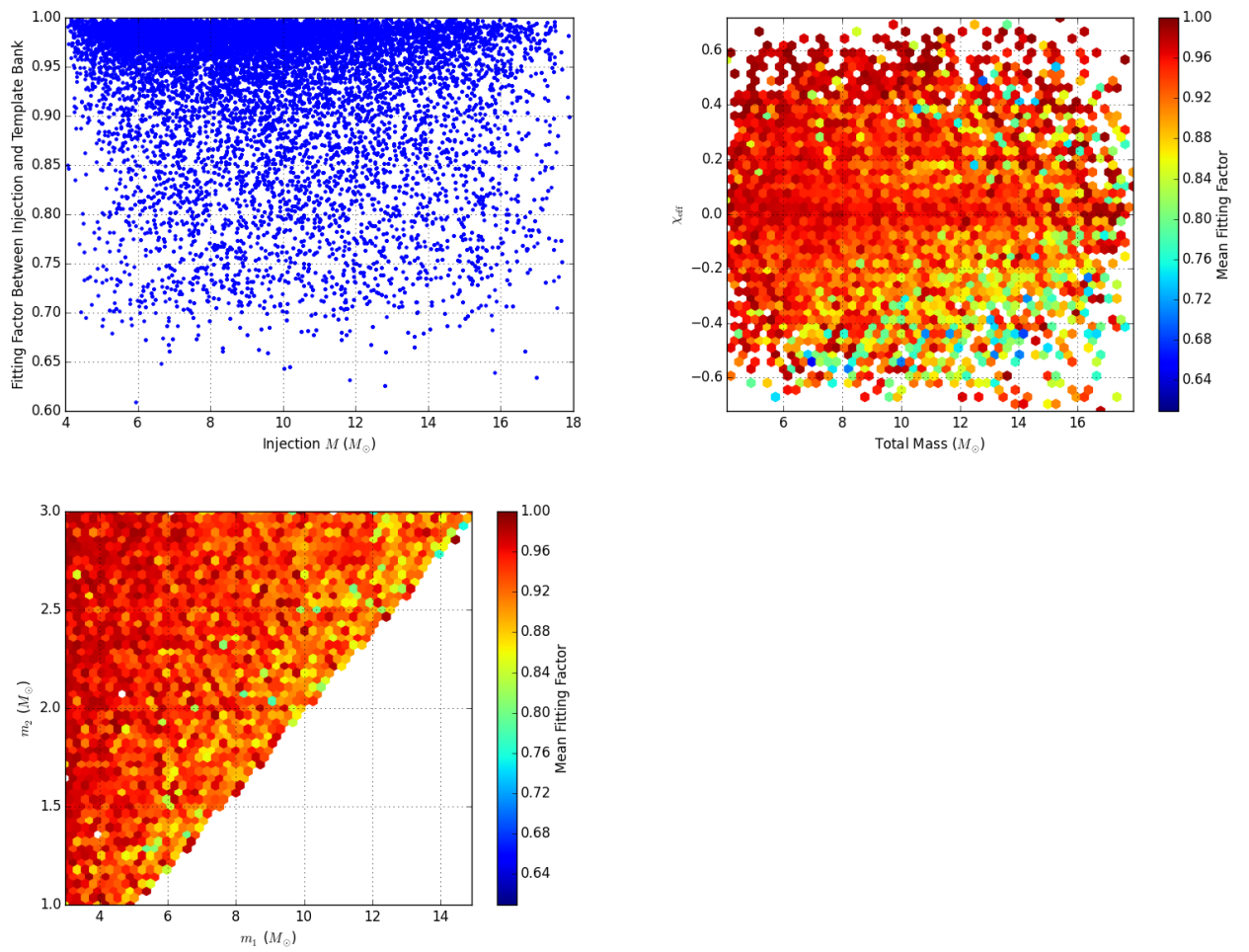


Figure 53 : The plots show the fitting factor between the templates and the waveforms of the NSBH IMRPhenomPv2 type of injections. The 1st plot shows the fitting factor as a function of the injected total mass, the 2nd plot shows the fitting factors in the \mathcal{M} - χ_{eff} plane, the 3rd plot shows the same in the component mass plane. These injections are recovered well for the positive χ_{eff} systems, but not so well for the negative ones. On the other hand the extreme mass ratio systems seem to be recovered with a poorer fit, which is what we expect.

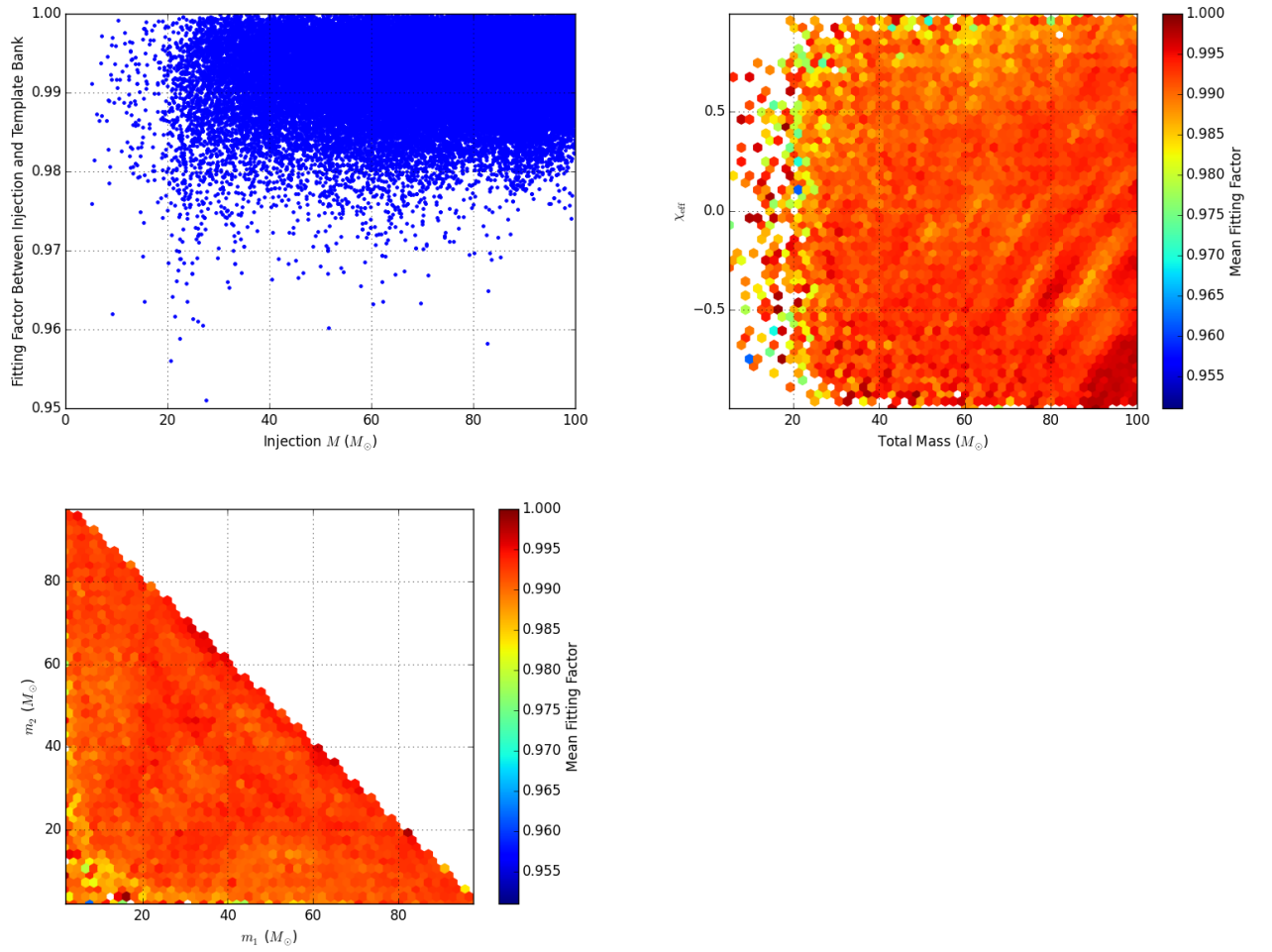


Figure 54 : The plots show the fitting factor between the templates and the waveforms of the BBH SEOBNRv4_ROM type of injections. The 1st plot shows the fitting factor as a function of the injected total mass, the 2nd plot shows the fitting factors in the \mathcal{M} - χ_{eff} plane, the 3rd plot shows the same in the component mass plane. The injections seemed to be recovered well, except for very low masses and χ higher than about 0.5, for which the fitting factor is found to be relatively low.

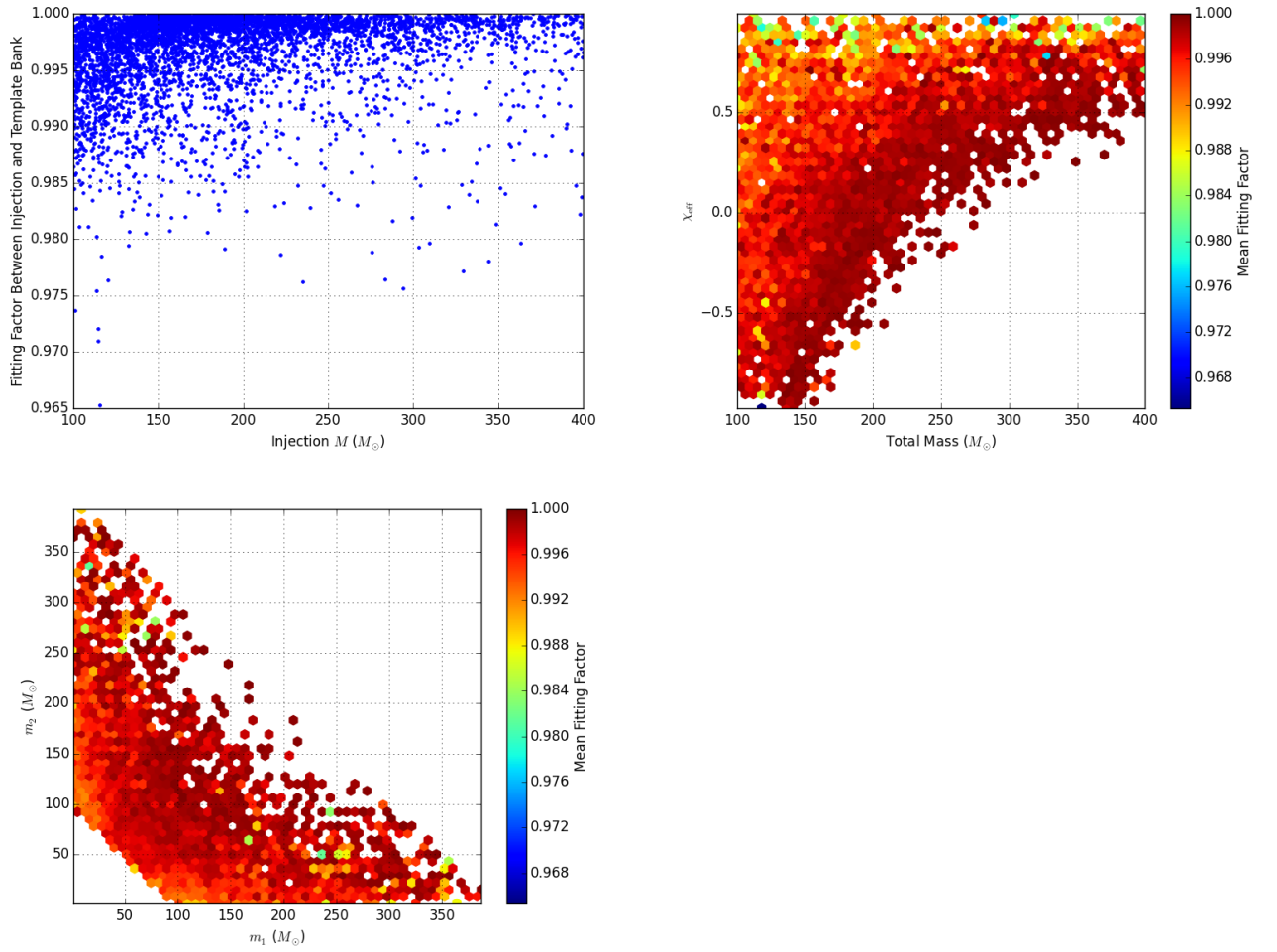


Figure 55 : The plots show the fitting factor between the templates and the waveforms of the IMBH SEOBNRv4_ROM type of injections. The 1st plot shows the fitting factor as a function of the injected total mass, the 2nd plot shows the fitting factors in the \mathcal{M} - χ_{eff} plane, the 3rd plot shows the same in the component mass plane. The fitting factor is lower for the highly spinning injections.

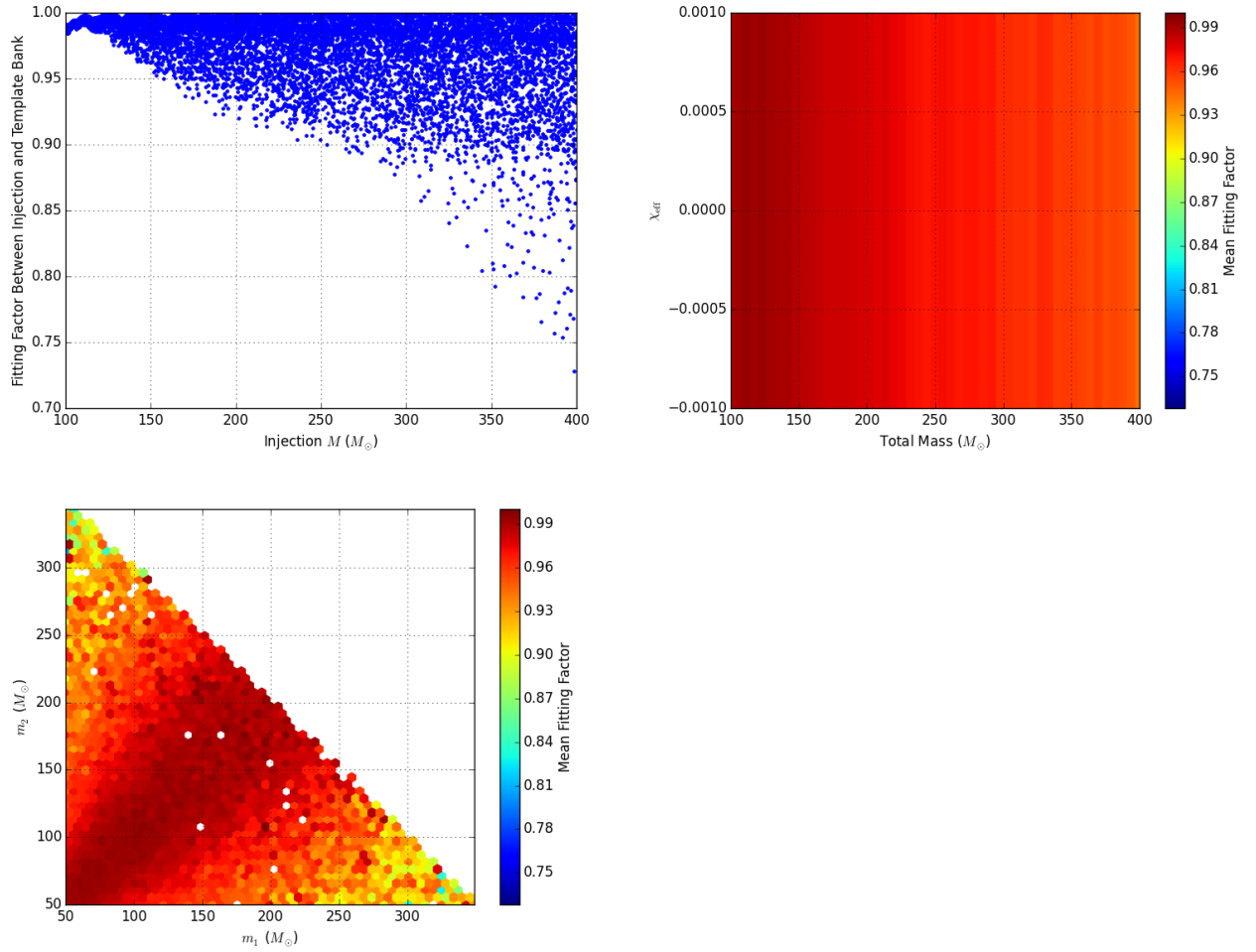


Figure 56 : The plots show the fitting factor between the templates and the waveforms of the IMBH EOBNRv2HM_ROM type of injections. The 1st plot shows the fitting factor as a function of the injected total mass, the 2nd plot shows the fitting factors in the $\mathcal{M}-\chi_{eff}$ plane, the 3rd plot shows the same in the component mass plane. The injections have lower fitting factor for higher masses and for more extreme mass ratios. This is to be expected as our bank does not include templates including higher order mode waveforms and higher order modes become more prominent at higher mass ratios.

Chapter 5

Contributions to the IMBH search and its improvement

5.1 The IMBH search region and astrophysical populations targeted in O1

Intermediate mass binary black holes (IMBH) are mostly defined as black holes with masses between $10^2 M_{\odot}$ and $10^5 M_{\odot}$. Their exact origin is unknown but they are hypothesized to form inside dense globular clusters (GC) due to hierarchical merging of stellar mass black holes. Some of the other competing theories are (i) direct collapse of massive first-generation, low metallicity Population III stars [31], (ii) runaway mergers of massive main sequence stars in dense stellar clusters [31], (iii) the accretion of residual gas onto stellar-mass black holes [40], and (iv) chemically homogeneous evolution [31]. The first observing run of Advanced LIGO lasted between September 12, 2015 and January 19, 2016 including a total of 51.5 days of coincident analysis time between the two detectors, located in Hanford, Washington (H1), and Livingston, Louisiana (L1). The gravitational wave signals observed during this period came from two stellar mass binary black holes (BBH), being named GW150914 [3] and GW151226 [24] and a low-significance candidate called LVT151012. However as no IMBH was observed, only upper limits could be placed on their possible rates of observation.

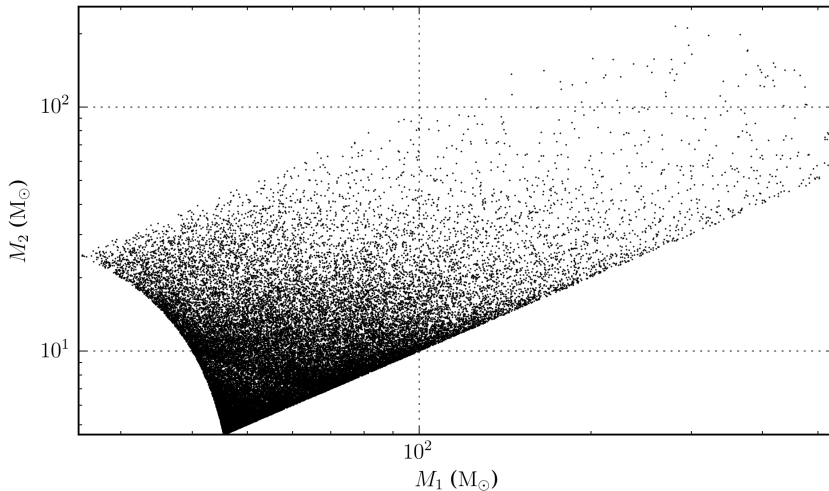


Figure 57 : A visual representation of the original IMBH only dedicated search bank used in the first observing run of Advanced LIGO (O1), in the component mass space.

Both un-modeled and modeled searches were used in O1, to search for IMBHs. The independent modeled searches include the GstLAL-based inspiral pipeline based search [9] and the PyCBC search. The un-modeled search includes the Coherent Wave Burst (cWB) search [41] which looks for coherent triggers with excess power compared to the noise level. In this chapter we discuss the comparison of the GstLAL-based inspiral pipeline based search to the IMBH region in O1 and O2, especially with respect to spacetime volume sensitivity and inclusion of higher order modes in the waveforms.

In O1, the dedicated search for IMBHs by the GstLAL-based inspiral pipeline, comprised matched filtering of data against a discrete bank of waveform templates. The bank spanned over binary systems with total masses in the range 50 to 600 M_{\odot} and dimensionless spins $\chi_{1,2}$ in the range -0.99 and 0.99. The positive and negative values of the spins denote alignment and anti-alignment with the angular momentum of the system, respectively. The mass ratios of the systems were kept between 0.1 and 1.

The templates used waveforms which are a reduced-order model of a double aligned-spin effective-one-body waveform [31]. The bank used by the GstLAL inspiral based pipeline which included 44,902 templates, has been shown in Fig. 57. Since the signals from such heavy mass systems are expected to spend less time within the LIGO band,

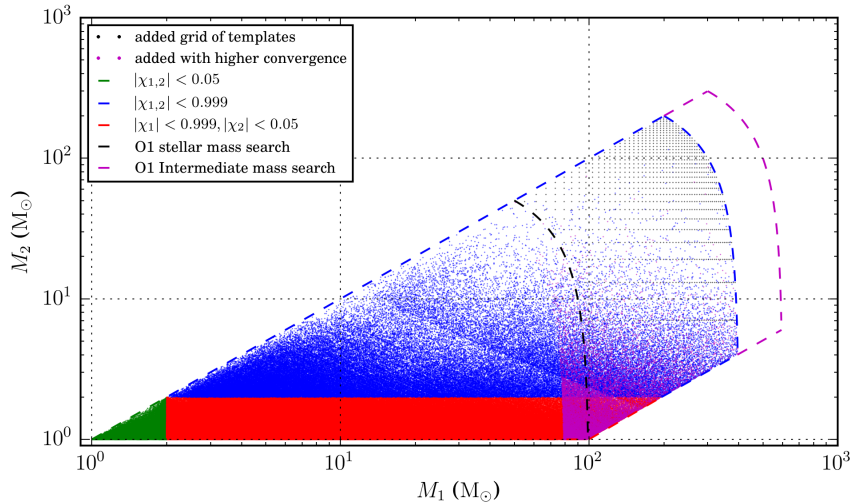


Figure 58 : A visual representation of the template bank used in the 2nd observing run of Advanced LIGO and Virgo (O2), in the component mass space. The search region corresponding to the O1 IMBH search region is shown.

they are likely to be lost due to the noise characteristics at low frequencies [31], hence GstLAL began its analysis at a frequency of 15 Hz.

5.2 The search in 1st observing run vs 2nd observing run

The search for compact objects by the GstLAL-based inspiral pipeline in the the second observing run (O2) of LIGO and Virgo, has been described in detail in chapter 4. As can be appreciated from that, certain changes were made to the search. The search in O2 used a template bank including stellar mass systems and IMBH systems, with total masses ranging from $2M_{\odot}$ - $400M_{\odot}$, such that the searches were not separated. The O2 bank containing a total of 677000 templates has been depicted in Fig. 58. The lower cut off frequency for the search in O2 was 15Hz. The binning of templates with similar background noise characteristics was done differently in the two searches. In O1 IMBH search, the binning was in \mathcal{M} and χ plane. In the second observing run, the binning was in \mathcal{M} and χ up to a total mass of $80M_{\odot}$ beyond which the binning was done according to the duration of the templates, to ensure similar templates are grouped together thus allowing correct approximation of the significance of coincident triggers. In the O2 search, since a variety of systems were being searched over together, two different

waveform approximants had to be used. The TaylorF2 type of approximant was used below an \mathcal{M} of 1.73 while the reduced-order model of a double aligned-spin effective-one-body waveform SEOBNRv4_ROM was used above it.

As a result of the changes in the search for IMBH going from O1 to O2, the sensitivity of the search in O2 needs to be compared to that in O1 and the relevant changes need to be understood and considered. This is in light of the fact that upper limits were placed on the rates of observation of IMBHs in O1 [31], hence while quoting such upper limits from O2 with a different search, awareness of the change in sensitivity would be in the interest of being consistent.

5.2.1 Comparison of the search sensitivity in 1st and 2nd observing runs of advanced LIGO

The spacetime volume sensitivity is the volume in space and time that the detector is sensitive to. In the GstLAL inspiral based pipeline, it is found following the formalism outlined in Eq. (2.3.15) and Eq. (2.3.16). This involves injecting simulated signals into the pipeline and finding the ratio of those recovered beyond a certain threshold of false alarm rate, to those injected, in each distance bin, which is proportional to the sensitivity of the search. In our study, we selected a chunk of O2 data and analyzed it using the GstLAL-based inspiral pipeline using the two different versions of the IMBH search in O1 and O2 as discussed above.

Injections Used

The same set of simulated injections were used for both studies. As shown in Fig. 59, injections depicting spin aligned systems with component masses $100 M_{\odot}$ and non spinning systems with component masses $300 M_{\odot}$ were used. The motivation behind this choice was, the O1 IMBH search was found to be most sensitive to the $100 M_{\odot}$ equal companion mass systems. Also, the $300 M_{\odot}$, unit mass ratio systems are not included in the templates of the O2 bank, but were included in the O1 bank. Hence it is useful to see how well they are recovered by the O2 search.

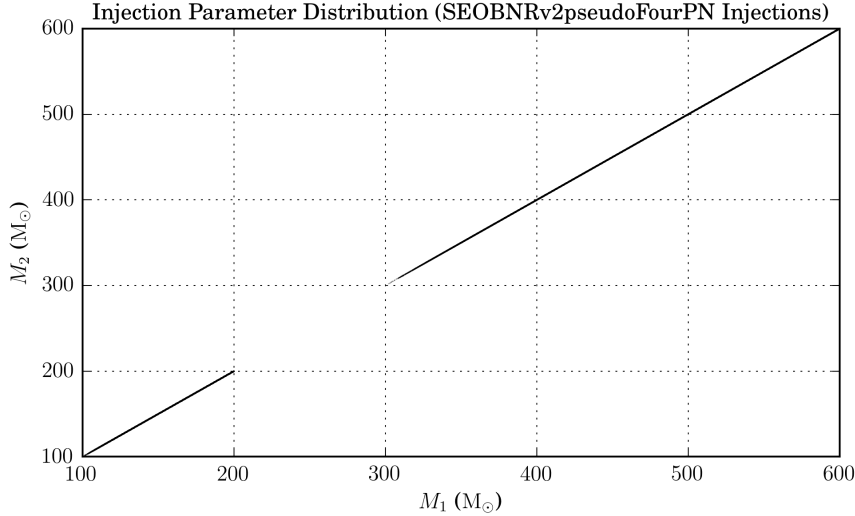


Figure 59 : Simulated signals or injections used to compare between the sensitivity of the GstLAL-inspiral based search in O1 Vs in O2.

Data Used

The data used corresponds to the chunk 19 of O2, taken between July 27, 2017 and August 5, 2017, corresponding to GPS times 1185217218-1185937218. This corresponds to ~ 5 days of coincident data in the H1 and L1 detectors.

Comparison of results and discussion

In Fig. 60 We show an overlay of the space time volume sensitivity Vs combined false alarm rate (CFAR) plots for both O1 IMBH only search and from the O2 search. The left and the right plots correspond to the sensitivity of the searches to all injection sets combined and for the $100 M_{\odot}$ and unit mass ratio systems respectively. The $300 M_{\odot}$ and unit mass ratio systems were not recovered by the O2 search as it does not have templates for such high mass systems, hence a comparison for that injection set has not been shown. Fig. 61 depicts the same information, but instead of showing the results of the two searches in different colours, we show the ratio of the sensitivity from the O1 Vs the O2 search. In either case, the following is observed:

1. The IMBH only search in O1 is found to be more sensitive to IMBH type of injections, rather than the O2 search. From Fig. 61 we can see that the O1 search is found to have higher sensitivity by a factor of ~ 2 (actually 1.9) at very low CFAR

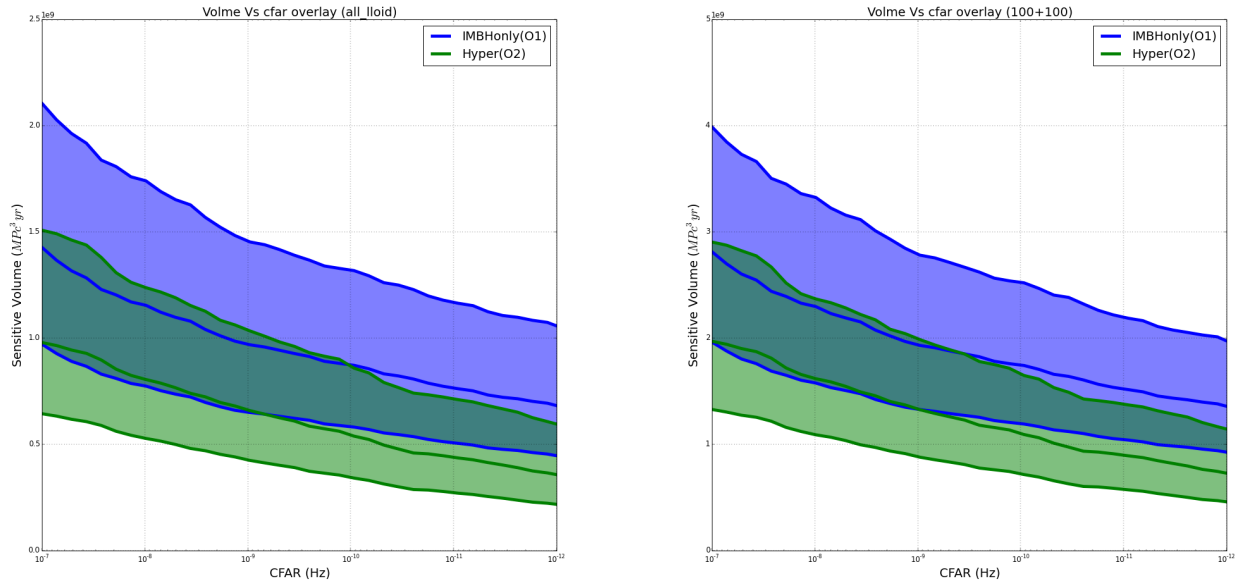


Figure 60 : Spacetime volume sensitivity Vs combined false alarm rate (CFAR) plots for an O1-like IMBH search (shown in cyan) and for an O2 search (shown in green) (from GstLAL-based inspiral pipeline). (Left) Comparison for all injections (Right) for $100M_{\odot}$, unit mass ratio systems. The dedicated IMBH search of O1 is found to be more sensitive than the search in O2 in case of the injections considered.

($10^{-13} Hz$). The number of templates in the O2 bank is higher by a factor of ~ 2 (actually 2.3). The increase in the number of templates going from O1 search to O2, would have increased the number of accidentals and hence increased the false alarm rate for the recovery of each injection.

2. The relative sensitivity of the searches change over the range of CFAR considered. This can be attributed to the fact that noise is non-gaussian causing glitches to have strange structures.
3. As has been mentioned above, The $300+300 M_{\odot}$ non-spinning injections (total mass: $600-1200 M_{\odot}$) could not be recovered by the O2 search, as they lie outside the parameter space covered.

5.3 Inclusion of higher order modes of waveforms

In the first observing run of LIGO no IMBHs were observed but the dedicated search results were used to place an upper limit on the rates of coalescences of IMBHs. For

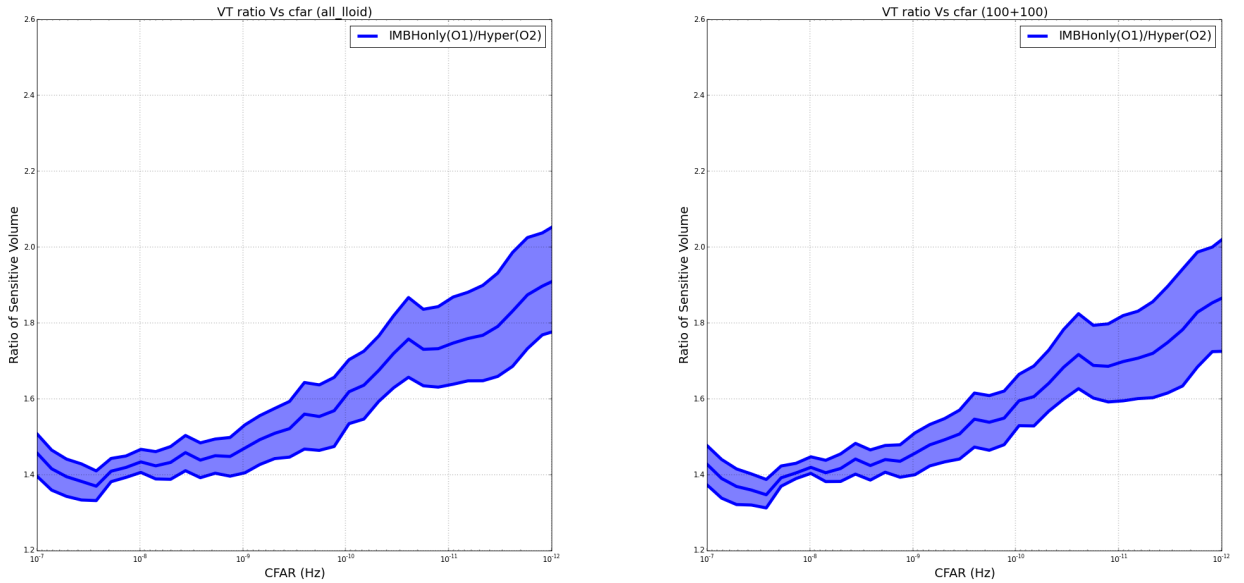


Figure 61 : Ratio of space time volume sensitivity Vs combined false alarm rate (CFAR) plots for an O1-like IMBH search and for an O2 search (O1/O2) . (Left) Comparison for all injections (Right) for $100M_{\odot}$, unit mass ratio systems. The O1 IMBH search is found to be more sensitive than the O2 search, especially at low CFAR i.e higher significance.

BBHs with component masses of $100 M_{\odot}$, systems to which the search was found to be most sensitive, the rate of observation was found to be $0.93 \text{ Gpc}^{-3} \text{ yr}^{-1}$ [31]. The sensitive distance for such systems was found to be 1.1 to 1.6 Gpc. The sensitive distance is that which is calculated from the sensitive volume or the volume in space and time out to which the search is sensitive, as calculated in chapter 2 in section 2.3

The sensitive spacetime volume, as shown in the above references, is calculated by injecting simulated signals into the detection pipelines such as the GstLAL-based inspiral pipeline. After a Monte Carlo integration over the space time volume being searched, it turns out that the sensitivity is proportional to the ratio of found to total number of injections. Hence for the accurate estimation of the spacetime volume sensitivity and hence the rate estimates, it is necessary that the simulated signals, accurately describe the systems being modeled.

5.3.1 Importance of higher order modes in the search

The gravitational wave h emitted by a binary black hole is a superposition of multiple modes of vibration written as $h_{(l,m)}$. The $h_{(2,\pm 2)}$ mode is the dominant quadrupole mode of vibration. Searches so far have modeled the gravitational waves using only the dominant $(l, m) = (2, \pm 2)$ mode, thus neglecting higher order modes of vibration [31] [42]. However, higher order modes have significant effect on the waveform for systems with total masses above $\sim 100 M_\odot$ and for mass ratio $q = \frac{m_1}{m_2} > 1$ where, $m_1 > m_2$ [42]. Hence especially for the IMBBH systems which are of unequal mass, not including higher order modes leads to inaccurate description of the signals, hence a biased estimation of the sensitivity of the search and hence that of rates.

The gravitational wave strain h at a point (d_L, θ, ϕ) in the sky where d_L is the luminosity distance, (θ, ϕ) being the sky localization and ψ being the effective polarization, is given by [42]:

$$h(\Xi; d_L, \iota, \phi; \bar{\iota}, \bar{\phi}, \psi_p; t - t_c) = F_+(\bar{\theta}, \bar{\phi}, \psi_p)H_+(d_L; \iota, \phi; \Xi; t - t_c) + F_\times(\bar{\theta}, \bar{\phi}, \psi_p)H_\times(d_L; \iota, \phi; \Xi; t - t_c) = \frac{F}{d_L}(\cos\psi\Re(\mathcal{H}) + \sin\psi\Im(\mathcal{H})) \quad (5.3.1)$$

where,

$$\mathcal{H} = h_+ - ih_\times = \sum_{l \geq 2} \sum_{m=-l}^{m=l} Y_{l,m}^{-2}(\iota, \phi) h_{l,m}(\Xi; t - t_c) \quad (5.3.2)$$

Here $F = \sqrt{F_+^2 + F_\times^2}$, $\tan\psi = \frac{F_\times}{F_+}$ and $h_{l,m}(\Xi; t) = A_{l,m}(\Xi; t)e^{-i\phi_{l,m}(\Xi; t)}$, $A_{l,m}$ and $\phi_{l,m}$ being real. (h_+, h_\times) are the plus and cross polarizations of the gravitational waves and (F_+, F_\times) gives the antenna pattern of the detector [43]. Ξ denotes the 8 intrinsic parameters including the masses of the binaries m_i and their dimensionless spins $\vec{\chi}_i = \vec{s}_i/m_i$. (r, ι, ϕ) is the reference frame in the standard spherical coordinates, such that the polar angle $\iota = 0$ coincides with the total angular momentum of the binary. $(\bar{\theta}, \bar{\phi})$ gives the general sky location and t_c gives the time of coalescence while ψ_p is the polarization of the signal. $Y_{l,m}^{-2}(\iota, \phi)$ is the spin -2 weighted spherical harmonics. $Y_{2,\pm 2}$ has a maxima at $\theta = (0, \pi)$ and a minima at $\theta = \pi/2$ while the higher order modes behave the opposite way. Hence while for face on/off sources the major contribution is from the (2,2) mode, for edge on sources a more important contribution comes from the higher order modes

[42]. Also, for a given $h_{l,m}$ mode, its frequency $f_{l,m} \propto m f_{orb}/M$ where f_{orb} is the orbital frequency and M its total mass. With increase in M , the (2,2) mode begins to leave the frequency band the detectors are sensitive to and falls into the low frequency noise. The higher m modes however have more contribution at this point, having higher frequency.

5.3.2 The contribution of higher order modes to the search sensitivity

A study was conducted to compare the sensitivity of the GstLAL-based inspiral pipeline based search as used in O2 towards injections including and not including higher order modes.

Injections Used

Four sets of simulated gravitational wave signals were mixed into the data to be recovered by the GstLAL-based inspiral pipeline. This included two sets of BBH injections and two sets of IMBH injections, in each case, the two sets are identical except for the fact that one of them includes higher order modes and the other does not. The waveform family used for the non higher order mode injections is EOBNRv2pseudoFourPN and for the higher order mode included injections it is EOBNRv2HMPseudoFourPN. For the stellar mass black holes, the component masses ranged between 3-97 M_{\odot} and the total masses between 6-100 M_{\odot} . They were non-spinning, injected between 5 and 300 Mpc. The mass ratios range between 1 and 31. The IMBH injections modeled systems with component masses between 50 and 300 M_{\odot} and total mass between 100 and 350 M_{\odot} . The injections were also non-spinning and were injected between 30Mpc -7.5Gpc. The mass ratios range between 1 and ~ 6 .

Data Used

The data used for the search corresponds to the chunk 10 of O2 with GPS times between 1173902418 and 174651218 which corresponds to March 18, 2017 GMT-20:00:00 to Mar 27, 2017, GMT-00:00:00.

Comparisons, results and discussions

The spacetime volume vs CFAR plots were obtained for each of the injection sets, by the GstLAL-based inspiral pipeline, as outlined in section 5.2.1. They were then compared in a similar fashion. As before, we obtain the ratios of the space time volume sensitivity for the injection sets excluding higher order modes and the ones including higher order modes for both BBHs and IMBHs. The following are observed:

1. For stellar mass BBH systems, inclusion of higher order modes do not seem to effect the overall sensitivity. The ratio stays close to 1.
2. The effect of inclusion of the higher order modes is significant for the IMBH systems with masses greater than $100 M_{\odot}$.
3. For high CFAR ($\sim 10^{-7} Hz \sim 1 \text{ per year}$) we find that excluding higher order modes causes the sensitivity to be underestimated, hence the ratio tends to be below 1
4. For low CFAR (hence higher significance) we see that exclusion of higher order modes leads to an overestimation of the sensitivity.

The rates quoted in [31] were computed without using higher order mode contributions, hence at low significance, the numbers are fairly conservative as the sensitivity is underestimated while omitting higher order modes. The rates for $q=1$ systems remain robust however since higher order modes have minimal contributions to them. Points 2 and 3 above can be explained as, at low significances, the higher power contributed by the higher order mode increases the SNR (signal to noise ratio) and hence the sensitivity. However, at a higher significance threshold, hence a lower CFAR, the greater mismatch between the injection waveforms including higher order modes and the templates which do not contain them, leads to lowering of the sensitivity. At higher significance, since a greater separation between signal and noise triggers is needed, triggers including higher order modes that have higher power are more likely to be lost in noise.

Our findings are mostly in line with similar comparisons done in [42]. A significant difference is, their comparisons used matched filter based search pipeline PyCBC and un-modeled search pipeline cWB [42]. Also, they used the searches as they were in O1.

In case of the matched filter based search, they saw the overestimation of sensitivity on exclusion of higher order modes at higher significances, go up by a factor of 2, in our case we see a maximum difference of a factor of 1.16.

5.4 looking forward: Plans for 3rd observing run

The 3rd observation run of LIGO, or O3 plans to include templates that contain information about higher order modes and simulations or injections that use waveforms computed using numerical relativity that include effects of higher order modes. This is expected to increase the sensitivity of the search.

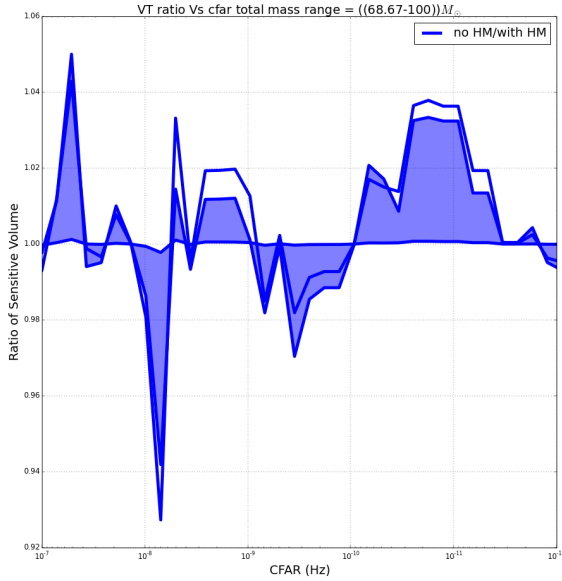
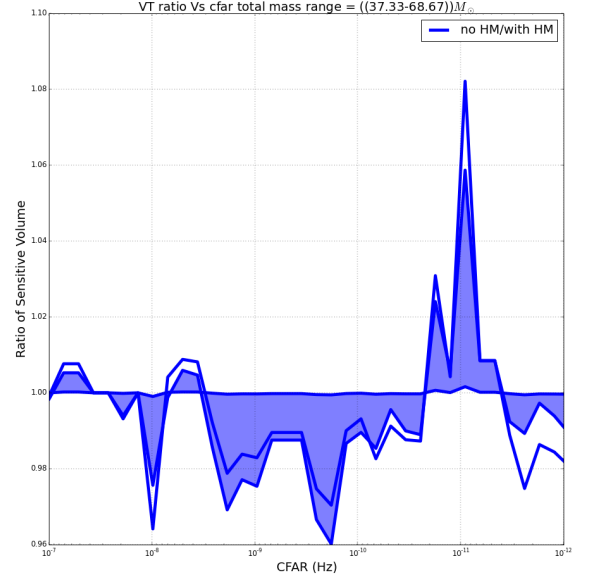
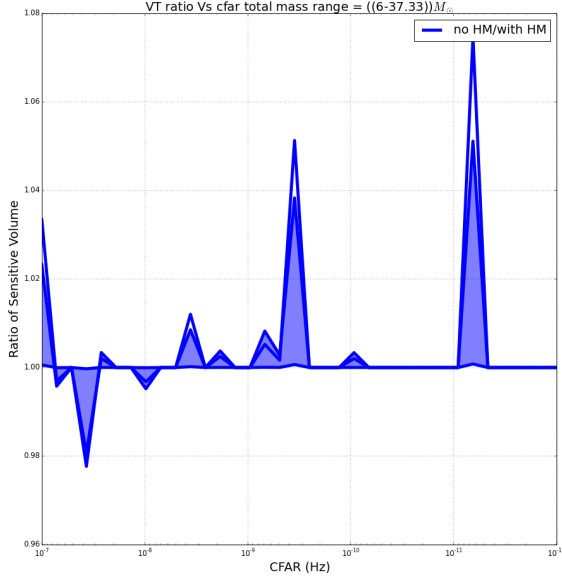


Figure 62 : Ratio of space time volume sensitivity Vs combined false alarm rate (CFAR) plots for BBH injections to compare the effect of not including Vs including higher order modes for an O2 search (no HM/with HM) . The three different plots correspond to different total mass bins spanning the whole injection set. For all mass bins, the ratio is close to 1 showing that HM injections do not change the results as much for stellar mass systems below a total mass of $100 M_{\odot}$

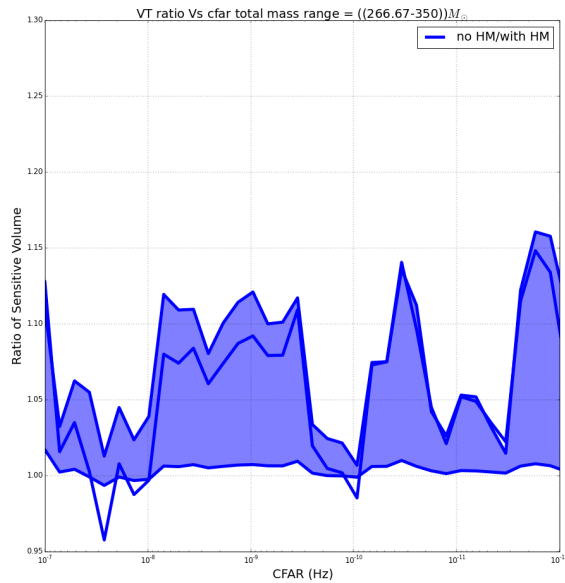
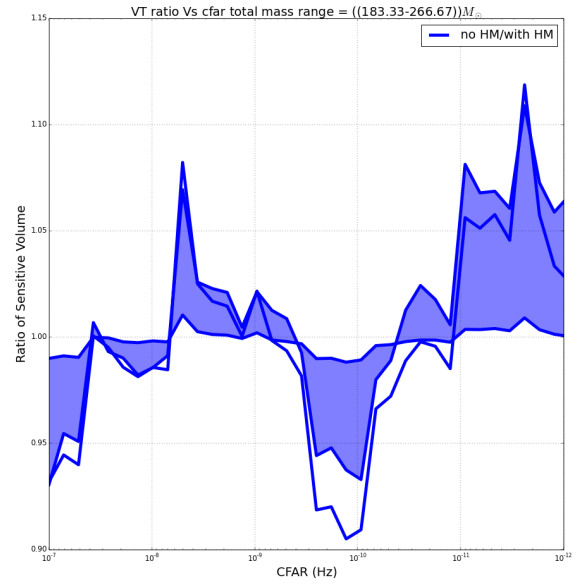
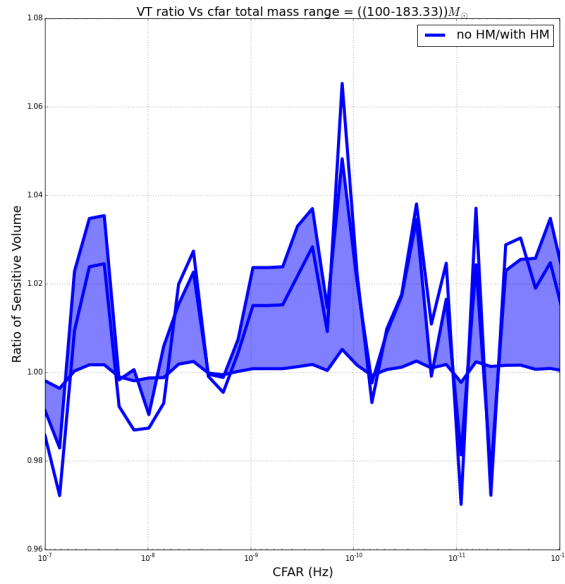


Figure 63 : Ratio of spacetime volume sensitivity vs combined false alarm rate (CFAR) plots for IMBH injections to compare the effect of not including vs including higher order modes for an O2 search (no HM/with HM) . The three different plots correspond to different total mass bins spanning the whole injection set. For all mass bins, the ratio is greater than 1 showing that absence of higher order modes leads to an overestimation of sensitivity and hence an underestimation of rates above a total mass of 100 M_{\odot} . The effect seems to be the highest for the highest mass bin and also seems to increase with decrease in CFAR, i.e increase in significance.

Chapter 6

Contributions to the Analysis of Advanced LIGO data using Matched Filter Based Offline Runs

6.1 Introduction

This chapter summarizes the contributions made to the first and second observing runs of advanced LIGO, with respect to data analysis using the GstLAL-inspiral based pipeline, presentation of results and followup investigations undertaken and contributions to collaboration-wide papers.

6.2 Contributions to latest and 2nd observation run (O2)

The second observing run of Advanced LIGO, otherwise known as O2, lasted between November 30, 2016 to August 26 2017.

6.2.1 Contributions to GstLAL-based inspiral pipeline search

As pointed out in chapter 4, the initial version of the O2 template bank was dense in the low-mass region. This is a typical feature as waveforms being longer for such systems, they have more distinguishing power and need better coverage. In the high-mass region, the waveforms being short, the bank was rare and if the same number of templates were

placed in each bin, as was inherited from O1, templates with very different parameters and hence very different noise characteristics, were being grouped together. To redress this, two different steps were taken as pointed out in that chapter. More templates (about 15,665) were added in the higher mass region (above $80 M_{\odot}$ in total mass). Also, the number of templates binned together was smaller in the higher mass region so as to ensure that only templates with similar noise properties get binned. This was done to ensure correct estimation of significance of triggers, which would not happen when background noise gets estimated inaccurately due to inefficient grouping of templates.

This can be appreciated from Fig. 65, left plot, loud coincident glitches in time shifted or “closed box” analysis, were found with the earlier version of the bank shown in the left plot of Fig. 64. These glitches do not show up in the right plot of Fig. 65 which was obtained using the final bank used by GstLAL-based inspiral pipeline for O2 as shown in Fig. 64 right plot.

I helped in the construction of the improved bank shown in Fig. 64 right plot. Extra templates had to be added but it had to be decided where to start the re-population of the bank. After several test banks, the extra templates were added after a total mass of $80 M_{\odot}$, as that was found to be most optimal. Also the templates had to be binned by duration above this mass limit instead of the \mathcal{M} - χ binning employed below it. This is because, for the low-mass systems the waveform is dominated by the inspiral region where \mathcal{M} and χ are the leading order terms. But this dependence diminishes for higher mass systems where the waveform is dominated by merger and ringdown, as discussed in chapter 4.

6.2.2 Conducting analysis runs and related investigations

Conducting analysis over science data involves looking for gravitational wave signature in the data using a search pipeline. I have contributed to the search using the GstLAL-based inspiral pipeline for end to end analysis of two chunks of data in O2. The pipeline works in a way described in chapter 4 [9]. The chunks analyzed majorly by me were Chunk 8 and 9 in O2, corresponding to GPS times (1172334618-1173188118) and (1173188118-1173902418) respectively. The results of the pipeline analysis are looked at in time shifted

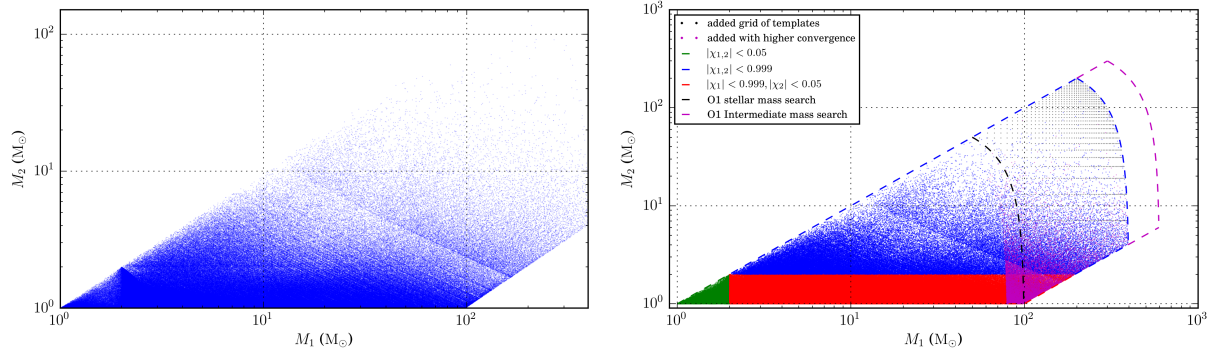


Figure 64 : The template bank used by GstLAL-based inspiral pipeline (left) before addition of extra templates (right) after addition of extra templates, which were added to reduce coincident glitches.)

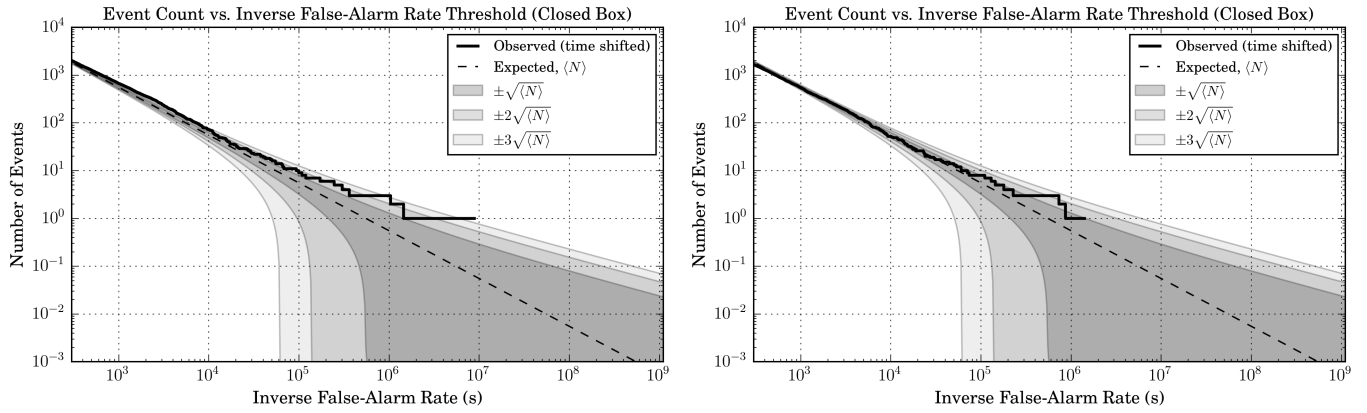


Figure 65 : For analysis of chunk 6 of O2 data (GPS: 1170948618 - 1171632618)(left) an Event count vs inverse false alarm rate (IFAR) plot showing loud coincident glitches classified as a detection in the time shifted data before extra templates were added (right) removal of such glitches.

data, so as to estimate any correlated background noise (also called closed box results). The coincident analysis shows any significant triggers or events (open box results). Injections missed at high SNR are followed up and time frequency heat maps called omega scans are obtained for them. These scans are useful for investigating glitches in a certain time interval. An example of such a followup is shown in Fig. 68.

The results were presented as a comparison between the search using the initial bank shown in Fig. 64 (left) and the new bank (right).

From Fig. 66 and Fig. 67 we see that more injections are missed at higher SNR and higher mass for the improved bank as compared to the original. Injections are said to be missed when they have a false alarm rate above the threshold of 1 per 30 days.

The sensitivity for the new bank run drops for the higher mass systems and increases

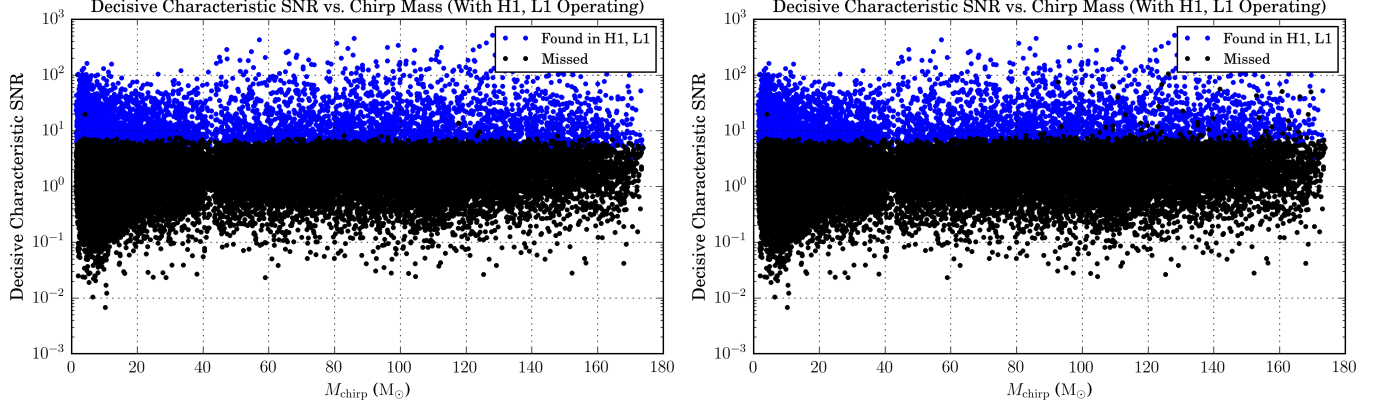


Figure 66 : Comparison of injections missed (combined false alarm rate or CFAR > 1 per 30 days) using the initial (left) and the final (right) bank used for O2 or second observing run of LIGO.)

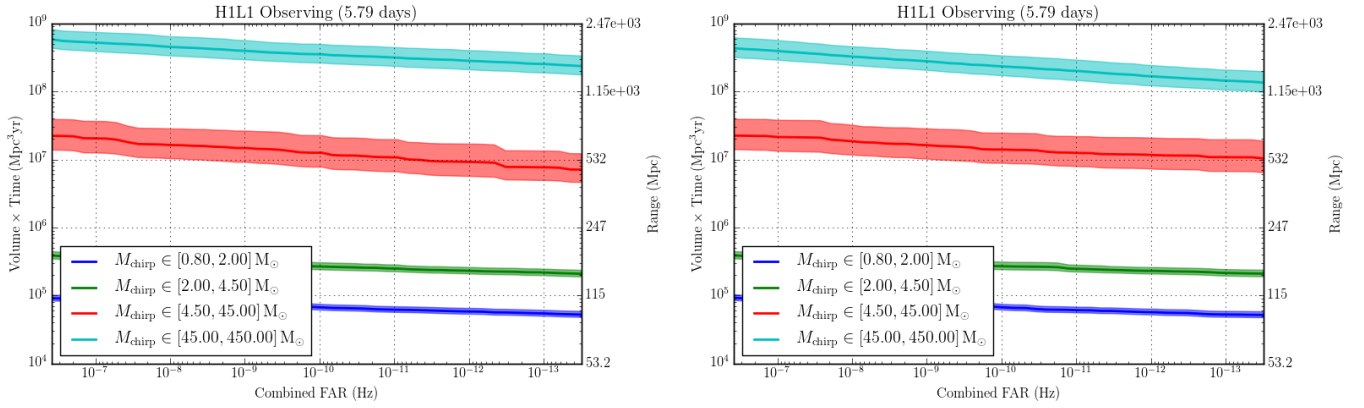


Figure 67 : Comparison of spacetime volume sensitivity using the initial (left) and the final (right) bank used for O2)

slightly for lower mass systems compared to the old search. The new addition of templates puts more templates in the IMBH region, constraining higher noise to this region, making sensitivity worse here. But since such noise is now constrained to the high mass bins, sensitivity and recovery of BBH systems improve.

In Fig. 66 most injections that are missed, are high mass (total mass $> 300 M_{\odot}$) systems and lie in the now less sensitive IMBH region, hence these are recovered with high CFARs or high chisquare values [9], with the exception of a few glitches, which are also missed. The precessing injections were missed as they are mostly extreme mass ratio systems (about 10:1) the sensitivity of the search towards such systems is limited.

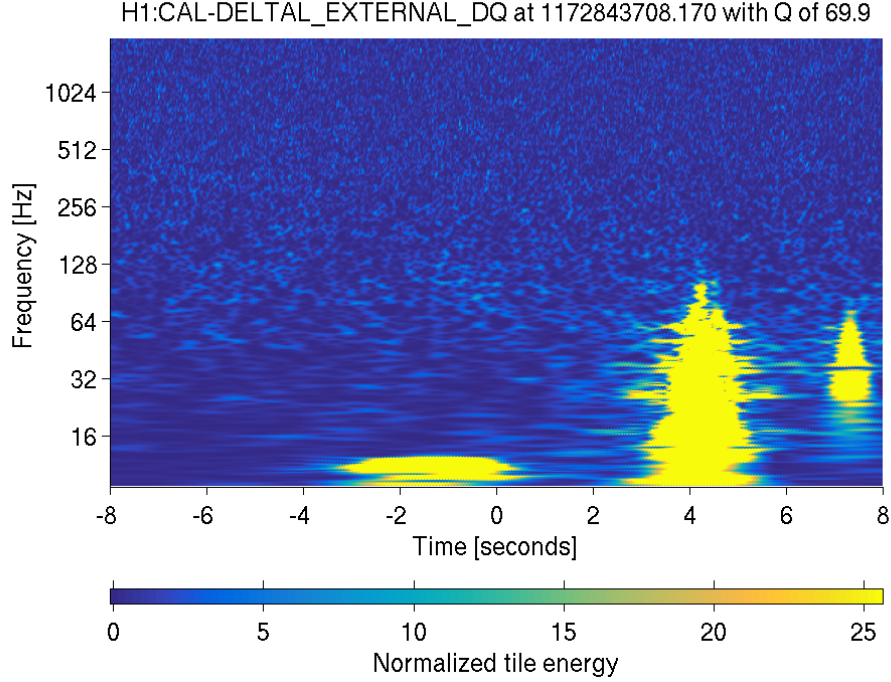


Figure 68 : Example of an omega scan followup of a missed injection, showing multiple glitches in H1 instrument, causing the injection to be missed.

The open box results in Fig. 69, seemed to show a marginally interesting candidate with False Alarm Probability (FAP) ~ 0.1 which corresponds to FAR $\sim 1/57$ days, which is below the $1/30$ days threshold for being catalogued as significant triggers. However after followup, it turned out to be a glitch in L1 as shown in Fig. 70.

6.2.3 Contribution to BNS rates calculation

On August 17 2017, a binary system of neutron stars were seen to merge, having component masses in the range $1.17\text{-}1.60 M_{\odot}$ [22] The gravitational wave event named GW170817 was followed by the observation of a gamma ray burst named GRB 170718A, by astronomers, thereby further corroborating the merger. This joint electromagnetic and gravitational wave observation of a merger was unprecedented and led to a lot of insight into the fields of cosmology, astrophysics and gravitational waves. I contributed to the calculation of the astrophysical rates of observation of binary neutron stars, using gravitational waves, which was used in the discovery paper [22].

The rates posterior for binary neutron stars can be calculated in the following way [44]:

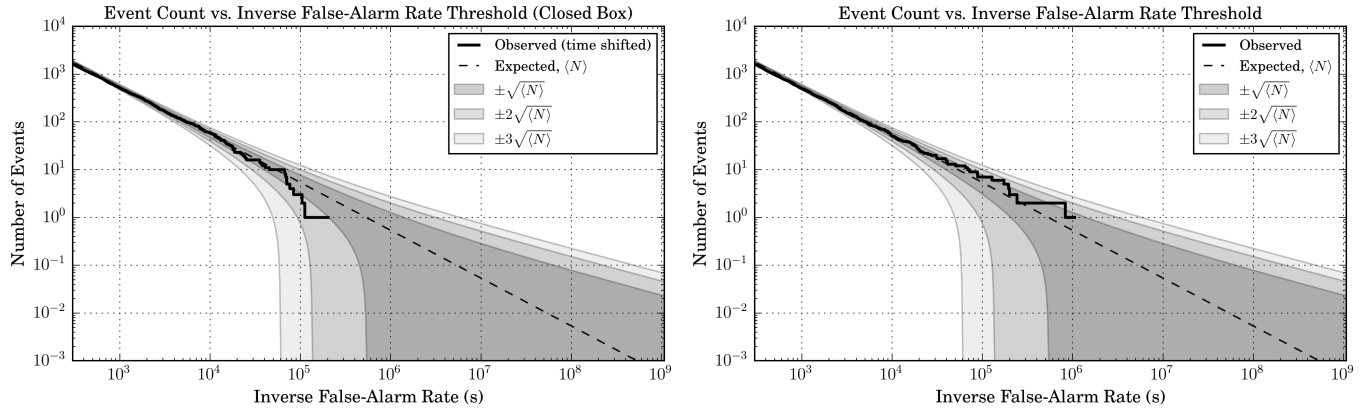


Figure 69 : For analysis of chunk 8 of O2 data (GPS: 1172334618-1173188118)(left) an Event count Vs Inverse false alarm rate or IFAR plot in the time shifted data (closed-box) (right) In coincident data (open-box). A marginally interesting candidate is seen in the coincident data.

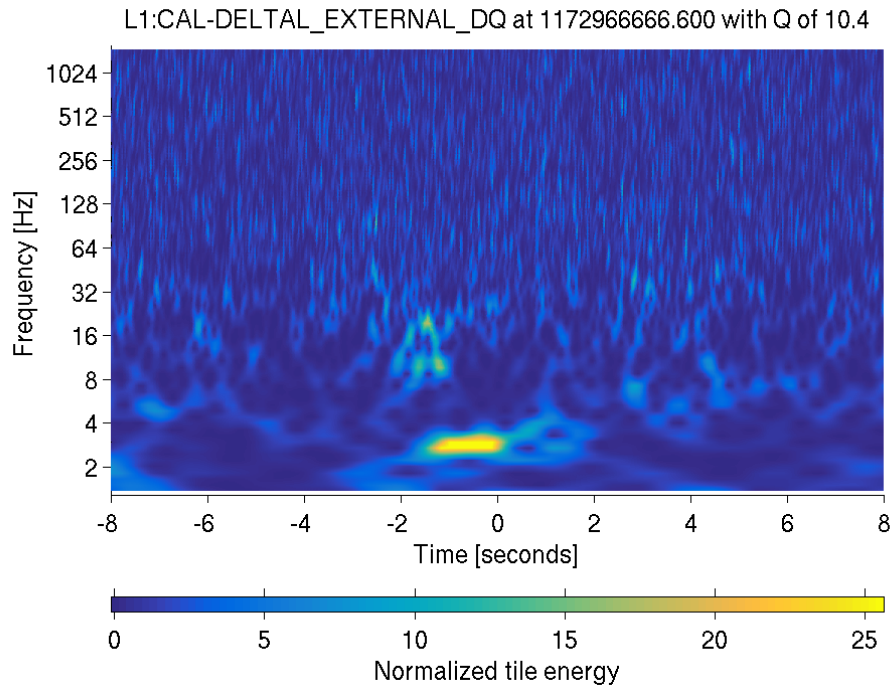


Figure 70 : Omega scan followup of the loudest coincident trigger in chunk 8, which turned out to be a glitch in L1 detector.

The posterior on the counts of events observed Λ is given by:

$$p(\Lambda|s) = p(\Lambda)e^{-\Lambda} \quad (6.2.1)$$

which is true from Bayes' Theorem, as the likelihood of zero observation in data s follows the Poisson distribution for zero events given by:

$$p(s|\Lambda) = e^{-\Lambda} \quad (6.2.2)$$

where $\Lambda = R\langle VT \rangle$ and R is the rate of observation and $\langle VT \rangle$ is the averaged spacetime volume sensitivity. Hence we can now jointly represent the posterior on R and $\langle VT \rangle$ as:

$$p(R, \langle VT \rangle | s) = p(R, \langle VT \rangle) e^{-R\langle VT \rangle} \quad (6.2.3)$$

The prior can be expanded as:

$$p(R, \langle VT \rangle) = p(R | \langle VT \rangle) p(\langle VT \rangle) \quad (6.2.4)$$

Now the prior $p(R | \langle VT \rangle)$ can be chosen to be uniform or flat and hence 1, or it can be chosen to be the Jeffery's Prior ($1/\sqrt{R\langle VT \rangle}$).

The other prior is chosen as [44]:

$$p(\langle VT \rangle) = \ln \mathcal{N}(\mu, \sigma^2) \quad (6.2.5)$$

where $\mu = \langle VT \rangle$, the mean and $\sigma = \Delta\langle VT \rangle / \langle VT \rangle$, the fractional error in $\langle VT \rangle$. We also consider a callibration error of 4%. We get the rate posterior by marginalizing Eq. 6.2.3 over $\langle VT \rangle$. Hence we have:

$$p(R | s) = \int d\langle VT \rangle \ln \mathcal{N}(\mu, \sigma^2) e^{-R\langle VT \rangle} \quad (6.2.6)$$

Figure 71 shows the posterior for BNS events obtained using O1 and O2 data. We used a CFAR threshold of 1/100 yr in our calculations and find at 90 % confidence interval, our 50th, 5th and 95th percentiles of the posterior gives the rate estimate as $\sim 1102_{-863}^{+1966} Gpc^{-3} yr^{-1}$. However, including the O1 upper limit of $12600 Gpc^{-3} yr^{-1}$ as a prior, the rate is estimated at $1540_{-1220}^{+3200} Gpc^{-3} yr^{-1}$ [22].

6.3 Contributions to papers

The papers I have contributed to are as follows:

1. On the bank used by Advanced LIGO's template based search for inspiralling compact binaries [45]: This is a paper under preparation and is close to a final draft. It

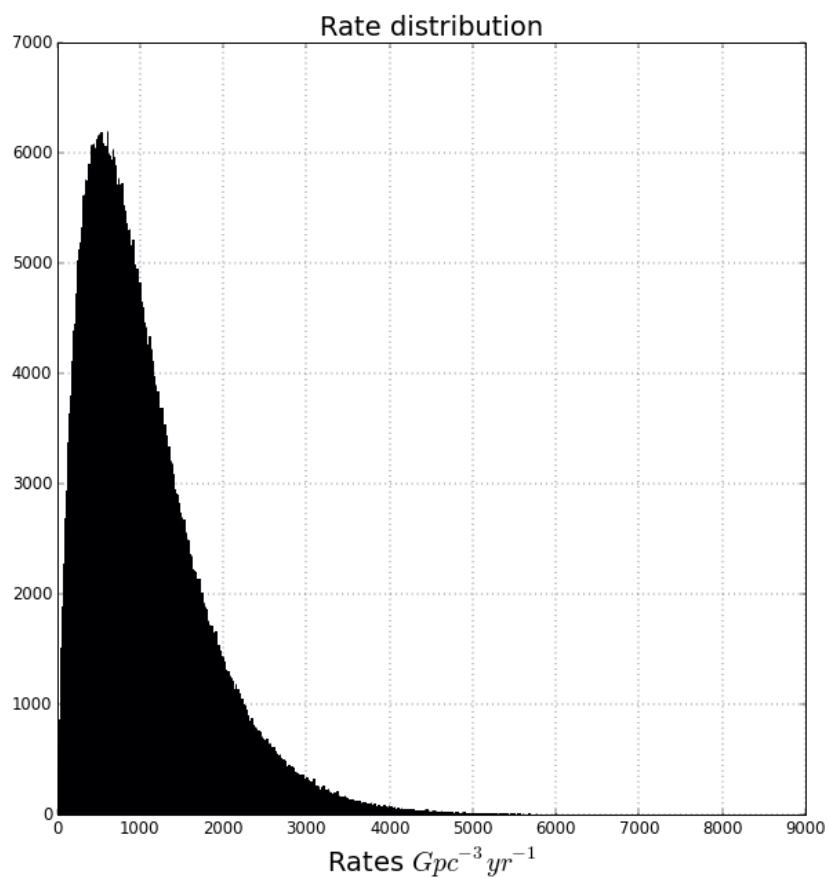


Figure 71 : The BNS posterior obtained in Eq. 6.2.6.

aims to describe in detail the construction of the template bank used by GstLAL-based inspiral pipeline for O2 search. It also describes changes in grouping background noise going from O1 to O2 and the effectualness of the bank. The study involved is described in details in chapter 4

2. The GstLAL Search Analysis Methods for Compact Binary Mergers in Advanced LIGO's Second and Advanced Virgo's First Observing Runs : This paper is under preparation and is close to a final draft. This describes the analysis methods used by GstLAL-based inspiral pipeline and changed introduced going from O1 to O2.

Collaboration wide papers

3. GW170817: Observation of Gravitational Waves from a Binary Neutron Star Inspiral [22]: This is the binary neutron star discovery paper. I contributed to the

calculation of the astrophysical rates of observation of binary neutron stars. The study undertaken is described in section 6.2.3

Future planned

4. O2 Catalogue paper: This is a paper that aims to accumulate or catalogue information about various detections and discoveries made by LIGO and Virgo instruments so far and list important triggers. It also aims to make astrophysical rates statements about various categories of binary populations. I aim to contribute to the statement about astrophysical rates of compact objects in the mass gaps. The preliminary study required to work towards such a calculation has been shown in chapter 3.

6.4 Contribution to 1st Observation run (O1):

The first observing run of Advanced LIGO, otherwise known as O1, lasted between September 12, 2015 to January 19, 2016.

6.4.1 SNR based trimming of IMBH injection files:

IMBH injection sets were trimmed or pruned based on their expected SNRs in the two detectors. Injections that have an expected SNR less than 2, were removed from the sets for a more efficient search. The total number of injections were reduced from 333180 to 59512. I contributed to trimming such injection sets based on their SNRs and running test analyses with the GstLAL-based inspiral pipeline in preparation for the O1 IMBH search.

6.4.2 Investigations of missed injections:

Similar to what is shown in subsection 6.2.2, I contributed to the follow up investigations of the missed injections. Injections were found to be missed either due to very high CFARs, glitches in the detectors as discussed before or the injection times being too close to the edge of a segment or a veto. I contributed to the missed injection investigations for chunks 456 and 789 in O1.

Chapter 7

Conclusion

The era of gravitational wave astronomy and astrophysics is here. Gravitational wave events have already been detected from several compact object mergers. We are progressing towards an era of robust astrophysical studies, statements and discoveries, based on gravitational wave observations, which help constrain astrophysical or cosmological hypotheses. On the other hand, LIGO is expected to reach design sensitivity in its fourth observing run and hence still needs technical and developmental work. This dissertation focuses on the following aspects:

- 1) the developmental aspects of the matched filter based GstLAL-based inspiral pipeline ;
- 2) use it to analyze and interpret science data collected in the 1st and 2nd observing runs of LIGO (O1 and O2) ;
- 3) use such data to make astrophysical statements about possibility of mergers from compact objects in the hypothetical gap separating binary neutron stars and black holes.

In chapter 2 We tried to assess the sensitivity of a search which is a combination of the stellar mass search of O1 and part of the Intermediate mass search of O1. This was in preparation for such a combined search in O2. We wanted to see if such a combined search will have optimal sensitivity. We tested a heuristically combined search against IMBH injections or simulations as these waveforms being short, they are likely to show up as glitches in such a combined search. We found that the combined search is more sensitive for the most part, but for higher masses and lower CFARs, the IMBH search turns out to be more sensitive. The likely reasons for this are, the combined search

involved a heuristic overlap of banks that were generated with parameters motivated by different searches. Also, the grouping of templates at higher masses was the same as that at the lower masses, causing templates with widely different noise characteristics to be grouped together and thereby causing sensitivity to fall spuriously. A larger bank is also likely to have more accidentals. This was addressed in O2 by making the bank denser in the higher mass region and the binning was done in a mass dependent fashion as seen in chapter 4. Also, as we see in chapter 5 the effect of lowering of the sensitivity of the combined bank, is more pronounced at lower CFAR, hence higher significance, as a better match is needed between templates and waveforms or in other words a better separation is needed between signal and noise. Having too few templates in the higher mass region, prevents a good match, which is taken care of by adding extra templates as shown in chapter 4. We also recommend template (or mass) based weighting of ranking statistics to account for such loss of sensitivity, which has been exhibited in chapter 3.

In chapter 3 we attempt to use Bayesian rate estimation to make astrophysical statements using data from O1 and O2 of advanced LIGO. The hypothesized supernova mass gap is known to separate neutron stars from black holes, and ranges between 3 and 5 M_{\odot} in component masses. We use the FGMC counting formalism along with template based weighting to obtain a posterior for observation of possible events within the proposed gap. We show that the FGMC formalism can be used to obtain counts posterior for a category of astrophysical objects that fall within the proposed gap. We show that the presence of a significant event at the centre of the gap, is observable as a shift in the mode of the counts posterior. We roughly estimate the number of events needed to falsify the mass gap if the underlying population of binaries is dominated by low mass Vs higher mass binaries.

In chapter 4 we described the design and construction of the template bank used by GstLAL-based inspiral pipeline in O2. We described the investigations done to ensure optimal sensitivity of the bank. We described the improvements made to the bank during O2 to prevent coincident noise in time-shifted data. We also describe the effectualness of the bank against different sets of simulations describing different astrophysical systems.

In chapter 5 we describe the major contributions made to the IMBH search during

O2. This falls majorly into two categories:

- 1) Comparison of the sensitivity of the search.
- 2) Inclusion of higher order mode simulations in the search.

We compare the sensitivities between the two observing runs, in view of the change in the compact object search going from O1 to O2. The search for intermediate mass binary black holes (IMBBH) was separate in O1, but was combined with the search for stellar mass in O2. Also there were changes in binning of the background noise between the two searches. The O2 bank was found to be less sensitive to IMBHs because it had a smaller parameter space and had a larger number of templates, thus increasing the number of accidentals. Also, the IMBH search had the spurious overestimation of significance due to incorrect estimation of background noise when templates with very different noise characteristics are grouped together. This study informed the decision by the IMBH working group to use the O2 bank to make IMBH search statements.

Inclusion of higher order modes were seen to affect the sensitivity towards high mass, extreme mass ratio systems that are edge on. At high CFAR (low significance) the increase in power within the sensitive frequency band of LIGO due to this inclusion, caused an increase in SNR thereby increasing the sensitivity. However at lower CFAR (higher significance) the sensitivity was seen to fall on including higher order modes due to mismatch with the templates, as a better match is required at such higher significances.

In chapter 6 we describe the contributions to the first and second observing runs of LIGO. In the first observing run, contributions were made by me mostly to the IMBH search in terms of pruning simulated waveforms on the basis of SNR to enable an efficient analysis for estimation of sensitivity. I also helped following up missed triggers in preparation for the presentation of the search results.

For O2, I contributed to optimization of the sensitivity of the search bank, analysis and interpretation of O2 data and contributed to papers.

The third observing run of LIGO is set to start later this year. Currently I am involved in working on papers that describe the search for O2 and summarize findings. I will also be using the concepts outlined in chapter 3 to contribute to making astrophysical statements about observation of events in the hypothetical mass gap, in the astrophysical

catalogue to be published by the collaboration.

Bibliography

- [1] J. D. E. Creighton and W. G. Anderson. *Gravitational-Wave Physics and Astronomy*. Weinheim, Germany: Wiley-VCH, 2011.
- [2] Joel M. Weisberg and Joseph H. Taylor. “Relativistic binary pulsar B1913+16: Thirty years of observations and analysis”. In: *ASP Conf. Ser.* 328 (2005), p. 25. arXiv: [astro-ph/0407149](https://arxiv.org/abs/astro-ph/0407149) [[astro-ph](#)].
- [3] B. P. Abbott, R. Abbott, et al. “Observation of Gravitational Waves from a Binary Black Hole Merger”. In: *Phys. Rev. Lett.* 116 (6 Feb. 2016), p. 061102. DOI: [10.1103/PhysRevLett.116.061102](https://doi.org/10.1103/PhysRevLett.116.061102). URL: <https://link.aps.org/doi/10.1103/PhysRevLett.116.061102>.
- [4] Leslie E Wade IV. *GRAVITATIONAL WAVES FROM ROTATING NEUTRON STARS AND COMPACT BINARY SYSTEMS*. Thesis submitted at The University of Wisconsin Milwaukee, 2015.
- [5] The LIGO Scientific Collaboration, J Aasi, et al. “Advanced LIGO”. In: *Classical and Quantum Gravity* 32.7 (2015), p. 074001. URL: <http://stacks.iop.org/0264-9381/32/i=7/a=074001>.
- [6] Alessandra Buonanno, Bala R. Iyer, et al. “Comparison of post-Newtonian templates for compact binary inspiral signals in gravitational-wave detectors”. In: *Phys. Rev. D* 80 (8 Oct. 2009), p. 084043. DOI: [10.1103/PhysRevD.80.084043](https://doi.org/10.1103/PhysRevD.80.084043). URL: <https://link.aps.org/doi/10.1103/PhysRevD.80.084043>.
- [7] Michael Pürrer. “Frequency-domain reduced order models for gravitational waves from aligned-spin compact binaries”. In: *Classical and Quantum Gravity* 31.19 (2014), p. 195010. URL: <http://stacks.iop.org/0264-9381/31/i=19/a=195010>.

- [8] Press Teukolsky Vetterling Flannery. *Numerical Recipes in C, The art of scientific computing*. Cambridge University Press, 2007.
- [9] Cody Messick, Kent Blackburn, et al. “Analysis framework for the prompt discovery of compact binary mergers in gravitational-wave data”. In: *Phys. Rev. D* 95 (4 Feb. 2017), p. 042001. DOI: [10.1103/PhysRevD.95.042001](https://doi.org/10.1103/PhysRevD.95.042001). URL: <https://link.aps.org/doi/10.1103/PhysRevD.95.042001>.
- [10] A. V. Filippenko, T. Matheson, et al. “A Black Hole in the X-Ray Nova Ophiuchi 1997”. In: *Publications of the Astronomical Society of the Pacific* 109.734 (1997), p. 461. URL: <http://stacks.iop.org/1538-3873/109/i=734/a=461>.
- [11] Will M. Farr, Niharika Sravan, et al. “The Mass Distribution of Stellar-mass Black Holes”. In: *The Astrophysical Journal* 741.2 (2011), p. 103. URL: <http://stacks.iop.org/0004-637X/741/i=2/a=103>.
- [12] Krzysztof Belczynski, Grzegorz Wiktorowicz, et al. “Missing Black Holes Unveil the Supernova Explosion Mechanism”. In: *The Astrophysical Journal* 757.1 (2012), p. 91. URL: <http://stacks.iop.org/0004-637X/757/i=1/a=91>.
- [13] Laura Kreidberg, Charles D. Bailyn, et al. “Mass Measurements of Black Holes in X-Ray Transients: Is There a Mass Gap?” In: *The Astrophysical Journal* 757.1 (2012), p. 36. URL: <http://stacks.iop.org/0004-637X/757/i=1/a=36>.
- [14] Tyson B. Littenberg, Ben Farr, et al. “Neutron Stars versus Black Holes: Probing the Mass Gap with LIGO/Virgo”. In: *The Astrophysical Journal Letters* 807.2 (2015), p. L24. URL: <http://stacks.iop.org/2041-8205/807/i=2/a=L24>.
- [15] J. Veitch et al. “Parameter estimation for compact binaries with ground-based gravitational-wave observations using the LALInference software library”. In: *Physical Review D* 91.4 (2015). DOI: [10.1103/PhysRevD.91.042003](https://doi.org/10.1103/PhysRevD.91.042003).
- [16] Will M. Farr, Jonathan R. Gair, et al. “Counting and confusion: Bayesian rate estimation with multiple populations”. In: *Phys. Rev. D* 91 (2 Jan. 2015), p. 023005. DOI: [10.1103/PhysRevD.91.023005](https://doi.org/10.1103/PhysRevD.91.023005). URL: <https://link.aps.org/doi/10.1103/PhysRevD.91.023005>.

- [17] Debnandini Mukherjee Heather Fong Shasvath Kapadia. *Source-Dependent Template-Weighting Methods to Evaluate CBC Rates*. dcc LIGO-G1700362, 2017.
- [18] Jolien Creighton Shasvath Kapadia. *Re-evaluation of O1-BNS-rates with mass-weighting*. dcc LIGO-G1700157, 2017.
- [19] Jolien Creighton. *Certain Identities in FGMC*. dcc T1700029-v1, 2017.
- [20] Shasvath Kapadia. *Using multicomponent FGMC with mass-based template weighting to determine the rates of compact binary mergers*. dcc T1800072-v1, 2018.
- [21] B. P. Abbott, R. Abbott, et al. “GW170814: A Three-Detector Observation of Gravitational Waves from a Binary Black Hole Coalescence”. In: *Phys. Rev. Lett.* 119 (14 Oct. 2017), p. 141101. DOI: [10.1103/PhysRevLett.119.141101](https://doi.org/10.1103/PhysRevLett.119.141101). URL: <https://link.aps.org/doi/10.1103/PhysRevLett.119.141101>.
- [22] B. P. Abbott, R. Abbott, et al. “GW170817: Observation of Gravitational Waves from a Binary Neutron Star Inspiral”. In: *Phys. Rev. Lett.* 119 (16 Oct. 2017), p. 161101. DOI: [10.1103/PhysRevLett.119.161101](https://doi.org/10.1103/PhysRevLett.119.161101). URL: <https://link.aps.org/doi/10.1103/PhysRevLett.119.161101>.
- [23] B. P. Abbott, R. Abbott, et al. “GW170608: Observation of a 19 Solar-mass Binary Black Hole Coalescence”. In: *The Astrophysical Journal Letters* 851.2 (2017), p. L35. URL: <http://stacks.iop.org/2041-8205/851/i=2/a=L35>.
- [24] A. Albert, M. André, et al. “Search for high-energy neutrinos from gravitational wave event GW151226 and candidate LVT151012 with ANTARES and IceCube”. In: *Phys. Rev. D* 96 (2 July 2017), p. 022005. DOI: [10.1103/PhysRevD.96.022005](https://doi.org/10.1103/PhysRevD.96.022005). URL: <https://link.aps.org/doi/10.1103/PhysRevD.96.022005>.
- [25] B. P. Abbott, R. Abbott, et al. “GW170104: Observation of a 50-Solar-Mass Binary Black Hole Coalescence at Redshift 0.2”. In: *Phys. Rev. Lett.* 118 (22 June 2017), p. 221101. DOI: [10.1103/PhysRevLett.118.221101](https://doi.org/10.1103/PhysRevLett.118.221101). URL: <https://link.aps.org/doi/10.1103/PhysRevLett.118.221101>.

- [26] B. P. Abbott, R. Abbott, et al. “Binary Black Hole Mergers in the First Advanced LIGO Observing Run”. In: *Phys. Rev. X* 6 (4 Oct. 2016), p. 041015. DOI: [10.1103/PhysRevX.6.041015](https://doi.org/10.1103/PhysRevX.6.041015). URL: <https://link.aps.org/doi/10.1103/PhysRevX.6.041015>.
- [27] B. P. Abbott, R. Abbott, et al. “The Rate of Binary Black Hole Mergers Inferred from Advanced LIGO Observations Surrounding GW150914”. In: *The Astrophysical Journal Letters* 833.1 (2016), p. L1. URL: <http://stacks.iop.org/2041-8205/833/i=1/a=L1>.
- [28] Walthinsen et al. *GStreamer*. <https://gstreamer.freedesktop.org>.
- [29] Adam Mercer et al. *LALSuite*. <https://www.lsc-group.phys.uwm.edu/daswg/projects/lalsuite.html>. Accessed: 2015-07-01.
- [30] Kipp Cannon, Chad Hanna, et al. *GstLAL*. <https://www.lsc-group.phys.uwm.edu/daswg/projects/gstlal.html>. Accessed: 2015-07-01.
- [31] B. P. Abbott, R. Abbott, et al. “Search for intermediate mass black hole binaries in the first observing run of Advanced LIGO”. In: *Phys. Rev. D* 96 (2 July 2017), p. 022001. DOI: [10.1103/PhysRevD.96.022001](https://doi.org/10.1103/PhysRevD.96.022001). URL: <https://link.aps.org/doi/10.1103/PhysRevD.96.022001>.
- [32] *The GstLAL Search Analysis Methods for Compact Binary Mergers in Advanced LIGO’s Second and Advanced Virgo’s First Observing Runs*. <https://dcc.ligo.org/LIGO-P1700411>. dcc link.
- [33] B. P. Abbott, R. Abbott, et al. “GW150914: First results from the search for binary black hole coalescence with Advanced LIGO”. In: *Phys. Rev. D* 93 (12 June 2016), p. 122003. DOI: [10.1103/PhysRevD.93.122003](https://doi.org/10.1103/PhysRevD.93.122003). URL: <https://link.aps.org/doi/10.1103/PhysRevD.93.122003>.
- [34] Benjamin D. Lackey, Koutarou Kyutoku, et al. “Extracting equation of state parameters from black hole-neutron star mergers: Aligned-spin black holes and a preliminary waveform model”. In: *Phys. Rev. D* 89 (4 Feb. 2014), p. 043009. DOI: [10.1103/PhysRevD.89.043009](https://doi.org/10.1103/PhysRevD.89.043009). URL: <https://link.aps.org/doi/10.1103/PhysRevD.89.043009>.

- [35] Duncan A. Brown, Ian Harry, et al. “Detecting binary neutron star systems with spin in advanced gravitational-wave detectors”. In: *Phys. Rev. D* 86 (8 Oct. 2012), p. 084017. DOI: [10.1103/PhysRevD.86.084017](https://doi.org/10.1103/PhysRevD.86.084017). URL: <https://link.aps.org/doi/10.1103/PhysRevD.86.084017>.
- [36] I. W. Harry, B. Allen, and B. S. Sathyaprakash. “Stochastic template placement algorithm for gravitational wave data analysis”. In: *Phys. Rev. D* 80 (10 Nov. 2009), p. 104014. DOI: [10.1103/PhysRevD.80.104014](https://doi.org/10.1103/PhysRevD.80.104014). URL: <https://link.aps.org/doi/10.1103/PhysRevD.80.104014>.
- [37] Sylvain Marsat, Alejandro Bohé, et al. “Next-to-leading tail-induced spin-orbit effects in the gravitational radiation flux of compact binaries”. In: *Classical and Quantum Gravity* 31.2 (2014), p. 025023. URL: <http://stacks.iop.org/0264-9381/31/i=2/a=025023>.
- [38] Mark Hannam, Patricia Schmidt, et al. “Simple Model of Complete Precessing Black-Hole-Binary Gravitational Waveforms”. In: *Phys. Rev. Lett.* 113 (15 Oct. 2014), p. 151101. DOI: [10.1103/PhysRevLett.113.151101](https://doi.org/10.1103/PhysRevLett.113.151101). URL: <https://link.aps.org/doi/10.1103/PhysRevLett.113.151101>.
- [39] *SEOBNRv4ROM*. <https://dcc.ligo.org/LIGO-G1601761>. dcc link.
- [40] Nathan Leigh, Alison Sills, and Torsten Böker. “Modifying two-body relaxation in N-body systems by gas accretion”. In: *Monthly Notices of the Royal Astronomical Society* 433.3 (2013), pp. 1958–1965. DOI: [10.1093/mnras/stt862](https://doi.org/10.1093/mnras/stt862). eprint: [/oup/backfile/content_public/journal/mnras/433/3/10.1093/mnras/stt862/2/stt862.pdf](http://oup/backfile/content_public/journal/mnras/433/3/10.1093/mnras/stt862/2/stt862.pdf). URL: <http://dx.doi.org/10.1093/mnras/stt862>.
- [41] J. Aasi, B. P. Abbott, et al. “Search for gravitational radiation from intermediate mass black hole binaries in data from the second LIGO-Virgo joint science run”. In: *Phys. Rev. D* 89 (12 June 2014), p. 122003. DOI: [10.1103/PhysRevD.89.122003](https://doi.org/10.1103/PhysRevD.89.122003). URL: <https://link.aps.org/doi/10.1103/PhysRevD.89.122003>.
- [42] Juan Calderón Bustillo, Francesco Salemi, et al. “Sensitivity of gravitational wave searches to the full signal of intermediate-mass black hole binaries during the first observing run of Advanced LIGO”. In: *Phys. Rev. D* 97 (2 Jan. 2018), p. 024016.

DOI: [10.1103/PhysRevD.97.024016](https://doi.org/10.1103/PhysRevD.97.024016). URL: <https://link.aps.org/doi/10.1103/PhysRevD.97.024016>.

- [43] Piotr Jaranowski, Andrzej Królak, and Bernard F. Schutz. “Data analysis of gravitational-wave signals from spinning neutron stars: The signal and its detection”. In: *Phys. Rev. D* 58 (6 Aug. 1998), p. 063001. DOI: [10.1103/PhysRevD.58.063001](https://doi.org/10.1103/PhysRevD.58.063001). URL: <https://link.aps.org/doi/10.1103/PhysRevD.58.063001>.
- [44] B. P. Abbott, R. Abbott, et al. “Upper Limits on the Rates of Binary Neutron Star and Neutron Star-Black Hole Mergers from Advanced LIGO’s First Observing Run”. In: *The Astrophysical Journal Letters* 832.2 (2016), p. L21. URL: <http://stacks.iop.org/2041-8205/832/i=2/a=L21>.
- [45] Debnandini Mukherjee et al. *On the banks used by Advanced LIGO’s template based search for inspiralling compact binaries*. <https://dcc.ligo.org/LIGO-P1700412>. dcc link.

Debnandini Mukherjee

EDUCATION

- 8/2012–5/2018* **Doctor of Philosophy in Physics**
Leonard E. Parker Center for Gravitation, Cosmology and Astrophysics,
University of Wisconsin – Milwaukee, Milwaukee WI
Advisor: Patrick R. Brady
Awards: Physics Research Excellence Award, Chancellor's Graduate Student Award
- 7/2009–6/2011* **Master of Science (M.Sc) Physics**
University of Delhi (India)
- 7/2006–6/2009* **Bachelor of Science (B.Sc Honours) Physics**
University of Delhi (India)

RELEVANT SKILLS

- Programming Languages: Python, C, C++, Pascal
- Experience with using and improving data analysis packages and pipelines used in LIGO.
- Public Outreach activities :
 1. As a member of Coffeeshop Astrophysics at UW Milwaukee, helped prepare and give a number of astro-related public talks.
 2. Astro Break Talks: Talks given at the Manfred Olson Planetarium (UW Milwaukee).
 3. Astro club : 20 minute talks given to an audience of undergraduate physics majors.

SELECTED HONOURS AND AWARDS

- 8/2012–Present* UWM Physics Research Excellence Award
- 8/2012–Present* UWM Chancellor's Graduate Student Award
- December 4, 2016* Special Breakthrough Prize in Fundamental Physics
- July 2016* Gruber Cosmology Prize
- Aug 23 2017* Tied for 1st place in 2 minute Thesis Pitch (UWM)

TEACHING EXPERIENCE

- General Physics Laboratory I (non-Calculus)(Physics 121) - Fall 2012–Summer 2013, Spring 2014-Fall 2015
- Physics for health professionals (Physics 110) - Fall 2013
- Lab Physics I (Calculus treatment) (Physics 214) - Spring 2017, Fall 2017

CONFERENCES AND PRESENTATIONS

1. **Gravitational Wave Physics and Astronomy Workshop 2016** (GWPAW), Cape Cod, MA, Jun. 2016: talk on “Searching for intermediate mass black hole binaries using Advanced LIGO”
2. **American Physical Society April Meeting 2016** (APS April 2016), DC, 2016: talk on “Towards an extended binary black hole search using advanced LIGO: from stellar to intermediate mass”
3. **Ligo-Virgo Collaboration March meeting 2017** (LVC) Pasadena, CA, March 2017: Poster on: “Source-dependent template-weighting methods to evaluate compact binary coalescence rates” presented by Debnandini Mukherjee, Shasvath Kapadia & Heather Fong.
4. **Global Relay of Observatories Watching Transients Happen (GROWTH) 2017** Milwaukee, WI, Oct. 2017: talk on “Using data from Advanced LIGO to make astrophysical statements: what the search for compact objects have to say”
5. **Graduate Student Research Symposium for Math, Engineering and the Natural Sciences 2016** UW Milwaukee, WI, Oct. 2016: talk on “Search for gravitational waves using advanced LIGO”

INVITED TALKS

1. **Marquette University** March 2017: Talk given to a class of physics undergraduates on “Gravitational waves and LIGO”

LIST OF PUBLICATIONS

Primary Publications

1. **Debnandini Mukherjee**, Patrick Brady, et al. “On the bank used by Advanced LIGO’s template based search for inspiralling compact binaries” (in prep)
2. Surabhi Sachdev, **Debnandini Mukherjee**, et al. “Improved analysis framework for the Prompt Discovery of Compact Binary Mergers in Gravitational-wave Data” (in prep, title not finalized)

Major Contributions to Collaboration Publications:

1. B.P Abbot,...**D. Mukherjee**, et al. “GW170817: Observation of Gravitational Waves from a Binary Neutron Star Inspiral” Phys. Rev. Lett. 119, (2017) 161101 : Calculation of astrophysical rate of Binary Neutron Stars (sec. V, A)
2. Helped with the gstreamer based GstLAL offline search over Advanced LIGO’s 1st and 2nd observation run data. Also helped with improvements in search template banks and mechanisms.

Selected Collaboration Publications:

1. B.P Abbot,...**D. Mukherjee**, et al. “GW170814: A Three-Detector Observation of Gravitational Waves from a Binary Black Hole Coalescence” Phys. Rev. Lett. 119, (2017) 141101
2. B.P Abbot,...**D. Mukherjee**, et al. “GW170104: Observation of a 50-Solar-Mass Binary Black Hole Coalescence at Redshift 0.2” Phys. Rev. Lett. 118, (2017) 221101
3. B.P Abbot,...**D. Mukherjee**, et al. “GW170104: Observation of a 50-Solar-Mass Binary Black Hole Coalescence at Redshift 0.2” Phys. Rev. Lett. 118, (2017) 221101
4. B.P Abbot,...**D. Mukherjee**, et al. “Search for intermediate mass black hole binaries in the first observing run of Advanced LIGO” Phys. Rev. D 96, 022001 (2017)
5. B.P Abbot,...**D. Mukherjee**, et al. “Upper limits on the rates of binary neutron star and neutron star - black hole mergers from Advanced LIGO’s first observing run” Astrophys. J. Lett. 832, L21 (2016)
6. B.P Abbot,...**D. Mukherjee**, et al. “The basic physics of the binary black hole merger GW150914” Annalen der Physik 529, 1600209 (2017)
7. B.P Abbot,...**D. Mukherjee**, et al. “Binary black hole mergers in the first Advanced LIGO observing run” Phys. Rev. X 6, 041015 (2016)
8. B.P Abbot,...**D. Mukherjee**, et al. “GW151226: Observation of Gravitational Waves from a 22-Solar-Mass Binary Black Hole Coalescence” Phys. Rev. Lett. 116, 241103 (2016)
9. B.P Abbot,...**D. Mukherjee**, et al. “Observation of Gravitational Waves from a Binary Black Hole Merger” Phys. Rev. Lett. 116, 061102 (2016)

10. B.P Abbot,...**D. Mukherjee**, et al. “GW150914: First results from the search for binary black hole coalescence with Advanced LIGO” *Phys. Rev. D* 93, 122003 (2016)
11. B.P Abbot,...**D. Mukherjee**, et al. “Astrophysical Implications of the Binary Black-Hole Merger GW150914” *Astrophys. J. Lett.* 818, L22 (2016)
12. B.P Abbot,...**D. Mukherjee**, et al. “The rate of binary black hole mergers inferred from Advanced LIGO observations surrounding GW150914” *Astrophys. J. Lett.* 833, L1 (2016)